A VIBRATIONAL SPECTROSCOPIC STUDY OF AQUEOUS HYDROGEN HALIDE SOLUTIONS: *APPLICATION TO ATMOSPHERIC AEROSOL CHEMISTRY*

A Thesis

Presented in Partial Fulfillment of the Requirements for

the Degree Master of Science

in the Graduate School of The Ohio State University

By

Lori M. Levering

*****

The Ohio State University
2005

Master's Examination Committee:

Professor Heather Allen, Advisor

Professor Walter Lempert

Approved by

_____

Advisor
Department of Chemistry

ABSTRACT

Heterogeneous reactions on the surfaces of atmospheric aerosols play an important role in atmospheric chemistry. These reactions are capable of converting alkyl and hydrogen halides (common constituents of marine boundary aerosols) into active halogen compounds. Fundamental questions still remain concerning surface species and reaction mechanisms pertaining to marine boundary aerosols. The first step in beginning to understand these heterogeneous reactions is to determine how ions in solutions affect the structure of water at the air-liquid interface.

The air-liquid interface of aqueous hydrogen-halide (strong acid) solutions is examined using vibrational sum frequency generation spectroscopy. ATR-FTIR (attenuated total internal reflection Fourier transform infrared) and Raman spectroscopies are also used to compare the effects of the ions on the water structure in the bulk solutions to that of the interface. The bulk and air-liquid interface of aqueous sodium chloride and sodium hydroxide solutions are also investigated to compare the differences between the acid, sodium salt, and base solutions. The addition of HCl, HBr, and HI to water results in an increasing disruption of the hydrogen-bonding network with increasing size, polarizability, and concentration of the ions arising from the solvation shell of the anions. These results are similar to those for NaCl and NaOH. The addition of

HCl, HBr, and HI to water is found to cause a significant disruption in the hydrogen-bonding network at the air-liquid interface, whereas NaCl and NaOH have little effect on the interfacial water structure. Analysis of the spectra indicates the presence of H_3O^+ (and $H_5O_2^+$) and bromide and iodide anions in the interfacial region with an increase in interfacial depth.

To
My Parents
Dennis & Eileen Levering

ACKNOWLEDGMENTS

There are many people who have been instrumental in me achieving this goal. To list them all would be impossible, but there are a few that deserve a special thank you. First of all, I would like to thank my advisor, Heather Allen, for providing the guidance and support necessary to complete the research for this degree. I would also like to thank all of the members of the Allen lab, both past and present. In particular, Dr. Dingfang Liu was always readily available to assist when obstacles arose. The discussions and brainstorming with Dr. Sandhya Gopalakrishnan, Lisa Van Loon, and Dr. Laura Voss were always helpful.

A very special thank you goes to my parents. Without their constant encouragement and support, this achievement would not have been possible. I would also like to thank Carri, Misty, Kelly, and Mindy, who provided the comic relief and road trips that helped me keep my sanity through this process.

I also thank Research Corporation (Research Innovation Award) and NSF-Atmospheric Sciences award #ATM-0413893 for partial support.

VITA

December 8, 1979. . . . . Born – Marion, Ohio

1999 – 2002. . . . . Undergraduate Teaching Assistant
Ohio Northern University

2001 – 2002. . . . . Undergraduate Research Assistant
Ohio Northern University

May 19, 2002. . . . . B. S. Chemistry
Ohio Northern University

2002 – 2005. . . . . Graduate Teaching and Research Assistant
The Ohio State University

PUBLICATIONS

Research Publications

Martin Mucha, Tomaso Frigato, Lori M. Levering, Heather C. Allen, Douglas J. Tobias, Liem X. Dang, Pavel Jungwirth, "A Unified Molecular Picture of the Surfaces of Aqueous Acid, Base, and Salt Solutions", *Journal of Physical Chemistry B*, **2005**.

Dingfang Liu, Gang Ma, Lori M. Levering, and Heather C. Allen, "Vibrational Spectroscopy of Aqueous Sodium Halide Solutions and Air-Liquid Interfaces: Observation of Increased Interfacial Depth", *Journal of Physical Chemistry B*, **2004**, *108*(7), pp. 2252-2260.

FIELDS OF STUDY

Major Field: Chemistry

TABLE OF CONTENTS

Page

LIST OF TABLES

LIST OF FIGURES

LIST OF ABBREVIATIONS

ATR-FTIR	attenuated total internal reflection Fourier transform infrared
CCD	charge coupled device
CW	continuous wave
DAA	single proton donor – double proton acceptor
DDAA	double proton donor – double proton acceptor
DDA	double proton donor – single proton acceptor
FWHM	full-width at half-maximum
HWHM	half-width at half-maximum
GaAs	Gallium Arsenide
M	moles per liter
OPA/OPG	optical parametric generator/amplifier
ps	picosecond
VSFG	vibrational sum frequency generation
x	mole fraction
β	beta – molecular susceptibility
Γ	gamma – half-width at half-maximum (HWHM)
χ	chi – macroscopic second-order nonlinear susceptibility

CHAPTER 1

INTRODUCTION

In the last decade, atmospheric aerosol surface chemistry has been recognized to play a critical role in the uptake and transformation of gaseous species present in the atmosphere.[1-3] Although the large impact aerosols have on heterogeneous reactions in the atmosphere is well acknowledged, fundamental questions still remain concerning surface species and reaction mechanisms pertaining to marine boundary aerosols. The identity and orientation of the species at the surface of these aerosols may have a large impact on the physical characteristics of the surface (i.e. hydrophobicity, particle growth and morphology) and thus influence the absorption and adsorption of gas phase molecules. In addition, many of the chemical processes sea salt aerosols undergo (i.e. scavenging of reactive gases, chemical transformations in the aqueous phase, and volatilization of products) are pH dependent.[4] However, the determination of aerosol pH is difficult, leading to a wide range of estimated experimental pH values ranging from less that one to greater than nine.[4] Consequently, these pH dependent processes in sea salt aerosols are not well understood.

The ubiquitous nature of water in atmospheric aerosols makes investigating the air-aqueous interface a natural first step in understanding both the physical and chemical

processes of aerosols. The general understanding of the air-water interface can be extended to strong acid aqueous solutions to examine the effects of halide ions and protons on the surface structure of water. These fundamental studies can then provide insight into the role of species at the surface of atmospheric aerosols and atmospheric heterogeneous reaction mechanisms. In light of this, investigations into the bulk and interfacial structure of hydrogen halide (i.e. strong acid) solutions are presented in this thesis. Vibrational sum frequency generation (VSFG) spectroscopy is used to examine the air-liquid interface of hydrogen halide (i.e. strong acid) aqueous solutions, providing detailed, microscopic information about the distribution of ions at the air/water interface. Surface tension measurements were obtained to provide a macroscopic view of the concentration changes (with respect to the bulk) in the surface region of the aqueous solutions. In order to draw a comparison between the interface and the bulk solution, the hydrogen halide aqueous solutions were investigated with Raman and attenuated total internal reflection Fourier transform infrared (ATR-FTIR) spectroscopies.

1.1 Sea Salt Aerosols

Ocean waves have the consequence of ejecting small droplets of seawater into the air, serving as a large source of chlorine and bromine in the marine boundary layer.[2] As these droplets ascend into the atmosphere, water evaporates, leaving behind small aerosols. It is expected that these sea salt aerosols have the same ionic composition as seawater, but instead these particles are often deficient in chloride and bromide relative to sodium.[1,2] This discrepancy in concentration indicates sea salt aerosols react with atmospheric gases to convert condensed-phase halides into gas-phase halogen species, thus having a large impact on both stratospheric and tropospheric chemistry. An

important reaction involves the uptake of nitric and sulfuric acids by aerosols and the subsequent displacement of chloride and bromide into the gas phase as HCl and HBr, respectively.[5,6]

$$NaCl\ (aq) + HNO_3\ (aq) \rightarrow NaNO_3\ (aq) + HCl\ (g) \quad (1)$$

$$2\ NaCl\ (aq) + H_2SO_4\ (aq) \rightarrow Na_2SO_4\ (aq) + 2\ HCl\ (g) \quad (2)$$

Similar reactions involving bromine have been suggested and confirmed by laboratory studies.[7,8]

The acid displacement reactions involving chloride and bromide (e.g. Reactions 1 and 2) are strongly pH dependent.[1,4] Sea-salt aerosols at circumneutral and higher pH scavenge gaseous HCl, whereas, at pH values below about 4 (achieved by the accumulation of strong acids such as H_2SO_4 and HNO_3), HCl is degassed from the aerosol.

The main source of atmospheric iodine in the marine boundary layer is organoiodine compounds resulting from antimicrobial activity of various types of macroalgae and phytoplankton.[9,10] Photolysis of organoiodines, such as methyl iodide (CH_3I) yields iodine atoms which can then react with HO_2 to release HI into the gas phase as shown in equations 3-4.[9-11]

$$CH_3I + h\nu \rightarrow CH_3 + I \quad (3)$$

$$I + HO_2 \rightarrow HI + O_2 \quad (4)$$

$$(k_4 = 7.0 \times 10^{-11}\ cm^3\ s^{-1})$$

1.2 Atmospheric Halogen Concentrations

Sea salt aerosol concentrations of chloride, bromide, and iodide would be expected to mimic that of seawater. Typical concentrations of chlorine, bromine and iodine in sea water are 1.9 x 10^4 mg/L, 65 mg/L, and 6 x 10^{-2} mg/L, respectively.[12] However, as the droplet ascends into the atmosphere, water evaporates, leaving behind a more concentrated particle. To complicate sea salt aerosol concentration measurements further, sea salts are often deficient in halogens due to their release into the gas phase, as previously mentioned. Consequently, halogen concentrations, especially chloride and bromide, in sea salts are difficult to determine, although it is known that the molar ratio of chloride to bromide in sea salt particles is approximately 650:1.[1,2]

1.3 Tropospheric Chemistry of Hydrogen Halides

The interest in sea salt aerosol chemistry arises from the potential to form photochemically active halogen compounds from its reactions in the troposphere. These compounds can absorb light to generate halogen atoms.

HCl, a product of the ion exchange reactions of nitric and sulfuric acids in the troposphere, can react with the hydroxyl radical to form water and chlorine atoms.[1,2]

$$HCl + OH\cdot \rightarrow H_2O + Cl\cdot \qquad (5)$$

The resulting chlorine radical can then react rapidly with ozone ($k = 1.2 \times 10^{-11}$ cm^3 $molecule^{-1}$ s^{-1}). Another option for chlorine atoms is to react with organics; rate constants for the reactions with organics are generally greater than the reaction of the chlorine atom with ozone.[1] Thus, a major pathway for chlorine radicals is to transform hydrocarbons into their respective hydrocarbon radicals,

$$Cl\cdot + RH \rightarrow HCl + R\cdot \quad (6)$$

Although plausible, the reaction of HCl with the hydroxyl radical is slow ($k_5 = 8.0 \times 10^{-13}$ cm^3 molecule^{-1} s^{-1}) and is not predicted to be a major source of chlorine atoms in the troposphere.[1,2] On the other hand, the hydrogen abstraction reaction by chlorine atoms (Equation 6) is generally faster than the corresponding process for the OH radical,[13] allowing for the possibility that a relatively small chlorine atom concentration could still play a significant role in atmospheric oxidations.

HBr and HI undergo similar reactions with OH to produce bromine and iodine atoms.[1,9,10] Bromine atom reactions with organic compounds are extremely slow and iodine atoms do not react at all with saturated or unsaturated organic compounds and so, instead of the tropospheric ozone formation observed with chlorine, bromine and iodine atoms result in ozone depletion.

1.4 Stratospheric Chemistry of Hydrogen Halides

In addition to the importance of the above reactions on tropospheric ozone concentrations, HCl also plays an important role in the stratosphere by serving as a chlorine reservoir molecule, thus, tying up chlorine atoms and controlling ozone destruction.[12,14] However, as first suggested by Farman *et al.*[15] in 1985 and then by Solomon *et al.*[16] in 1986, polar stratospheric clouds (PSCs) provide a surface to convert HCl into reactive chlorine, as shown in reactions 7-8.

$$HCl + HOCl \rightarrow Cl_2 + HNO_3 \quad (7)$$

$$HCl + ClONO_2 \rightarrow Cl_2 + HNO_3 \quad (8)$$

During the polar winter, the concentrations of chlorine accumulate and when the sunlight returns in the summer, the chlorine is photolyzed, generating chlorine atoms that can then induce ozone-destroying chain reactions.[12,17]

The heterogeneous reactions on PSCs have the additional consequence of removing nitrogen oxides from the gas phase. Reactions 7 and 8 generate nitric acid, which remains in the condensed phase on the PSC, causing "denitrification" of the stratosphere. As a result, the amount of NO_2 available to sequester active chlorine in the stable reservoir molecule, $ClONO_2$ via reaction 9, is reduced.

$$ClO + NO_2 + M \rightarrow ClONO_2 + M \qquad (9)$$

(M is a third body present to remove energy)

This denitrification further enhances the ozone depleting ability of PSCs.

Corresponding reservoir species, HBr and $BrONO_2$, are less abundant and possess shorter atmospheric lifetimes, but also play an important role in stratospheric heterogeneous chemistry leading to ozone loss.[18,19] Since bromine species are short-lived, the dominant heterogeneous bromine reactions are the reactions that allow the conversion of water into HO_x (HO_x=OH+HO_2), HCl into ClO and NO_x(NO_x=NO+NO_2) into HNO_3, as well as the rapid recycling of the bromine reservoir species.[18]

The reactivity of HI on atmospheric surfaces is not currently well understood, but recent studies have revealed that HI is efficiently taken up by ice at stratospheric temperatures.[19,20] As a result, iodide may also deplete ozone through its own catalytic cycles or through cycles with chlorine and/or bromine.

1.5 Sum Frequency Generation Background

Since the focus of this work is on the surfaces of aqueous solutions, a brief overview of sum frequency generation (SFG) theory is presented. A more in depth discussion of the theory of sum frequency generation can be found in the literature.[21-27]

SFG is a second-order nonlinear process in which two pulsed laser beams, one with infrared frequency, ω_{IR}, and one with visible frequency, ω_{Vis}, are overlapped in a medium in time and space, generating a photon at the sum of the frequencies, $\omega_{SFG} = \omega_{IR} + \omega_{Vis}$. Under the electric dipole approximation, the SFG process only occurs in noncentrosymmetric environments, such as an interface. The SFG intensity, I_{SFG}, is proportional to the square of the surface nonlinear susceptibility, $\chi^{(2)}$, which is a function of the sum frequency ($\omega_{SFG} = \omega_{IR} + \omega_{Vis}$) generated from a noncentrosymmetric media.

$$I_{SFG} \propto \left|P_{SFG}\right|^2 \propto \left|\chi_{NR}^{(2)} + \sum_{\nu}\left|\chi_{\nu}^{(2)}\right|e^{i\delta_{\nu}}\right|^2 I_{IR} I_{vis} \qquad (1)$$

P_{SFG} is the nonlinear second-order polarization, δ_{ν} is the phase factor, and I_{IR} and I_{vis} are the intensities of the incident visible and infrared beams. When the frequency of the incident infrared beam is resonant with a vibrational mode of an interfacial molecule, ν, the resonant susceptibility term, $\chi_{\nu}^{(2)}$, dominates and a SFG intensity enhancement is observed (the nonresonant term $\chi_{NR}^{(2)}$ is negligible).

Different polarization combinations of the incident and outgoing fields can be used to provide further information about the molecules at the interface. Liquid surfaces and interfaces are isotropic in the plane of the surface (i.e. the surface has $C_{\infty v}$ symmetry)

and thus, symmetry considerations[22] can reduce the surface susceptibility $\chi_s^{(2)}$, a 27-element tensor, to four independent nonzero elements:

$$\chi_{zzz}^{(2)}; \chi_{xxz}^{(2)} = \chi_{yyz}^{(2)}; \chi_{xzx}^{(2)} = \chi_{yzy}^{(2)}; \chi_{zxx}^{(2)} = \chi_{zyy}^{(2)} \tag{2}$$

where z is the direction normal to the interface.

These four different elements contribute to the VSFG signal under the four different polarization conditions PPP, SSP, SPS, and PSS, where the polarizations are listed in the order of decreasing frequency (sum frequency, vis, IR). P-polarized light is defined as having its electric field vector parallel to the plane of incidence and S-polarized light has its electric field vector perpendicular to the plane of incidence. The different polarization combinations are sensitive to the direction of the IR and Raman transition moments, where the PPP polarization combination includes all components of the resonant vibrational mode. Spectra acquired with different polarization combinations can be compared to determine molecular orientation, but the relationship is not simple.[28]

When describing the sum frequency response, the linear and nonlinear Fresnel factors must also be taken into consideration. These factors relate the electric fields in the medium to the incident and exiting fields and describe the extent of transmission and reflection of the light beams at the interface by considering the frequency, polarization, and the incident angle of the electromagnetic waves and the indices of refraction for the media at the boundary. The intensity of the sum frequency light emitted from the surface can be expressed in terms of the Fresnel coefficients, as in equations 3, a-d.

$$I_{ssp} \propto \left| F_i f_i f_z \chi_{iiz}^{(2)} \right|^2 \tag{3a}$$

$$I_{sps} \propto \left| F_i f_z f_i \chi_{izi}^{(2)} \right|^2 \tag{3b}$$

$$I_{pss} \propto \left| F_z f_i f_i \chi^{(2)}_{zii} \right|^2 \tag{3c}$$

$$I_{ppp} \propto \left| F_i f_i f_z \chi^{(2)}_{iiz} \right|^2 + \left| F_i f_z f_i \chi^{(2)}_{izi} \right|^2 + \left| F_z f_i f_i \chi^{(2)}_{zii} \right|^2 + \left| F_z f_z f_z \chi^{(2)}_{zzz} \right|^2 \tag{3d}$$

The subscripts on the intensity I denote the sum frequency, visible, and infrared polarizations, respectively. The subscript i denotes the x or y polarizations and the F and f are the Fresnel coefficients for the reflected and incident waves, respectively.

The resonant macroscopic nonlinear susceptibility, $\chi^{(2)}_{\upsilon}$, can be further broken down as shown in equation 4,

$$\chi^{(2)}_{\nu} \propto \frac{A_{\nu}}{\omega_{\nu} - \omega_{IR} - i\Gamma_{\nu}} \tag{4}$$

where A_{υ} is the amplitude of the transition moment, ν is the frequency of the transition moment, and Γ_{ν} describes the half-width at half-maximum (HWHM) of the transition. The sign of A_{ν} indicates whether a transition is out of phase with respect to the other transitions or if two transition moments exist anti-parallel with respect to each other; the resultant SFG response for both cases will then be 180º out of phase. The amplitude, A_{ν}, includes both the Raman and the infrared contributions; therefore, the SFG is allowed when the vibrational transition is both Raman and infrared active.

To further illustrate this point, the molecular susceptibility, $\beta_{lmn,\nu}$, can be described by equation 5,

$$\beta_{lmn,\nu} = \frac{\langle g | \alpha_{lm} | v \rangle \langle v | \mu_n | g \rangle}{\omega_{IR} - \omega_{\nu} + i\Gamma_{\nu}} \tag{5}$$

where $\langle g|\alpha_{lm}|\nu\rangle$ represents the Raman transition moment, $\langle \nu|\mu_n|g\rangle$ represents the IR transition moment for the molecule, and *lmn* represents the molecular coordinate system. An Euler angle transformation relates the molecular coordinate system (*l,m,n*) to the laboratory coordinate system (*I,J,K*). The transformation is shown in equation 6

$$\beta_{IJK,\nu} = \sum_{lmn} \mu_{IJK:lmn}\beta_{lmn,\nu} \tag{6}$$

where $\mu_{IJK:lmn}$ is the Euler angle transformation between the laboratory coordinates (*I,J,K*) and the molecular coordinates (*l,m,n*). The macroscopic susceptibility, $\chi^{(2)}_{IJK,\nu}$. can be calculated from the molecular susceptibility, $\beta_{IJK,\nu}$, as shown in equation 7,

$$\chi^{(2)}_{IJK,\nu} = N\langle\beta_{IJK,\nu}\rangle \tag{7}$$

where $\chi_{IJK,\nu}$ is equal to the number density, *N*, multiplied by the orientation average of $\beta_{IJK,\nu}$.

CHAPTER 2

EXPERIMENTAL

2.1 VSFG Scanning System and Experimental Details

The experimental setup of the Allen lab scanning VSFG system is shown in Figure 2.1 and has been described previously.[29] The SFG experiments were carried out using a visible beam at 532 nm and an infrared beam tunable from 2500 to 4000 cm^{-1} with a bandwidth of ~8 cm^{-1} generated from a KTP-KTA based optical parametric generator/amplifier (OPG/OPA) system (LaserVision). The 532 nm beam is generated by doubling the frequency (second harmonic) of the 1064 nm pump source from an EKSPLA PL 2143 A/SS Nd:YAG laser (29 ps pulse duration and 10 Hz repetition rate). The 532 nm beam is focused on the liquid surface using a plano-convex lens to yield a beam diameter of ~1 mm with a pulse energy of ~1.1 mJ. The IR beam is focused at the sample surface using a BaF_2 lens to yield a diameter of < 0.5 mm. The peak IR energy (at 3300 cm^{-1}) was ~350 μJ for the studies presented. The IR profile was measured simultaneously with the SFG spectrum by reflecting ~5% of the beam intensity onto an IR energy meter (J9LP, Molectron Inc.) using a BaF_2 window.

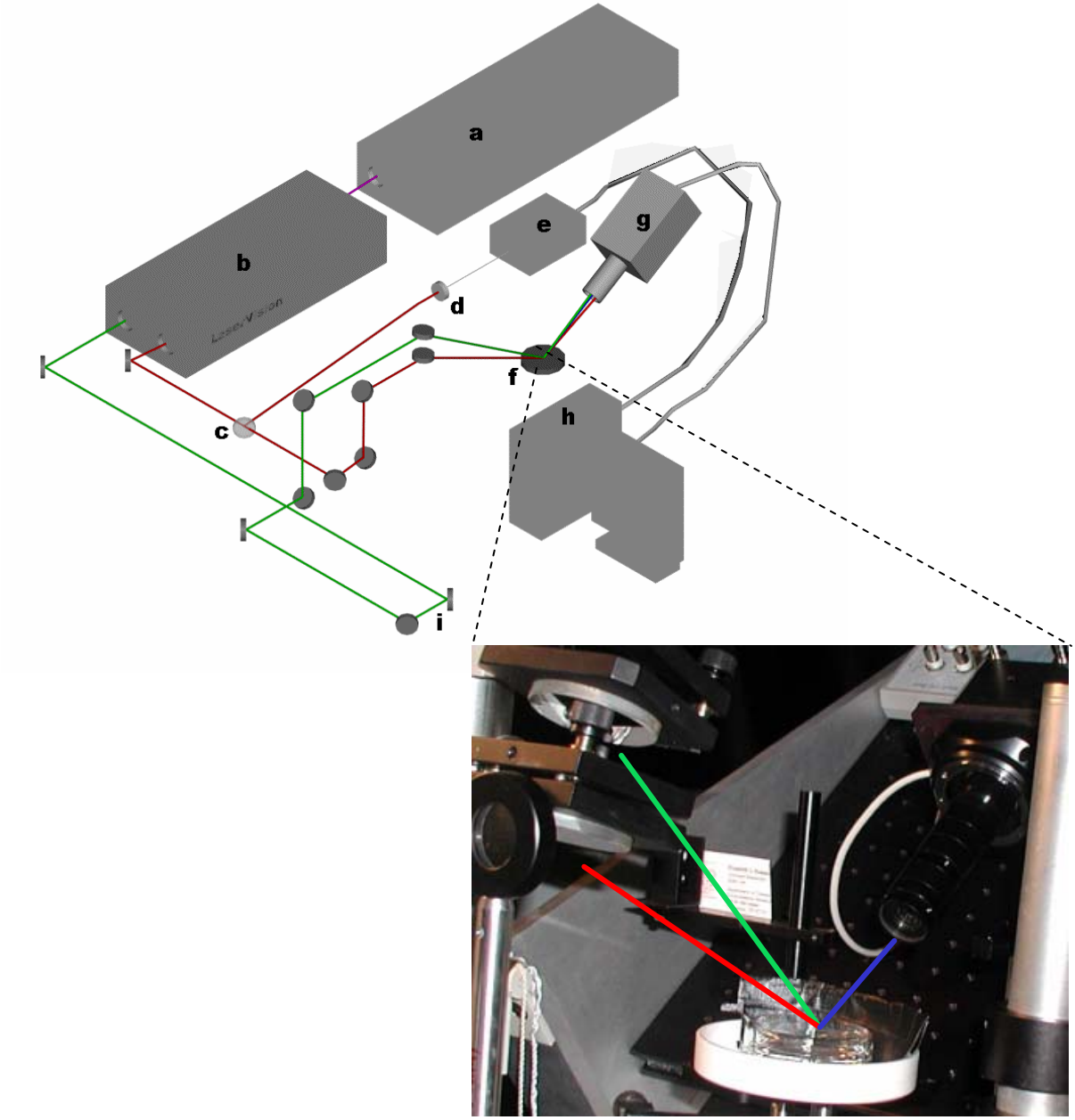

Figure 2.1: Schematic layout of the vibrational sum frequency generation scanning system: (a) EKSPLA Nd:YAG laser; (b) LaserVision OPA/OPG; (c) angled BaF_2 window; (d) infrared detector; (e) energy meter; (f) sample stage; (g) CCD; (h) control computer; (i) delay line. Green, red, blue and pink solid lines represent 532 nm, infrared, sum frequency, and 1064 nm, respectively. Digital picture shows the sample stage and the paths of the incoming and exiting beams.

The input angles were set to ~45° and ~53° from the surface normal for the 532 nm and IR beams, respectively. A 512 x 512 pixel back-illuminated charge coupled device (CCD) (Andor Technology, DV412) cooled to –42 °C was used to detect the sum frequency signal. A series of irises, a Schott glass filter (BG25), and two holographic Notch-Plus filters (Kaiser Optical Systems, Inc., HNPF-532.0-1.0) were used to block the 532 nm scattered light.

The SFG signal is optimized spatially and temporally at 3300 cm^{-1}. The VSFG spectra are normalized by the IR profile since the IR is detected in real time with the SFG intensity. The VSFG spectrum was also obtained from the surface of GaAs crystal, which accounts for any anomalies in the temporal and spatial overlap, and was comparable to the IR spectrum. The polarization combinations used for the SFG experiments are S, S, and P for the SFG, 532 nm, and infrared beams, respectively. Additional spectra with $S_{SFG}P_{vis}S_{IR}$ polarization were acquired for the acid solutions. All VSFG spectra were acquired at ~23 °C.

All of the SSP-polarized spectra presented in this thesis were acquired using a 15 s exposure time for each data point and were acquired in ~60 min (from 2800 to 3950 cm^{-1}). The VSFG spectra of the 1.2 M NaCl, NaOH and acid solutions were reproduced several times over the period of several months. The free O-H spectra of the 1.2 M HCl and HBr solutions are an average of three spectra and error bars are one standard deviation. The SPS-polarized spectra were acquired using a 45 s exposure time for each data point; the SPS-polarized spectra presented were divided by a factor of three in order to be comparable to the SSP-polarized spectra. At least one air-neat water

spectrum was acquired at the beginning and the end of the experiments to ensure the stability of the SFG system and to confirm reproducibility.

2.2 Raman Spectroscopy

Unpolarized Raman spectra were acquired at ~23 °C using ~87 mW from a 532 nm continuous wave (CW) laser (Spectra-Physics, Millennia II). The backscattered light was collected by a fiber optic probe (InPhotonics, RP 532-05-15-FC) coupled to the entrance slit of a 500 mm monochromator (Acton Research, SpectraPro 500i) using a 600 groove/mm grating blazed at 1 μm. The slit width was set to 20 μm, and the bandpass varied between 1.888 cm^{-1} (at 1500 cm^{-1}) and 1.366 cm^{-1} (at 4000 cm^{-1}). Data was collected to a liquid nitrogen cooled CCD camera (Roper Scientific, LN400EB, 1340 x 400 pixel array, back-illuminated and deep depletion CCD). SpectraSense software (Acton Research, version 4.1.9) was used for data collection and display.

Polarized Raman spectra (isotropic and anisotropic) were collected by passing the 532 nm light from the CW laser (Spectra-Physics, Millennia II, ~82 mW) onto the sample using the fiber optic probe (InPhotonics, RPS532/12-15). The scatter was focused onto the entrance slit of a 303 mm monochromator (Andor Technology, Shamrock 303i) using a BK7 lens. The scatter was dispersed using a 600 g/mm grating blazed at 500 nm and data was collected to a thermoelectrically cooled CCD camera (Andor Technology, DU440-BV, 2048 x 512 pixel array, back-illuminated, cooled to -70 ºC). Andor MCD software was used for data collection and display (Andor Technology, version 2.63.0.5). A 90° configuration for the incoming laser beam and detection was used and sheet

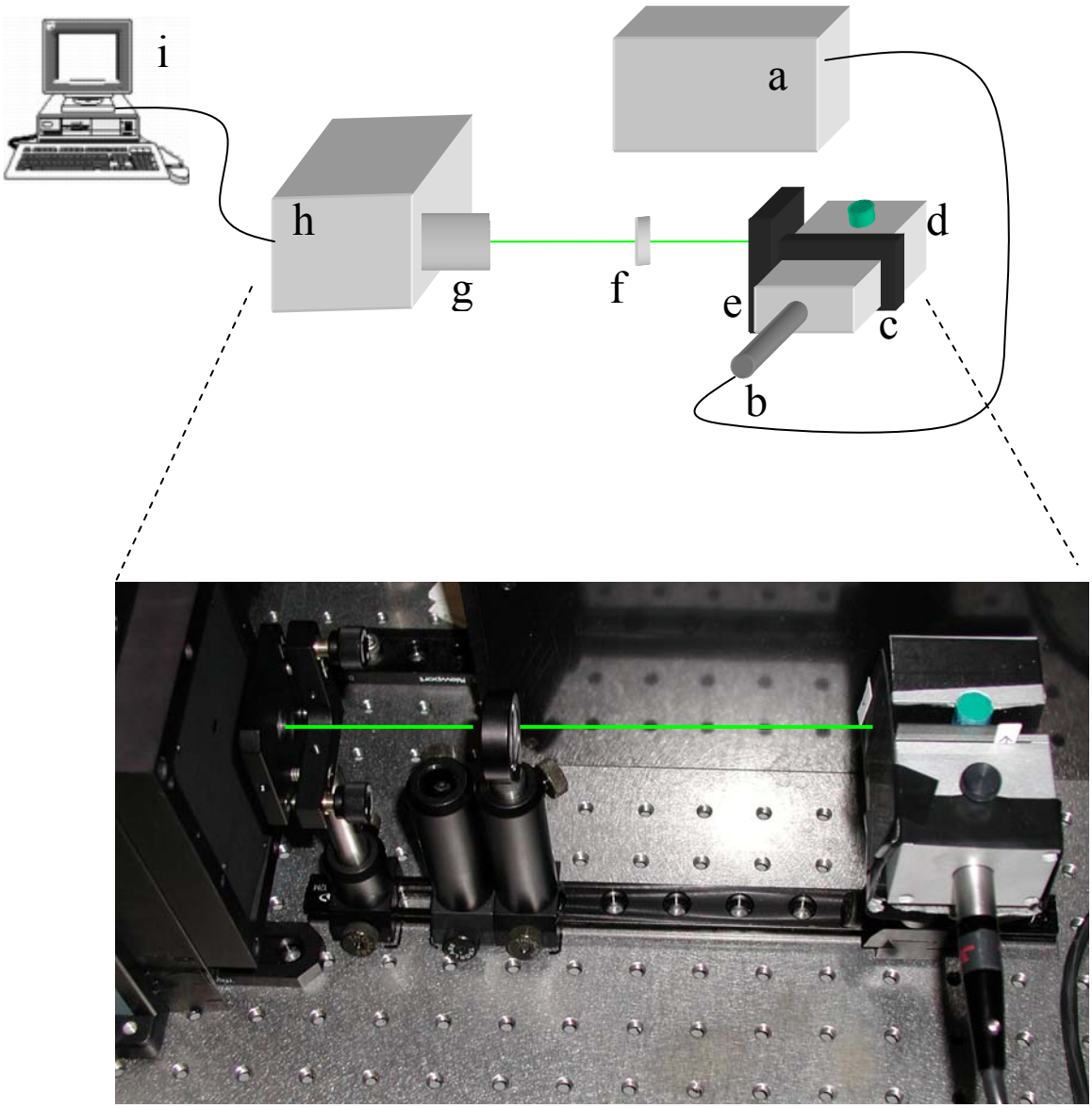

Figure 2.2: Schematic of polarized Raman setup: (a) Spectra-Physics Millennia II laser; (b) fiber optic Raman probe; (c) polarizing film; (d) sample holder; (e) polarizing film; (f) focusing lens; (g) Lyot depolarizer; (h) CCD and monochromator; (i) control computer. Digital picture shows the actual experimental setup.

polarizers were placed before and after the sample to select the polarization of the Raman scatter (Figure 2.2). A Lyot depolarizer (Thorlabs, LDPOL) was placed in the light path before the monochromator since there is a polarization dependence for the diffraction grating. Unpolarized Raman spectra were also acquired using this system and the spectra were consistent with the spectra obtained from the system using the SpectraPro 500i monochromator from above. The slit width was set to 50 μm and the bandpass varied between 16.3 cm^{-1} (at 1500 cm^{-1}) and 12.0 cm^{-1} (at 4000 cm^{-1}). The acquisition temperature was ~23 °C.

Both CCD cameras were calibrated using the 435.83 nm line of a fluorescence lamp and the wavenumber position was confirmed by taking a spectrum of crystalline naphthalene and comparing peak positions with the literature values.[30]

2.3 ATR-FTIR Spectroscopy

A Thermo Nicolet FTIR spectrometer (Avatar 370, Thermo Electron Corporation) was employed in the ATR-FTIR (attenuated total reflection Fourier transform infrared) spectroscopy experiments. A 45° single bounce silicon crystal trough ATR accessory (Smart SpeculATR, Thermo Electron Corporation) was used to collect the spectra at a spectral resolution of 4 cm^{-1} at ~24 °C. The spectra were averaged over 64 scans.

2.4 Spectral Fits

All spectral fits were performed using the software package IGOR (version 4.0.5.1). For the VSFG spectra, a Lorentzian fitting function, written by Dr. Elizabeth Hommel[31] of the Allen lab, to incorporate phase was used to fit the spectra. For the Raman and ATR-FTIR spectra, built in line algorithms were used to fit the spectra to

Voigt line shapes. Fitting parameters were obtained from the IGOR program. The plot_lor_peaks() command provided the peak positions, amplitudes, and HWHM (Γ_ν); the FWHM was obtained by multiplying Γ_ν by two; the print areaxy command provided the peak areas. The value for Γ_ν was confirmed through the use of a Mathcad 2000 program (Appendix B) written by Dr. Dingfang Liu of the Allen lab, which calculates the VSFG spectrum from the IGOR provided peak positions, amplitudes, and Γ_ν according to equations 1 and 4.

The VSFG spectrum describes the SFG intensity (I_{SFG}) as a function of the incident infrared frequency (ω_{IR}) and can be mathematically fit according to equations 1 and 4. When performing the fit, a constant complex number is used as the nonresonant term $(\chi^{(2)}_{NR})$ and the sign of the amplitude (A_ν) is used to denote the phase of the photons of the vibrational mode from the interfacial molecules, which incorporates orientation and relative vibrational phases. Equation 4 indicates the Lorentzian line shape in the VSFG spectrum fitting. In Raman and IR fitting, the intensity is the summation of each vibration's intensity $\left(|A|^2 + |B|^2\right)$, whereas in SFG the intensity is the absolute square of the summation of each vibration's $(\chi^{(2)}_\nu)$ and $(\chi^{(2)}_{NR})$ as shown in equation 1. This leads to different spectral characteristics for VSFG spectra relative to Raman and IR spectra. Therefore, VSFG spectra interpretation must occur after deconvolution into the component peaks because direct comparison of VSFG spectra to Raman and IR spectra may be misleading, particularly for the broad bands of the hydrogen-bonding region (3000-3600 cm^{-1}).

2.5 Surface Tension

Surface tensions were measured using a surface tensiometer (DeltaPi, Kibron Inc.), which employs the Wilhelmy Plate technique. A minor modification in the technique was made in that a wire probe was used instead of a thin plate. The solutions were contained in Teflon wells for the measurements. Surface tension measurements were collected at ~25 °C and are an average of three values.

2.6 Chemicals

Water was obtained from a Millipore Nanopure system (18.3 MΩ·cm). Acid solutions were made volumetrically from concentrated HCl (Fisher Scientific, 36.5 wt. %), HBr (Fisher Scientific, 48 wt. %) and HI (Alfa Aesar, 47 wt. %). A 56.5 wt. % HI solution (Alfa Aesar) was also examined, but its dark color caused difficulties in acquiring the Raman and VSFG spectra due to absorption of the 532 nm light. To prevent the HI solutions from reacting with light, solutions were stored in a dark cabinet and the flasks were covered with aluminum foil. In addition, HI solutions were made no more than one day in advance of their use to help ensure no reaction with light occurred.

Sodium chloride and sodium hydroxide solutions were prepared volumetrically from certified ACS grade chemicals purchased from Fisher Scientific. The 10 mol % and 20 mol % deuterated solutions were prepared volumetrically from 100.0 atom % D_2O Acros Organics). The 1.2 M NaCl, HCl and HBr deuterated solutions were then prepared volumetrically using the 10 mol % D_2O solution. All of the solutions were checked for organic contamination by obtaining the VSFG spectra of the solutions in the region between 2800 and 3000 cm^{-1}.

CHAPTER 3

1.2 M AQUEOUS SOLUTIONS

The ATR-FTIR and Raman spectra of bulk neat water and the SSP-polarized VSFG spectrum of the air-neat water interface in the O-H stretch region (2900-3900 cm^{-1}) are shown in Figure 3.1, a-c, respectively, along with their calculated fits and component peaks.

The broad peaks in the 3000-3600 cm^{-1} region contain three bands positioned at ~3250, ~3400, and ~3550 cm^{-1} in the IR, Raman, and VSFG spectra. The peak assignments for bulk water are assigned by defining the basic unit as being composed of four oscillating dipoles in a tetrahedral arrangement around an oxygen atom.[32] The peak at ~3250 cm^{-1} in the IR (3223 cm^{-1}) and Raman (3237 cm^{-1}) spectra is attributed modes within a hydrogen-bonding network that have primarily symmetric stretch character.[32] The peaks at ~3400 cm^{-1} (IR: 3398 cm^{-1}, Raman: 3449 cm^{-1}) and ~3550 cm^{-1} (IR: 3576 cm^{-1}, Raman: 3621 cm^{-1}) correspond to modes that have antisymmetric stretch character.[32] The differences in the 3400 cm^{-1} and 3550 cm^{-1} peak frequencies can be attributed to the strengths of the hydrogen bonds.[33]

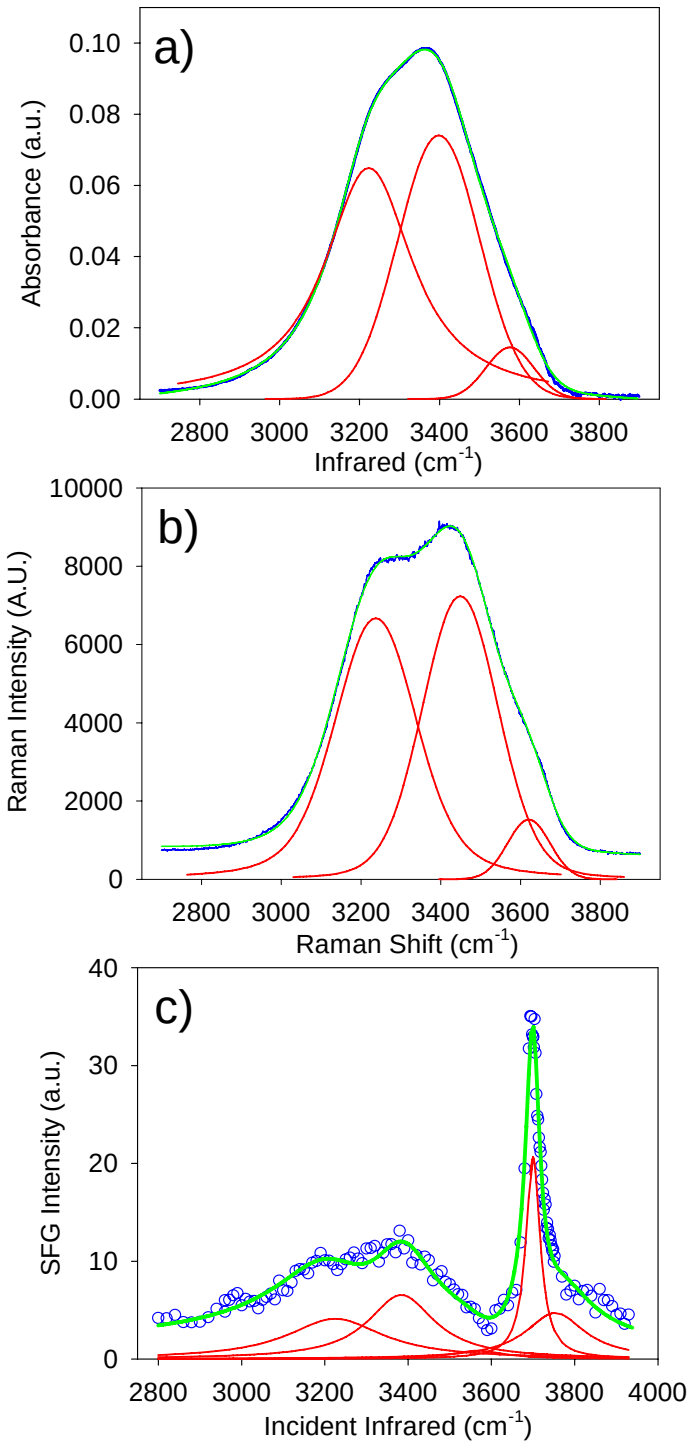

Figure 3.1: (a) ATR-FTIR spectrum of neat water, (b) Isotropic Raman spectrum of neat water, (c) SSP-polarized VSFG spectrum of air-neat water interface. The component peaks are shown in red and the calculated spectra from the spectral fits are shown in green.

The assignments of surface water O-H stretches are based on recent cluster work.[33-35] The ~3250 cm^{-1} peak in the VSFG spectrum is attributed to the bonded O-H of the 3-coordinate water molecules at the surface that are single proton donor – double proton acceptor (DAA) molecules (Figure 3.2a).[33-35] The 4-coordinate water molecules (double proton donor – double proton acceptor, DDAA) at the surface exist as distorted tetrahedrons due to its existence in the interfacial region (Figure 3.2b); the O-H stretches of these molecules contribute to the ~3400 cm^{-1} peak in the VSFG spectrum.[33-35] The ~3550 cm^{-1} peak in the VSFG spectrum arises from the O-H stretch of 3-coordinate double proton donor – single proton acceptor (DDA) molecules (Figure 3.2c).[33-35] The VSFG spectrum (Figure 3.1c) also contains a narrow peak at 3700 cm^{-1}, which is assigned to the dangling O-H (free O-H) stretch of water molecules bridging the air-aqueous interface with one uncoupled O-H bond directed into the vapor phase[36-38] and the other interacting through hydrogen bonding with the liquid phase as described above within the ~3250 cm^{-1} peak assignment (Figure 3.2a).[33-35]

SFG intensity is also observed on the high-frequency side of the free O-H peak at 3743 cm^{-1}. In aqueous ammonia VSFG spectra, Shultz *et al.*[39] found that the free O-H consists of two components: a narrow resonance at 3700 cm^{-1} and a broad peak extending ~100 cm^{-1} beginning at 3680 cm^{-1}. Yet, the origin of this intensity is not well understood. There is evidence from IR spectroscopic studies on amorphous ice surfaces supporting the assignment to the dangling O-H from doubly coordinated water molecules.[32,40] Recent IR spectroscopic studies of Vaden *et al.*[41] provide evidence this peak is due to stretches of alkali metal cluster ions ($M^+(H_2O)Ar$). In addition, recent IR studies of water in CCl_4 (l) suggests frustrated rotational modes exist in this spectral region.[42] Thus, a

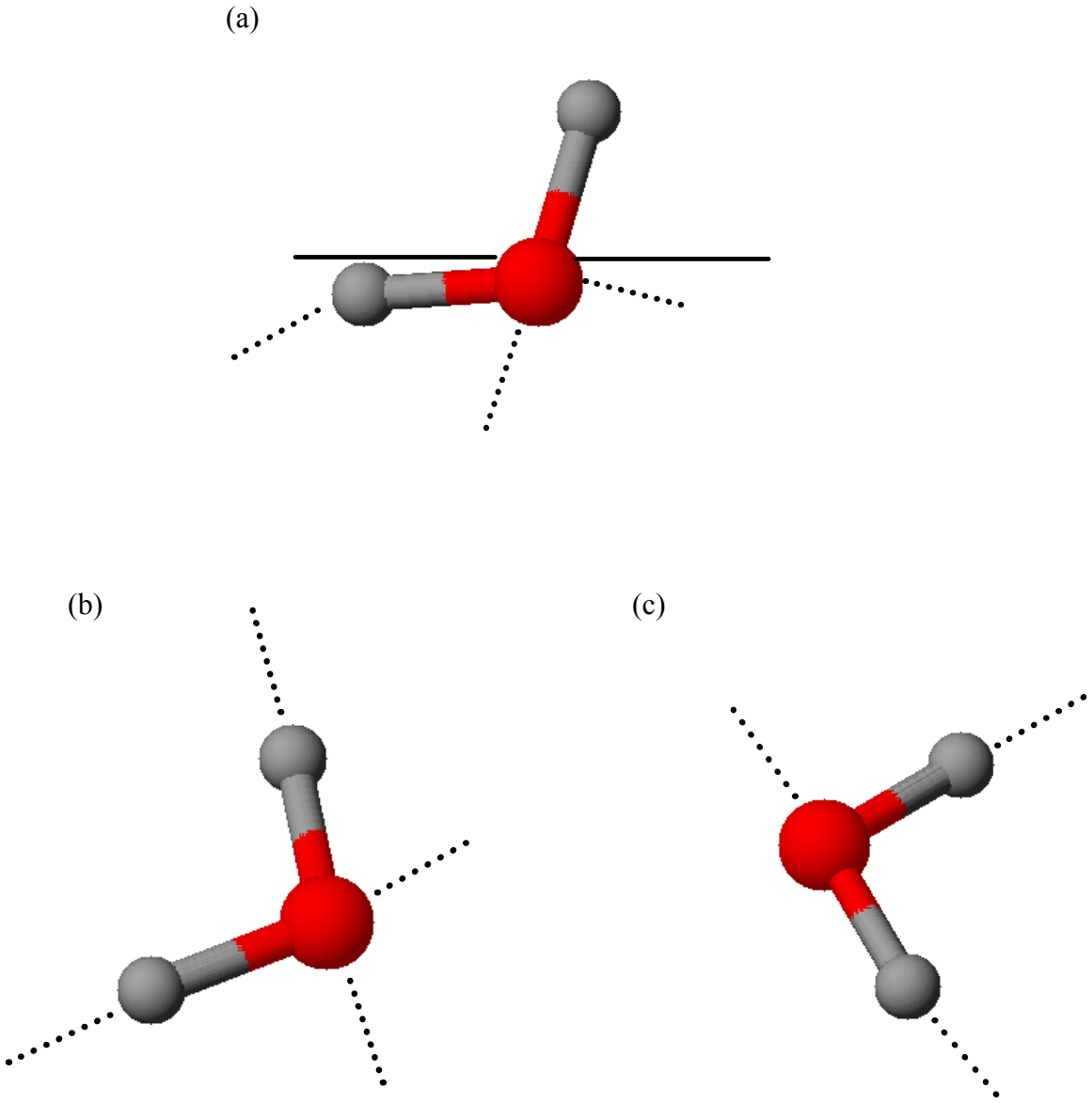

Figure 3.2: Molecular diagrams of the different contributors to the hydrogen-bonded O-H stretches of water in the VSFG spectrum (a) 3-coordinate DAA water molecules at the surface (hydrogen-bonded O-H: ~3250 cm^{-1}; free O-H: ~3700 cm^{-1}), (b) 4-coordinate (distorted tetrahedron) water molecules (~3450 cm^{-1}), (c) 3-coordinate DDA water molecules (~3550 cm^{-1}).

component peak on the high-frequency side of the free O-H is used to fit the VSFG spectra since a nonresonant component did not compensate for the resonant like feature particularly in the HBr and HI spectra as well as in previous sodium halide spectra.[29]

3.1 ATR-FTIR and Raman Spectra of 1.2 M Solutions

The bulk hydrogen-bonding structure of water after the addition of an inorganic salt (sodium chloride, NaCl), base (sodium hydroxide, NaOH) and acids (hydrochloric, HCl, hydrobromic, HBr, and hydriodic, HI, acids) was examined by obtaining IR and Raman spectra. The ATR-FTIR spectra of the 1.2 M aqueous solutions are shown in Figure 3.3. Spectral assignments were made after deconvoluting the spectra into component peaks as shown in Figure 3.4, a-f (calculated fits are shown in green). The isotropic Raman spectra (polarized parallel to the electric field vector of the incident vertically polarized laser beam) of the 1.2 M aqueous solutions are shown in Figure 3.5.

It is important to note that the intensity between 1500 and ~2800 cm^{-1} observed in the Isotropic Raman spectra is an artifact of the system and is due to the 532 nm Rayleigh line rather than any vibrational modes in the aqueous solutions; unpolarized Raman spectra of the 1.2 M aqueous solutions were obtained on the system using the SpectraPro monochromator for confirmation (Figure 3.6a) and no Raman intensity was observed on this system. The isotropic and anisotropic (polarized perpendicular to the electric field vector of the incident vertically polarized laser beam) Raman spectra are also shown in Figure 3.6b and 3.6c, respectively. As in the IR spectra, spectral assignments were made after deconvolution of the spectra into component peaks as shown in Figure 3.7, a-f, with the calculated fits shown in green. The peaks in the water O-H stretching region of the IR

and Raman spectra are assigned to the modes with primarily symmetric stretch character at ~3250 $cm^{-1}$and the modes with antisymmetric stretch character at ~3400 cm^{-1} and ~3550 cm^{-1}.

Fitting of the NaOH and acid (HCl, HBr, and HI) ATR-FTIR spectra is complicated by the presence of hydroxide and proton hydration complexes.[43-46] These complexes have a broad absorption in the IR spectra and fitting the aqueous NaOH and acid spectra requires the inclusion of an additional peak. The peak positions, amplitudes, full width at half maximum (FWHM), and peak areas for the IR and Raman spectra are shown in Table 3.1.

Upon the addition of NaCl to water, the IR (Figure 3.3) and Raman (Figure 3.5) spectra show a decrease in the 3250 cm^{-1} peak and an increase in the 3400 cm^{-1} peak. When NaOH is added to water, the IR and Raman spectra reveal little change in the hydrogen-bonding region of water. However, the IR spectrum of the NaOH aqueous solution reveals a substantial intensity enhancement in the region between ~1500 and ~3100 cm^{-1}; this enhancement is also observed in the Raman spectrum, but is less pronounced. With the addition of acid (HCl, HBr, and HI) to water, the IR spectra show a decrease in the 3250 cm^{-1} peak and a decrease and narrowing of the 3400 cm^{-1} peak. The Raman spectra of the acids show a decrease in the 3250 cm^{-1} peak accompanied by an increase and narrowing of the 3400 cm^{-1} peak. In both the Raman and IR spectra of acids, the observed trends in the hydrogen-bonding region are enhanced when going from HCl to HBr to HI. The broad intensity enhancement between ~1500 and ~3100 cm^{-1} observed in the spectra of NaOH is also present in the IR spectra of the acid solutions and to a lesser extent in the acid Raman spectra.

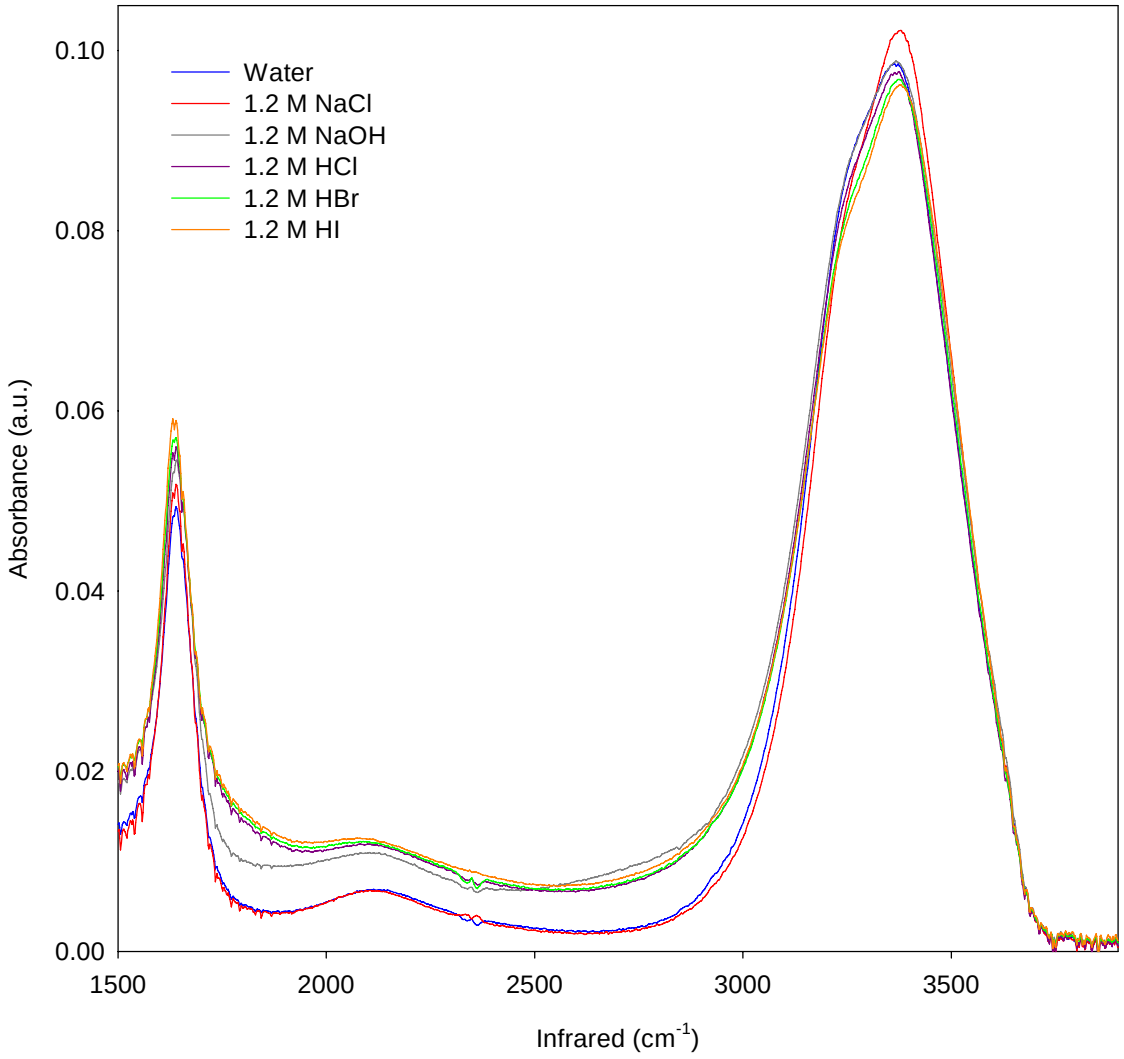

Figure 3.3: ATR-FTIR spectra of 1.2 M aqueous solutions compared to that of neat water.

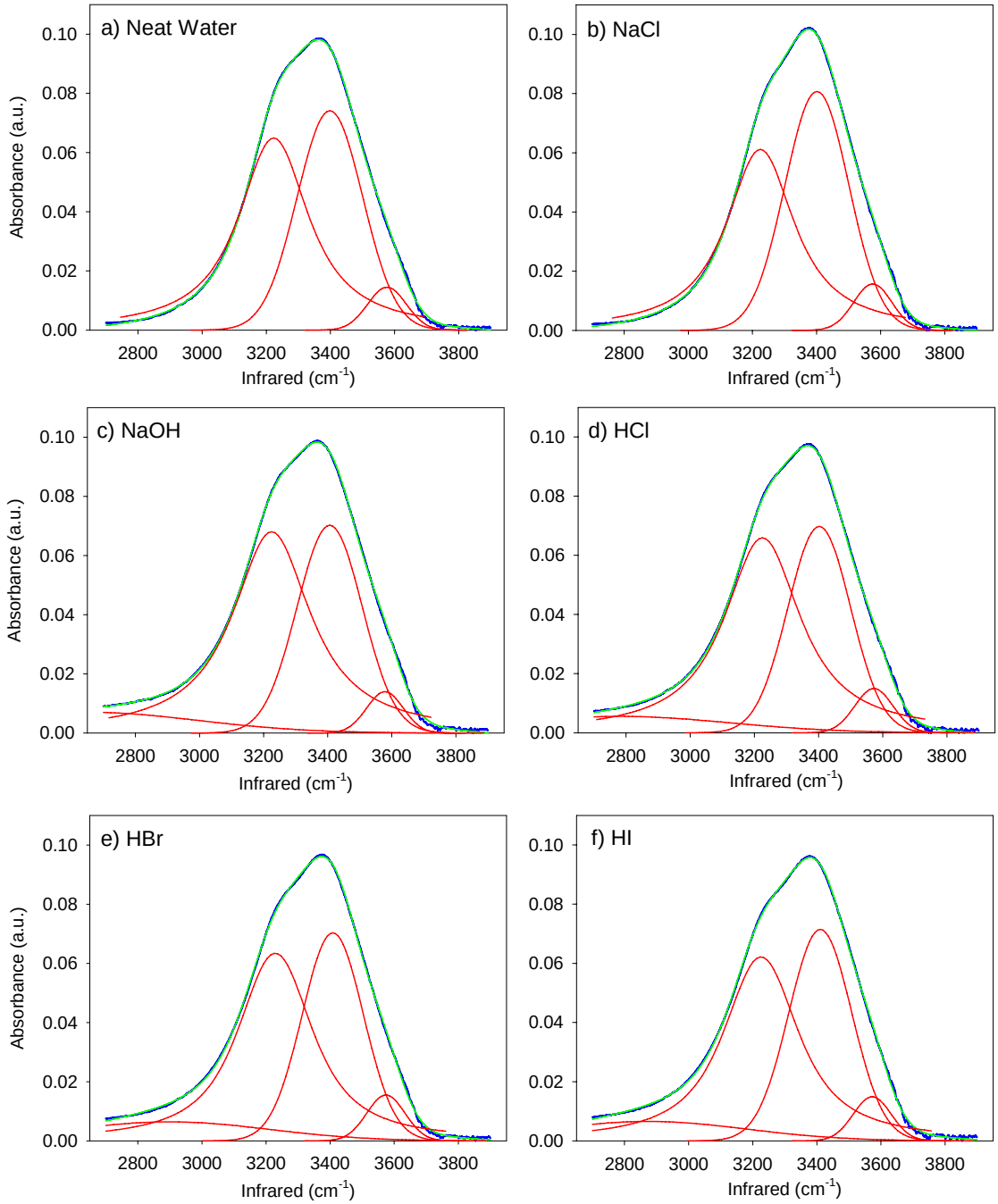

Figure 3.4: Spectral fits of ATR-FTIR spectra of 1.2 M aqueous solutions (a) Neat Water, (b) NaCl, (c) NaOH, (d) HCl, (e) HBr, (f) HI. Component peaks are shown in red and the calculated fits from the component peaks are shown in green.

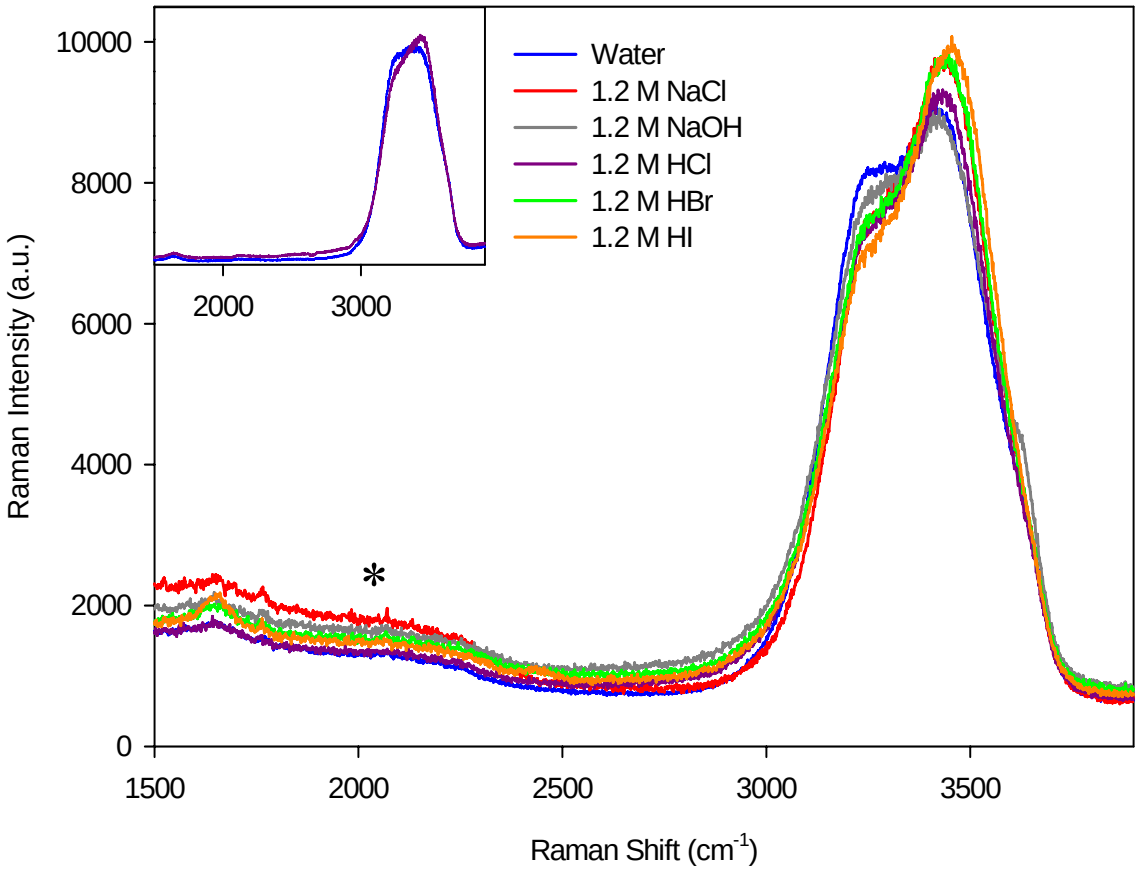

Figure 3.5: Isotropic Raman spectra of 1.2 M aqueous solutions compared to that of neat water. * The intensity between 1500 and ~2800 cm^{-1} is an artifact of the polarized Raman system arising from the 532 nm Rayleigh line. The inset shows the unpolarized Raman spectra of neat water and 1.2 M HCl.

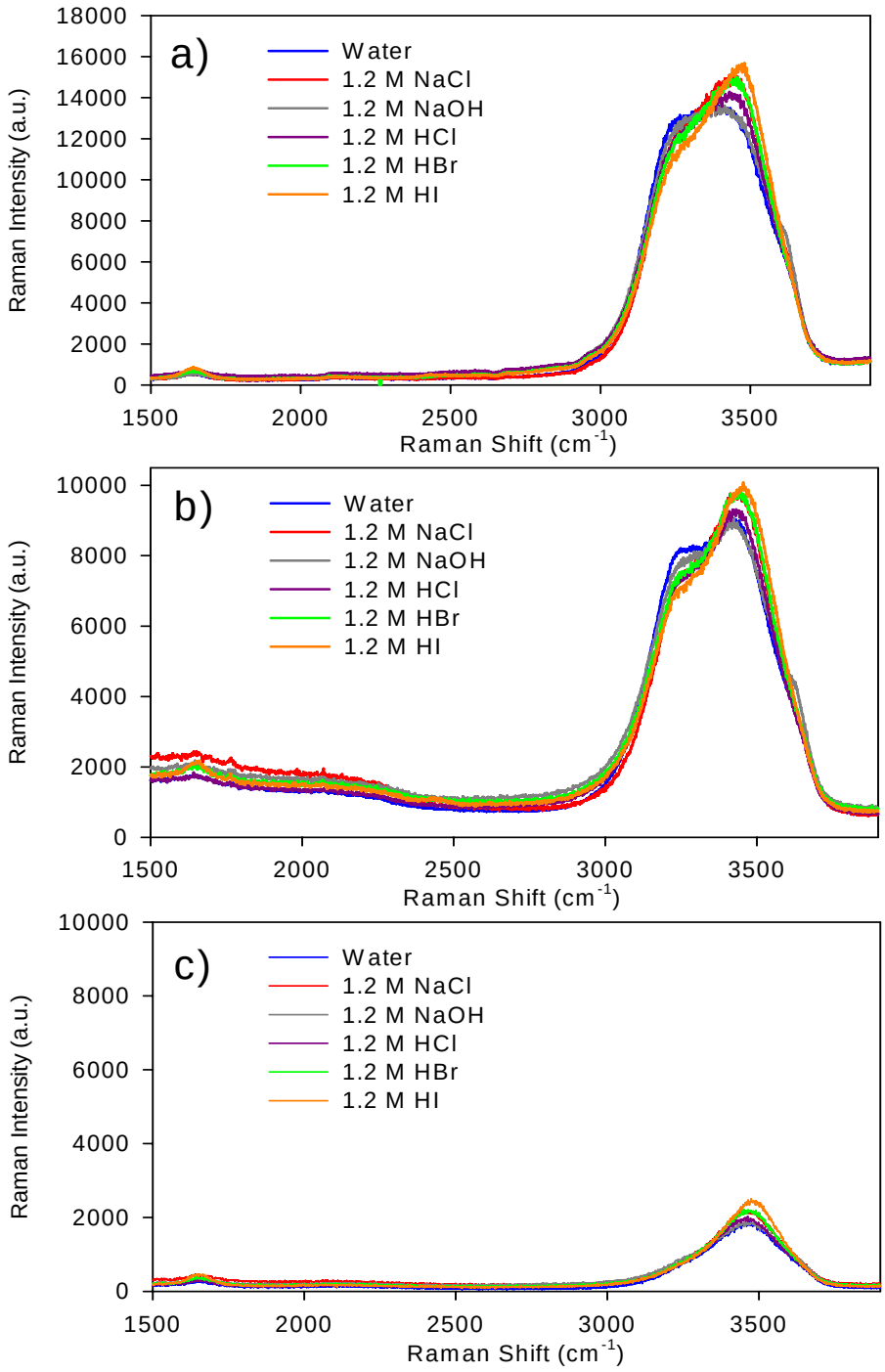

Figure 3.6: Raman spectra of 1.2 M aqueous solutions compared to that of neat water (a) Unpolarized Raman spectra, (b) Isotropic Raman spectra, (c) Anisotropic Raman spectra. The unpolarized spectra were acquired using the system with the SpectraPro monochromator; the polarized spectra were acquired using the system with the Shamrock monochromator.

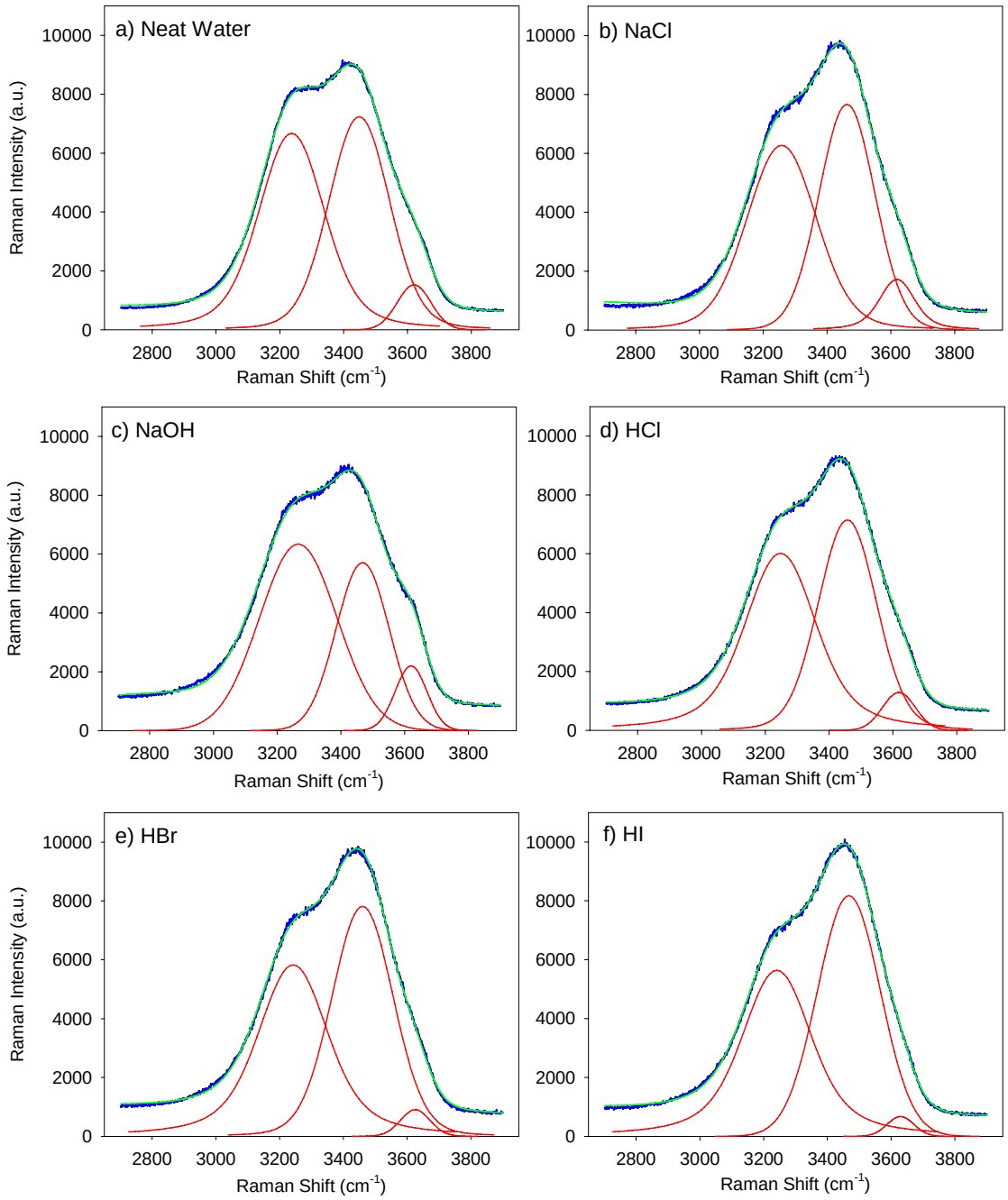

Figure 3.7: Spectral fits of the isotropic Raman spectra of 1.2 M aqueous solutions (a) Neat Water, (b) NaCl, (c) NaOH, (d) HCl, (e) HBr, (f) HI. Component peaks are shown in red and the calculated fits from the component peaks are shown in green.

	ATR-FTIR				Raman			
	Peak Position (cm^{-1})	Amplitude (A_v)	FWHM	Area	Peak Position (cm^{-1})	Amplitude (A_v)	FWHM	Area
Neat Water	3223.0	0.0937	262.8	26.45	3237.1	7013.3	241.0	1.96×10^6
	3398.4	0.0741	240.8	18.99	3449.0	7360.2	223.3	1.82×10^6
	3576.4	0.0145	141.8	2.18	3620.9	1525.6	125.0	2.03×10^5
1.2 M NaCl	3224.8	0.0890	256.0	24.28	3257.8	6412.7	255.8	1.84×10^6
	3401.3	0.0807	235.9	20.27	3462.4	7695.0	206.1	1.71×10^6
	3575.4	0.0157	140.2	2.34	3619.3	1864.1	129.8	2.88×10^5
1.2 M NaOH	2645.6	0.0071	821.1	6.16				
	3224.9	0.1040	293.7	31.20	3266.3	6338.4	286.3	1.93×10^6
	3406.2	0.0702	239.9	17.93	3468.2	5708.9	196.2	1.19×10^6
	3578.5	0.0139	134.3	1.99	3620.1	2198.6	117.7	2.76×10^5
1.2 M HCl	2781.0	0.0055	810.7	4.77				
	3225.0	0.0954	285.1	29.14	3247.9	6529.1	261.4	2.03×10^6
	3402.2	0.0697	230.7	17.13	3457.5	7236.3	214.9	1.71×10^6
	3572.5	0.0149	140.6	2.24	3619.0	1288.6	121.2	1.66×10^5
1.2 M HBr	2899.5	0.0064	728.6	4.99				
	3228.6	0.0808	273.8	25.91	3242.6	6357.9	255.8	1.93×10^6
	3408.3	0.0703	225.3	16.87	3460.2	7910.9	226.3	1.97×10^6
	3573.8	0.0155	140.3	2.31	3625.6	908.1	108.7	1.07×10^5
1.2 M HI	2873.8	0.0066	725.1	5.07				
	3225.8	0.0810	276.9	25.94	3241.5	6200.1	255.0	1.89×10^6
	3410.9	0.0715	231.2	17.59	3467.6	8175.1	232.2	2.02×10^6
	3572.7	0.0149	139.2	2.21	3629.4	672.8	99.1	7.10×10^5

Table 3.1: Parameters for ATR-FTIR (Figures 3.3, a-f) and Raman (Figures 3.5, a-f) spectral fits of 1.2 M aqueous solutions.

The changes in the hydrogen-bonding region of the IR and Raman spectra upon the addition of NaCl and acid (HCl, HBr, and HI) relative to that of neat water is attributed to the water molecules breaking their symmetric hydrogen-bonding network to solvate the ions. The addition of ions to water disrupts the symmetric stretch character of the tetrahedral hydrogen-bonding network, and thus a decrease in the 3250 cm^{-1} peak intensity. The resulting increase in modes with anti-symmetric stretch character is observed in the increase of the 3400 cm^{-1} peak intensity of the Raman spectra. The greater intensity enhancement of the 3400 cm^{-1} peak in the Raman spectrum of NaCl versus that for HCl can be attributed to the solvation of both a sodium cation and a chloride anion, whereas in HCl, the cation (H^+) is not necessarily solvated, but rather forms a different species (i.e. H_3O^+ or $H_5O_2^+$). The trend in the 3400 cm^{-1} peak in the acid solutions is associated with an increase in the size and polarizability of the anion in solution ($Cl^- < Br^- < I^-$).

The differences in the hydrogen-bonding region of the IR and Raman spectra of the 1.2 M solutions can be attributed to the different selection rules; for a mode to be IR active, the vibration must cause a change in dipole moment and for a mode to be Raman active, there must be a change in polarizability with the vibration. As acids with increasingly polarizable anions ($Cl^- < Br^- < I^-$) are added, the water molecules solvating these anions exhibit increased polarizability; thus, since Raman intensities arise from this condition, the effect is observed in the Raman spectra. Additionally, the amplitudes in the IR spectra are not the actual absorption cross sections, but the product of these with the

coupling of the respective intramolecular motions to intermolecular excitation along the hydrogen bonds.[33] The polarity of the H_3O^+ and $H_5O_2^+$ ions also responsible for the strong proton continuum in the IR spectra but a weak Raman spectrum.[47]

The broad band, between ~1500 and ~3100 cm^{-1}, present in the IR spectra (Figure 3.3) and to a lesser extent in the Raman (Figure 3.5) spectra of the acids arises from H_3O^+ and $H_5O_2^+$ groupings.[43-45,48-50] The excess proton in the $H_5O_2^+$ groupings fluctuates very rapidly between the two water molecules due to the presence of a double-minimum or a broad flat potential well; this potential well makes the hydrogen-bonds extremely polarizable. Large polarizabilities result in various strong interactions (i.e. induced dipole interactions with ions and with dipole fields of the solute and solvent molecules and with each other) and distort the energy surfaces of the hydrogen-bonds in $H_5O_2^+$.[43,44,49-51] The distortion of the energy surfaces results in the photons in the hydrogen bonds having a continuous energy level distribution and thus, a continuum in the IR and Raman spectra is observed.[43,44,51] The continua present in the acid solutions (Figures 3.3 and 3.5) are also observed in the spectra of aqueous base solutions;[46] however, instead of the continua arising from $H_5O_2^+$ groupings, the continua result from $H_7O_4^-$ and $H_9O_5^-$ groupings.

3.2 VSFG Spectra of 1.2 M Solutions

The structure of the air-aqueous interface of 1.2 M aqueous solutions of a sodium chloride (NaCl), sodium hydroxide (NaOH), hydrochloric acid (HCl), hydrobromic acid (HBr), and hydriodic acid (HI) was investigated using vibrational SFG spectroscopy; the resulting SSP-polarized VSFG spectra are shown in Figure 3.8. The inset of Figure 3.8 shows an expanded view of the free O-H region of neat water and the 1.2 M HCl and

HBr solutions. Spectral fits of the VSFG spectra after deconvolution into the component peaks with the calculated fits (green solid lines going through the majority of data points) are shown in Figure 3.9, a-f. The corresponding fitting parameters including relative phases (+ versus -) of the amplitude terms are shown in Table 3.2.

The region between 2800 cm^{-1} and 3950 cm^{-1} of the VSFG spectra of aqueous solutions is comprised of the single proton donor – double proton acceptor (DAA) molecule stretch at ~3250 cm^{-1},[33-35] tetra-coordinated interfacial water molecule stretch at ~3400 cm^{-1},[33-35] the double proton donor – single proton acceptor (DDA) molecule stretch at ~3550 cm^{-1},[33-35] and the dangling O-H stretch at ~3700 cm^{-1}.[36-38] These assignments are the same as that for neat water (Figure 3.2). However, in the acid solutions, the VSFG spectra contain an additional broad band centered at ~3200 cm^{-1} due to the vibrational modes of H_3O^+ and $H_5O_2^+$.

The VSFG spectra (Figure 3.8) reveal very different behavior for the acids versus the sodium halide and sodium base air-aqueous interfaces, whereas in the bulk aqueous solutions (Figure 3.3 and 3.5), the sodium halide, sodium base, and hydrogen halides all had similar effects on the hydrogen-bonding structure. For the sodium halide, NaCl, and sodium base, NaOH, the resulting VSFG spectra nearly overlap the neat water VSFG spectrum, indicating the hydrogen-bonding environments of the air-aqueous interface of 1.2 M NaCl and 1.2 M NaOH aqueous solutions are not significantly affected by the addition of sodium, chloride and hydroxide anions. On the other hand, the SSP-polarized surface vibrational SFG spectra of 1.2 M HCl, HBr, and HI aqueous solutions are

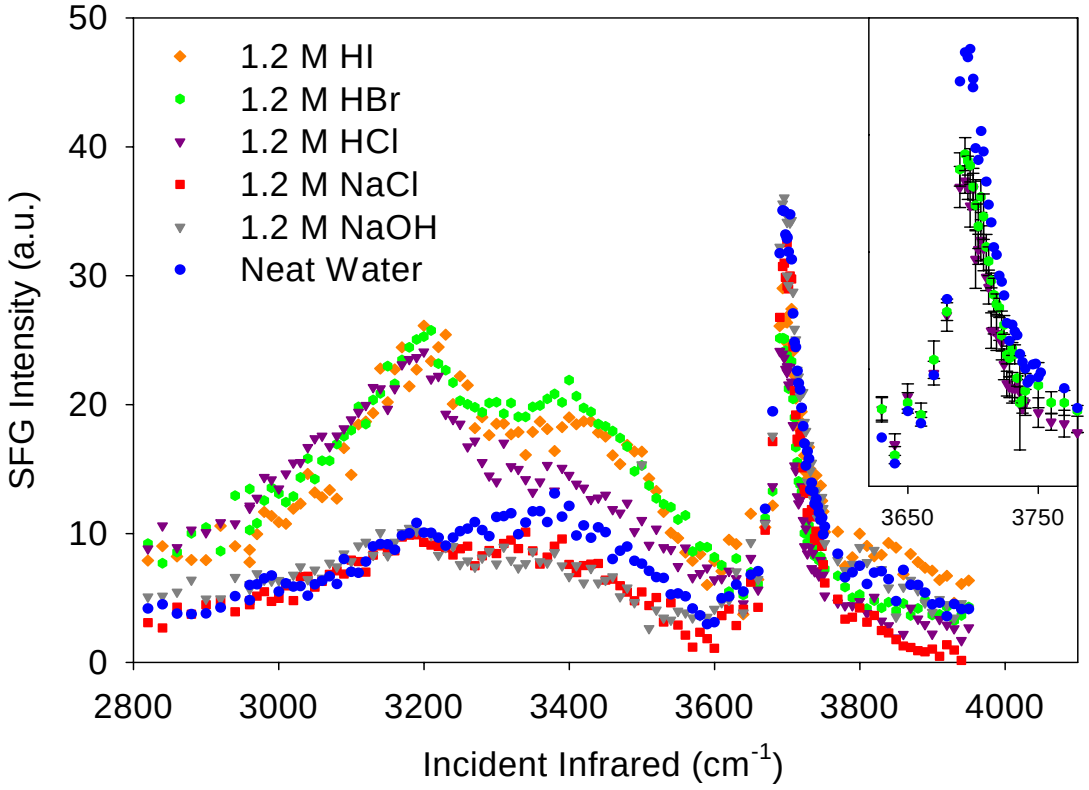

Figure 3.8: SSP-polarized VSFG spectra of 1.2 M solutions compared to that of neat water. Inset: Expanded view of the free OH region for neat water, 1.2 M HCl, and 1.2 M HBr (standard deviations are shown as error bars).

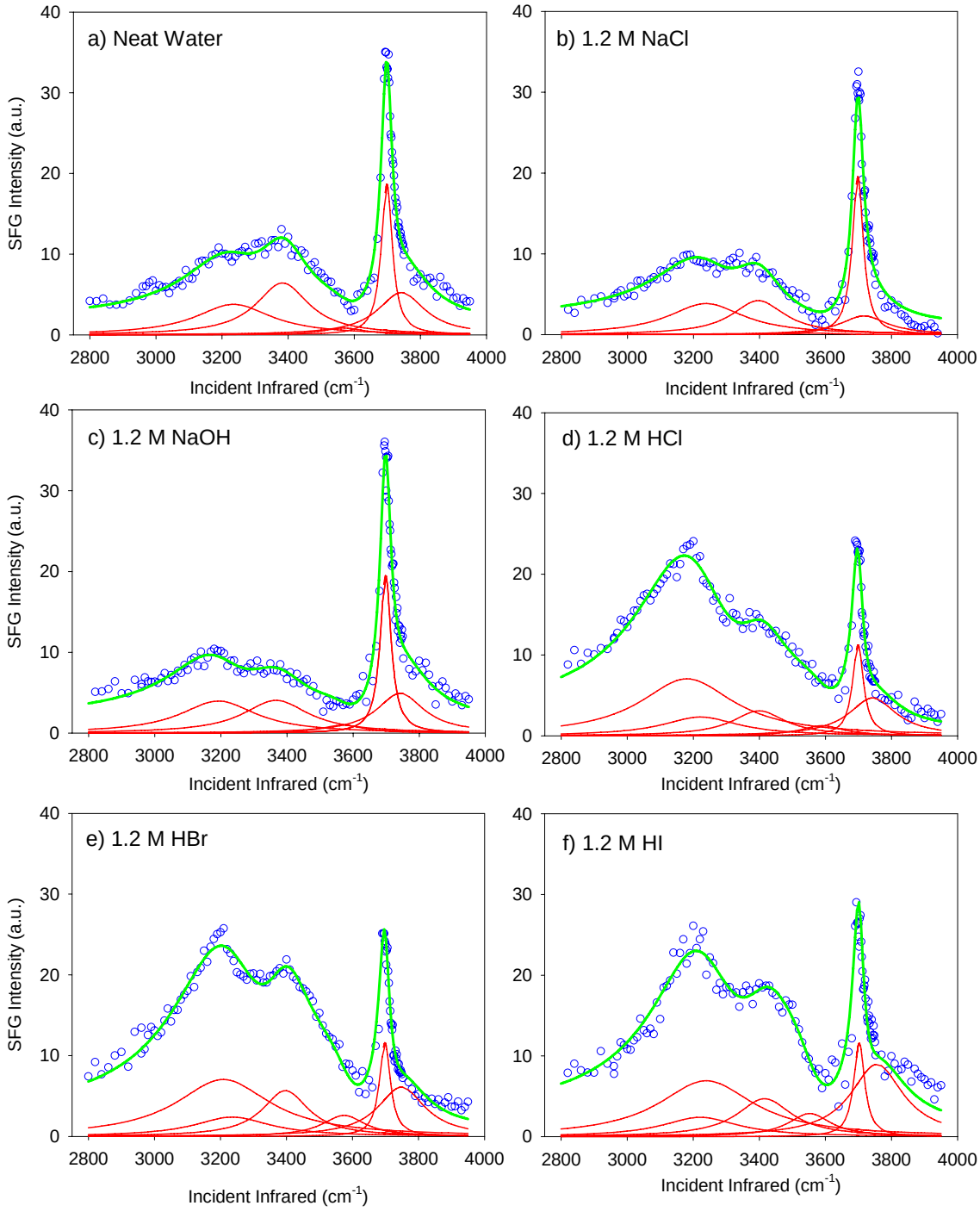

Figure 3.9: Spectral fits of SSP-polarized VSFG spectra of 1.2 M solutions (a) Neat Water, (b) NaCl, (c) NaOH, (d) HCl, (e) HBr, (f) HI. Component peaks are shown in red and the calculated fits from the component peaks are shown as green lines that go through most of the data points.

	Non-Resonant Term	Peak Position (cm^{-1})	Phase	Amplitude (A_v)	Γ_v	FWHM	Area
Neat Water	-1.2187 + 0.17749*i*	3234.8	+	274.2	141.0	282.0	1404.6
		3382.9	+	247.5	97.6	195.2	1761.8
		3568.8	-	72.1	78.5	157.0	187.8
		3698.8	-	86.6	20.0	40.0	1140.1
		3742.7	-	198.9	86.9	173.8	1207.4
1.2 M NaCl	-1.2187 + 0.17749*i*	3238.2	+	276.3	140.9	281.8	1427.5
		3396.7	+	200.2	97.6	195.2	1152.3
		3568.8	-	34.3	78.5	157.0	42.5
		3698.3	-	88.6	20.0	40.0	1193.0
		3716.5	-	132.0	86.9	173.8	539.5
1.2 M NaOH	-1.2187 + 0.17749*i*	3192.4	+	280.5	140.9	281.8	1459.0
		3366.8	+	243.6	121.0	242.0	1336.9
		3568.8	-	78.1	78.5	157.0	220.4
		3698.7	-	88.5	20.0	40.0	1190.0
		3742.7	-	192.6	86.9	173.8	1132.2
1.2 M HCl	-1.2187 + 0.17749*i*	3180.6	+	461.7	173.9	347.8	3052.7
		3221.8	+	214.5	140.9	281.8	858.3
		3398.7	+	171.5	97.6	195.2	845.8
		3589.2	-	87.8	78.5	157.0	277.5
		3698.8	-	67.3	20.0	40.0	688.0
		3742.7	-	188.0	86.9	173.8	1079.0
1.2 M HBr	-1.2187 + 0.17749*i*	3208.3	+	461.7	173.9	347.8	3074.4
		3235.7	+	218.0	140.9	281.8	888.0
		3394.0	+	202.6	88.1	176.2	1321.3
		3574.1	-	126.8	78.5	157.0	580.2
		3698.3	-	68.3	20.0	40.0	708.3
		3748.2	-	214.7	86.9	173.8	1402.0
1.2 M HI	-1.3024 + 0.15035*i*	3239.2	+	461.8	175.4	350.8	3062.7
		3221.0	+	218.0	140.9	281.8	886.1
		3415.7	+	219.4	101.1	202.2	1329.0
		3552.6	-	133.0	78.5	157.0	640.7
		3702.4	-	68.3	20.0	40.0	710.0
		3755.8	-	288.5	96.3	192.6	2228.6

Table 3.2: Parameters for VSFG spectral fits of 1.2 M solutions.

significantly different from the VSFG spectrum of the neat water surface. The acid solutions show an intensity enhancement in both the 3250 cm^{-1} and 3400 cm^{-1} peak and a decrease in the 3700 cm^{-1} peak intensity.

The acid VSFG spectra (Figure 3.8) reveal an enhancement in the 3400 cm^{-1} peak, relative to neat water. This peak, which is assigned to tetra-coordinated interfacial water molecules, increases according to the size and polarizability of the anion ($Cl^- < Br^- < I^-$) and is attributed to water molecules solvating the anions at the surface and thus disrupting the hydrogen-bonding network in the interface, as seen in the bulk solution studies of the 1.2 M solutions. This enhancement is consistent with previous studies on the sodium halide air-aqueous interfaces.[29]

The IR and Raman spectra (Figures 3.3 and 3.5, respectively) show that the intensity of the 3250 cm^{-1} peak decreases for all acid solutions when compared to water. Conversely, the VSFG spectra show a significant intensity increase in the 3250 cm^{-1} peak with the addition of acid as shown in Figure 3.8. Possible reasons for this increase in intensity include: 1) an increase in the infrared and Raman transition moments, 2) the formation of an electric double layer, 3) an increase in interfacial depth, and/or 4) contribution from H_3O^+ and $H_5O_2^+$ vibrational intensities. Examination of the infrared and Raman spectra permits the exclusion of Reason 1, since these spectra show no peak enhancement in the 3250 cm^{-1} peak intensity, but rather a decrease in intensity. Reason 2 (electric double layer formation) can also be excluded based on recent molecular dynamics simulations on aqueous solutions of HCl, HBr, and HI.[52] For HCl, both the hydronium cations and the chloride anions are present at the air-aqueous interface, with both showing a slight surface ion enhancement. The density profiles for HBr and HI

show a similar picture, except that bromine and iodine are more surface enhanced than chloride or hydronium. These simulations reveal that the separation of cations and anions at the aqueous-air interface is not extensive and the formation of an electric double layer at the surface of aqueous acid solutions is unlikely.

Reason 3 (increase in the interfacial depth) is a potential explanation for the enhancement of the 3250 cm^{-1} peak in the VSFG spectra of the acids. Sum frequency generation intensity (SSP polarization) is enhanced when probing larger numbers of water molecules and/or an increased alignment of the symmetric stretch transition moment of water molecules along the surface normal; an interfacial depth increase (defined by an increase in noncentrosymmetry at the surface) will increase the number of water molecules probed.

The differences in the air-aqueous interface arising from the different halide ions and the H_3O^+ and $H_5O_2^+$ ions can be examined by plotting the additive peak areas (integrated from 2800 to 3600 cm^{-1} to include the distribution of the tails) of the 3200, 3250, 3400, and 3550 cm^{-1} component peaks (Figure 3.10). The VSFG additive intensity increases from that of neat water to that of HI. Recall that the VSFG intensity is related to the Raman and IR intensities (Equation 5); if one compares the product of the Raman and IR intensities with the VSFG intensity, information can be obtained about the air-aqueous interface. The increase for the VSFG intensity is considerably larger than that for the Raman x IR (Figure 3.10), indicating the number of water molecules existing in the interfacial region increases with 1) the addition of H_3O^+ and $H_5O_2^+$ and 2) the size and polarizability of the halide anion. Specifically, the interface becomes larger with the addition of the H_3O^+ and $H_5O_2^+$ ions and halide anions, with iodide causing the most

substantial increase. This explanation is consistent with molecular dynamics simulations which also reveal an increase in the interfacial depth upon addition of hydrogen halides (HCl, HBr, and HI) to water[52] and the observed increase in interfacial depth in sodium halide aqueous solutions both by experimental studies[29] and MD simulations.[53,54]

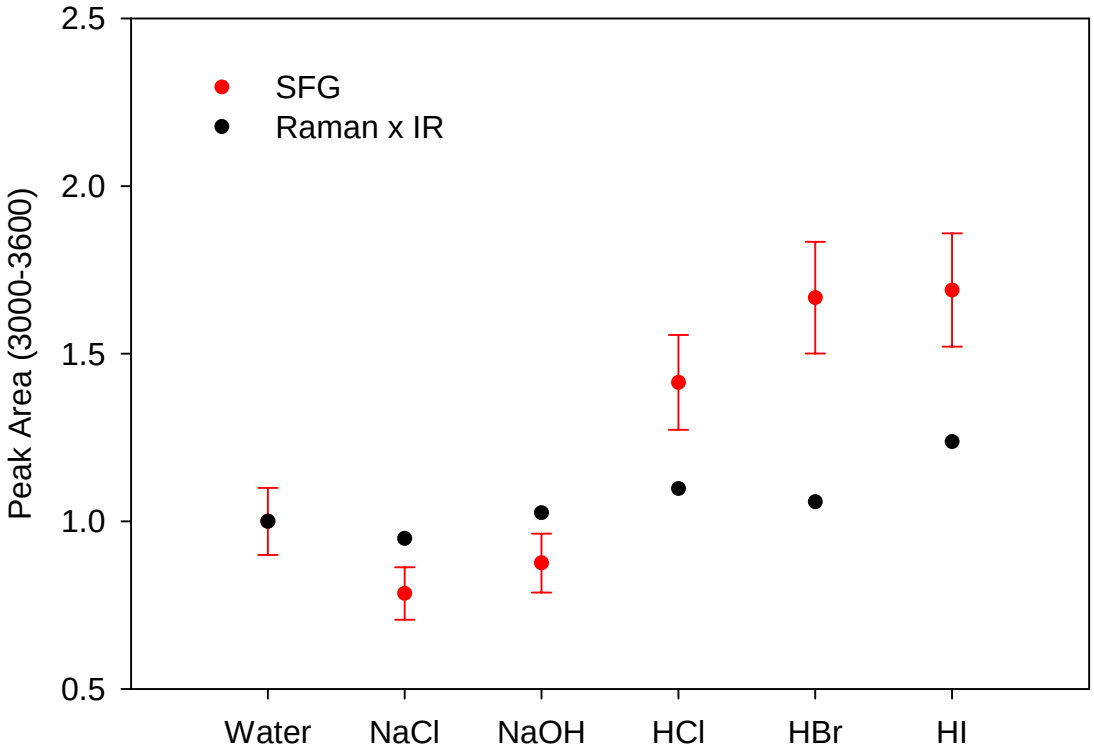

Figure 3.10: The areas of the 3200, 3250, 3400, and 3550 cm^{-1} (approximate, positions varied) peaks in the O-H stretch region for Raman x infrared (Raman area multiplied by ATR-FTIR area) and the SFG for the 1.2 M aqueous solutions. Areas were normalized to neat water. Error bars are estimated to be approximately 10%, based on experimental values.

Reason 4 (contribution from H_3O^+ and $H_5O_2^+$ vibrational intensities) is also a likely explanation based on recent molecular dynamics simulations[52,55] that show the hydronium ion has a weak affinity for the surface of aqueous acid solutions with a preferred orientation with the hydrogens pointing towards the aqueous phase and oxygen towards the vapor phase. The O-H stretching frequencies of the hydronium ion are detected and contribute to the VSFG intensity.

Much work has been done on the vibrational spectroscopy of H_3O^+ and $H_5O_2^+$ ions that supports the O-H vibrational frequencies observed here in the VSFG spectra of acids.[43-45,47-50,56] Falk and Giguere observed strong, broad absorption bands in the in infrared spectrum of aqueous acid solutions at about 1205, 1750, and 2900 cm^{-1} and attributed them to the hydronium ion.[47] Janoschek *et al.* were able to calculate the IR continua observed in aqueous solutions of strong acids and bases by taking into account distributions of electrical field strengths and O-O distances. These calculations were able to reproduce the continua observed in aqueous solutions of HCl and H_2SO_4.[57]

More recently, Yeh *et al*. observed the gas phase infrared spectra of the hydrated hydronium cluster ions $H_3O^+ \cdot (H_2O)_n$ (n = 1, 2, 3) from 3550 to 3800 cm^{-1}; for $H_5O_2^+$, two features are visible, a broad, featureless band at 3608.8 cm^{-1} and a higher frequency band centered at 3684.4 cm^{-1}.[56] Kim *et al*. investigated the infrared spectra of HCl and HBr aqueous solutions and observed a continuous absorption from 1000 to 3400 cm^{-1} and three broad bands at 1760, 2900, and 3350 cm^{-1}, which are attributed to the hydrated proton.[45] Graham and Roberts have also examined the infrared spectrum of the $HCl \cdot 6\ H_2O$ complex; vibrational modes centered at 1770 and 1275 cm^{-1} and the broad peak between 2500 and 3100 cm^{-1} were assigned to the ν_4, ν_2, and ν_3 modes of H_3O^+,

respectively.[58] Finally, McCoy and coworkers[49,50] have explored the properties of the ground state and OH fundamentals of $H_5O_2^+$ and the predissociation spectra of the shared proton oscillations in the $H_3O_2^-$ and $H_5O_2^+$ systems.

The complex nature of bulk water is not yet well understood. Neutral water clusters have become a focus of interest by providing a molecular level starting point into understanding both bulk phase properties of water as well as the extent to which water's properties are modified at surfaces.[33,34,59-62] In the last thirty years, extensive studies have also been done on the structure of protonated water clusters;[63-68] such studies can help provide insight about the surface structure of acidic aqueous solutions. Kassner and Hagen[69] were the first to propose the cluster ion $(H_2O)_{21}H^+$ exists in a clathrate-like pentagonal dodecahedron with the H_3O^+ residing either 1) in the center of the cage or 2) on the surface. Wei *et al.*[64] has provided experimental evidence suggesting the H_3O^+ lies in the center of the cage based on ion intensity distribution studies of trimethylamine (TMA) and its stability in mixed cluster ions of $(H_2O)_n(TMA)_m{\cdot}H^+$. Extra stability of the cluster is observed when the structure adopts the maximum hydrogen-bonding configurations, i.e. H_3O^+ becomes the core ion; these results support the Monte Carlo simulations by Nagashima *et al.*[70] and Svanberg and Pettersson.[65]

Recently, experimental[67,68] and theoretical[66,67] studies have found evidence that supports the idea that H_3O^+ resides on the surface of the clathrate cage, thus displacing a neutral water molecule to the cage center. Using infrared spectroscopy, Shin *et al.*[67] found the intensity of the free O-H vibrational bands in $H^+(H_2O)_n$ (n=6 to 27) varies characteristically depending on whether the water molecule is two- or three-coordinated. Electronic structure calculations by coauthors Christie and Jordan[67] compliment these

studies in finding the structure with an interior H_3O^+ were higher in energy than clusters with H_3O^+ on the exterior. Miyazaki *et al*.[68] also have used infrared spectroscopy to study the hydrogen-bonding network in clusters of $H^+(H_2O)_n$ (n=4 to 27) and their dependency on the cluster size. These studies revealed that as the number of water molecules grow from $n < 10$ to $\sim 10 < n < 21$ to $n > 21$, the hydrogen-bonded network structure goes from a chain structure to a two-dimensional net structure to a three-dimensional cage structure. The results of the cluster studies presented above provide support for the notion that H_3O^+ is present in the interface of aqueous acid solutions.

The VSFG spectra of the acid solutions also reveal a decrease in the 3700 cm^{-1} peak intensity, as shown in the inset of Figure 3.8, relative to neat water. Since this peak is attributed to the free O-H stretch at the air-aqueous interface, upon the addition of acids, the surface water structure undergoes a structural reorganization that reduces the number of O-H bonds projecting into the air. This decrease in the free O-H peak intensity is not dependent on the identity of the anion, within the experimental error as shown in the inset of Figure 3.8.

Currently, there is no clear physical understanding of the restructuring of the surface water molecules, although some postulates can be excluded. Changes in orientational distribution have been ruled out from polarized VSFG studies. SPS-polarized VSFG spectra were acquired and the resulting spectra are plotted in Figure 3.11 along with the SSP-polarized spectra of water for comparison. No enhancement in the free O-H stretching region of the SPS-polarized VSFG spectra, confirming the number of free hydroxyl groups is decreased rather than orientated differently with the addition of

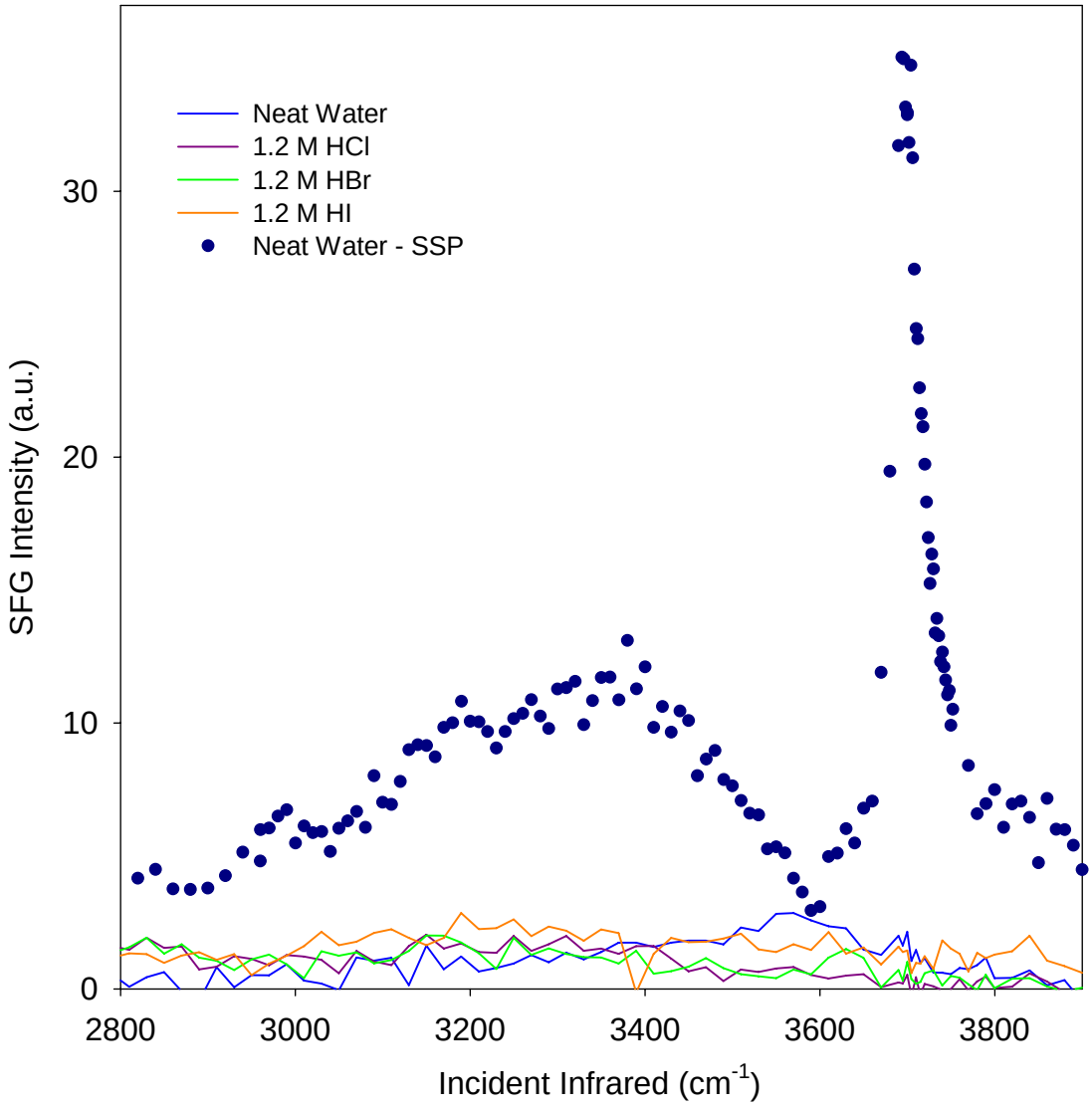

Figure 3.11: SPS-polarized VSFG spectra of neat water and 1.2 M HCl, HBr, and HI. The SSP-polarized neat water spectrum is plotted for comparison.

acid. Reorientation of the free O-H bonds to hydrogen bond with the oxygens of the hydronium ions is also not a rational explanation since there is a hydrophobic region on the lone-pair side of the oxygen in the hydronium ion.[55]

The observed decrease in the free O-H peak intensity of the VSFG spectra is consistent with recent molecular dynamics simulations.[52] The surface density (number per unit area) of free O-H bonds was calculated for the aqueous solutions of NaCl, NaOH, HCl, and HBr and compared to that for neat water. In the salt and base solutions, the density of free O-H bonds is about the same as neat water, whereas in HCl and HBr, there is a significant reduction in the surface density. The lack of changes in the surface orientation distribution is also confirmed through angular distribution calculations.[52]

The broad O-H stretch peaks in the hydrogen-bonding region of water make it difficult to provide a detailed description of the hydrogen-bonding region at the air-aqueous interface. To simplify the O-H stretch region and thus, clarify the peak assignments, VSFG spectra were obtained for 10 mol % and 20 mol % D_2O solutions and the 1.2 M NaCl, HCl, and HBr aqueous solutions in which 10% (by mole fraction) of the H_2O molecules were replaced by D_2O. The resulting SSP-polarized spectra are shown in Figure 3.12. The ATR-FTIR and isotropic Raman spectra of the deuterated solutions were also acquired to allow for comparison between the air-liquid interface and the bulk water structure of the deuterated aqueous solutions and are shown in Figure 3.13. Although the spectra of the deuterated solutions did not simplify the hydrogen-bonded O-H stretch peak assignments to the extent expected, the observed trends were consistent with previous isotopic dilution studies,[71-74] as well as the pure water studies.

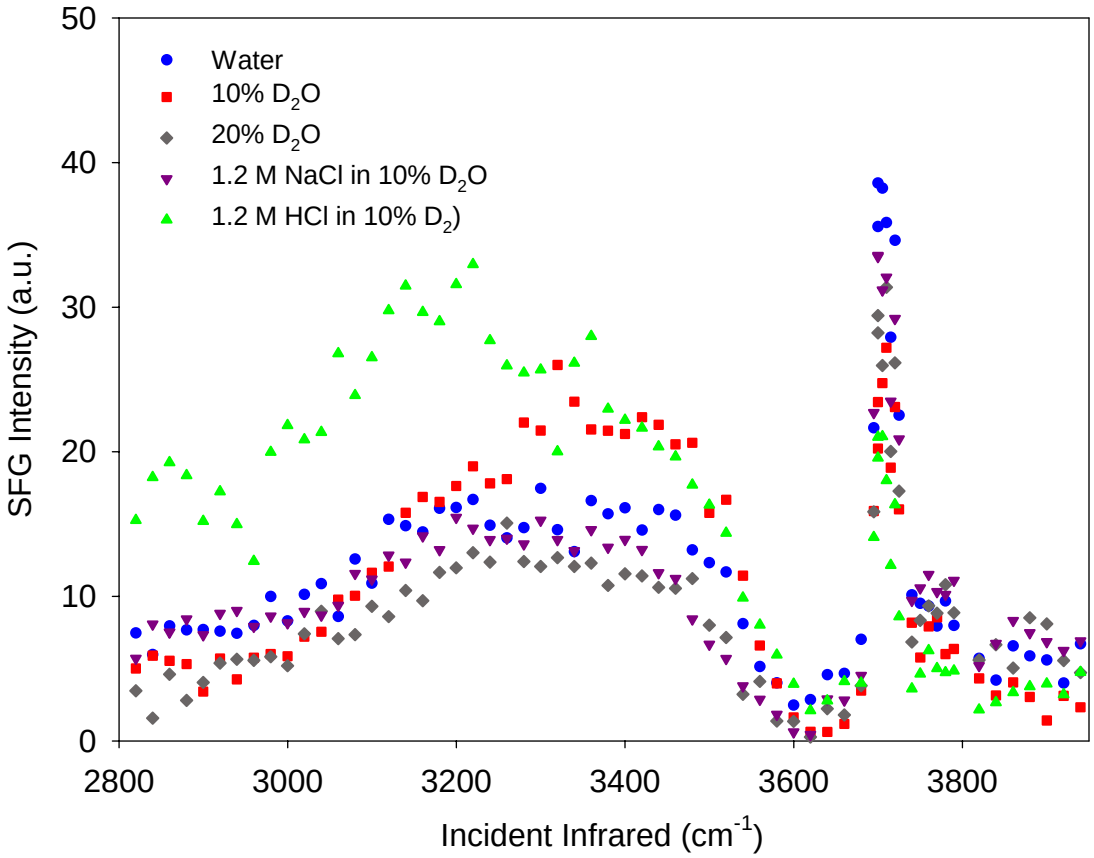

Figure 3.12: SSP-polarized VSFG spectra of neat water, 10 mol % and 20 mol % D_2O and 10 mol % deuterated solutions of 1.2 M NaCl and HCl.

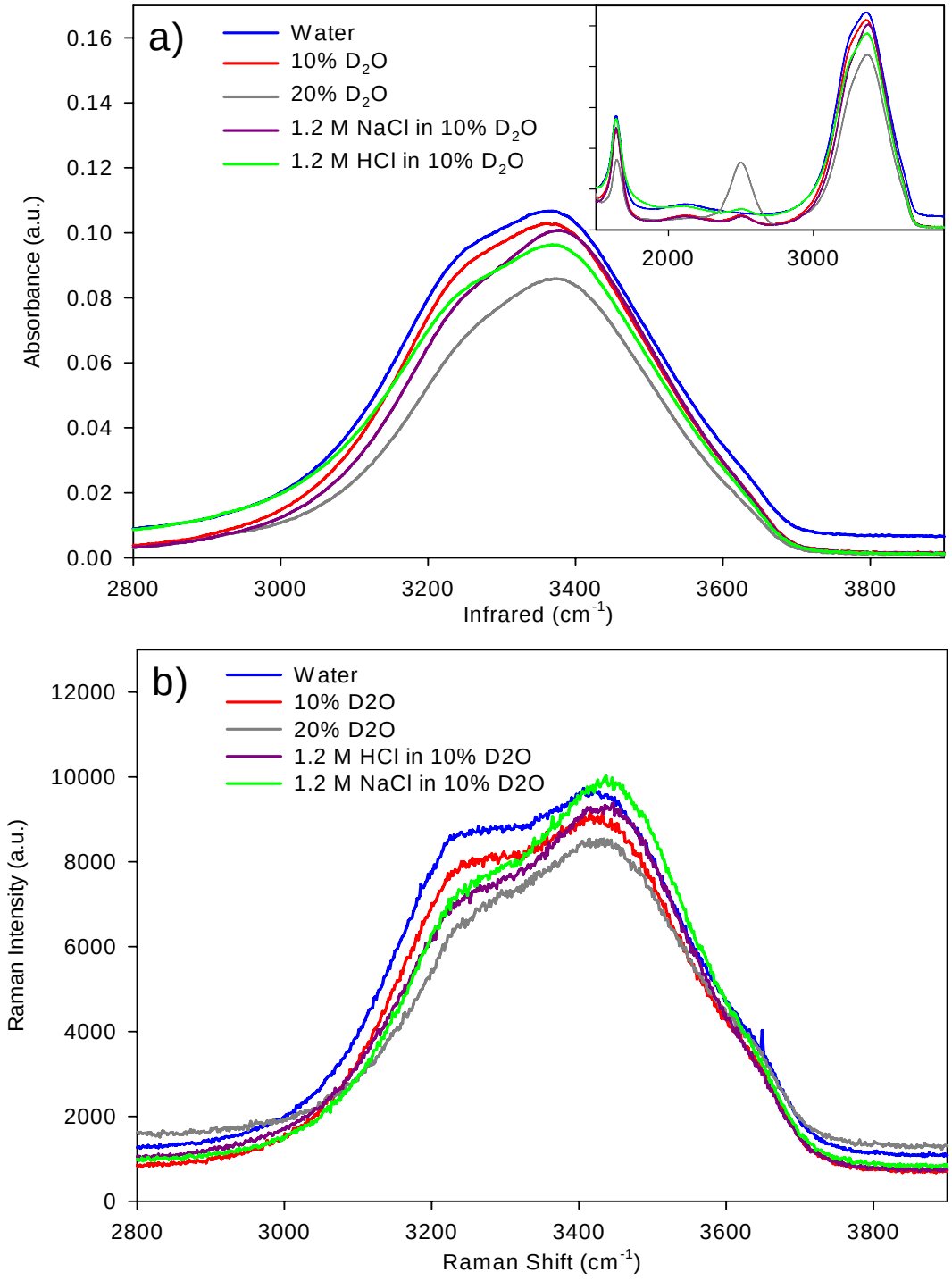

Figure 3.13: (a) ATR-FTIR spectra and (b) Isotropic Raman spectra of 10 mol % and 20 mol % D_2O and 10 mol % deuterated solutions of 1.2 M NaCl and HCl. The neat water spectrum is also included for comparison.

3.3 Conclusions

The air-liquid interface of aqueous hydrogen-halide (i.e. strong acid), sodium salt and sodium base solutions was investigated using vibrational sum frequency generation spectroscopy. The effect of these ions on the bulk water structure was also studied using ATR-FTIR and Raman spectroscopies. Within the bulk liquid environment for the aqueous sodium chloride, sodium hydroxide, and hydrochloric, hydrobromic, and hydriodic acid solutions, the hydrogen-bonding network of water becomes increasingly perturbed by the solvation shell of the anion as the size and polarizability is increased. For the NaCl and NaOH aqueous solutions, the interfacial water structure was found to be similar to that for neat water. Whereas, enhanced intensity was observed in the water O-H stretching modes at the air-liquid interface of aqueous HCl, HBr, and HI solutions. Comparison of the bulk and interfacial spectra of the acid solutions indicates the presence of H_3O^+ (and $H_5O_2^+$), bromide, and iodide ions at the air-liquid interface and an increase in interfacial depth.

CHAPTER 4

ACID CONCENTRATION STUDY

4.1 Surface Tension Measurements

To examine the macroscopic view of the interface and thus gain further insight into the air-liquid interface, surface tensions of the water and acid solutions were obtained and the results are shown in Figure 4.1. Also included in Figure 4.1 are the surface tensions of the corresponding sodium salts for comparison (the corresponding molarities of the aqueous solutions are shown in Table 4.1). Upon the addition of acid, the surface tension decreases relative to that of water. HCl and HBr have approximately the same effect on the surface tension of water, whereas the effect of HI is much greater. In contrast, the addition of salts causes the surface tension of water to increase. These results are consistent with previously reported surface tension data.[75]

Interpretation of the changes of surface tension with the addition of inorganic electrolytes is typically achieved via the Gibbs adsorption equation, which predicts the net (positive or negative) excess of ion in the interface.[76] An increase in surface tension with respect to neat water is explained by a net depletion of the surface layer by ions (both cations and anions). It is traditionally believed that inorganic aqueous salt solution surfaces are devoid of ions.[75-77] However, the studies presented here as well as molecular

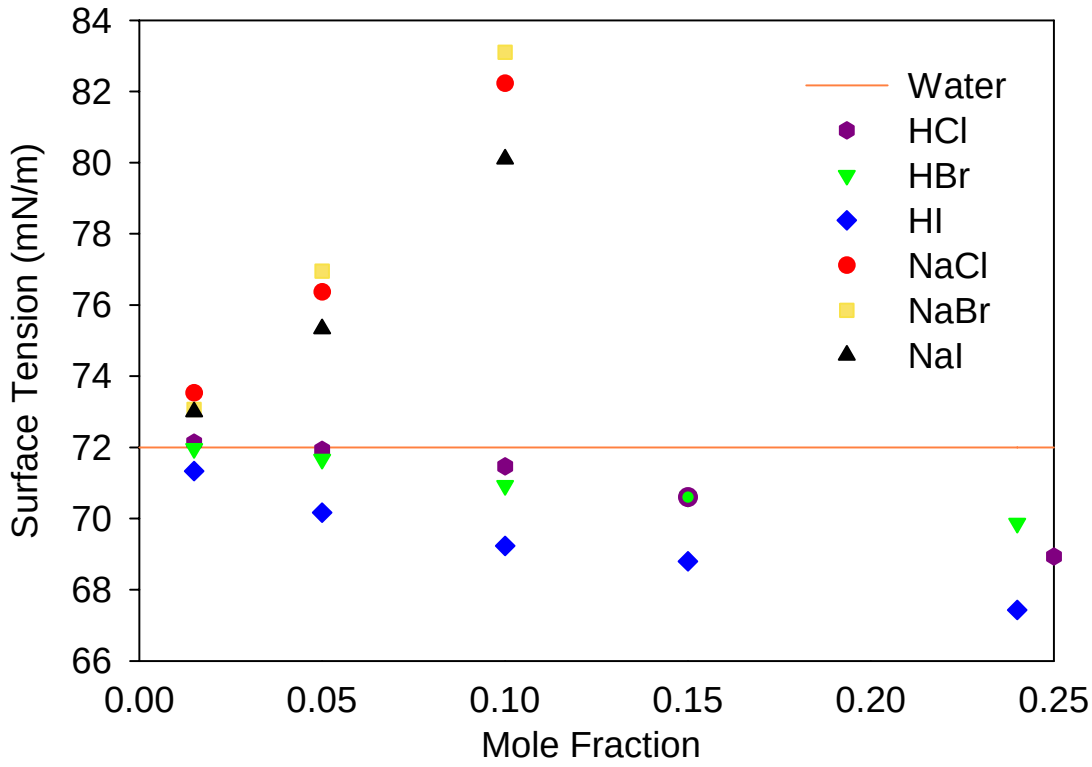

Figure 4.1: Surface tensions of acid and salt solutions.

	Mole Fraction (x)	Molarity (mol/L)
HCl	0.015	0.82
	0.022	1.2
	0.050	2.7
	0.10	5.2
	0.15	7.5
HBr	0.015	0.81
	0.023	1.2
	0.050	2.5
	0.10	4.6
	0.15	6.4
HI	0.015	0.79
	0.024	1.2
	0.050	2.3
	0.10	4.0
	0.15	5.3
NaCl	0.015	0.85
	0.021	1.2
	0.050	2.9
	0.10	6.2
NaBr	0.015	0.85
	0.021	1.2
	0.050	2.9
	0.10	6.2
NaI	0.015	0.85
	0.021	1.2
	0.050	2.9
	0.10	6.2

Table 4.1: Mole fractions and molarities of the aqueous solutions.

dynamics simulations[52,54,78] and other surface sensitive studies[29,79,80] have shown that ions are present at the air-aqueous interface. These results are not a direct contradiction of the thermodynamic arguments based on the Gibbs adsorptions equation, since these arguments do not account for a non-monotonous ion concentration profile with a surface enhancement and sub-surface depletion. In the case of sodium salts (NaCl, NaBr, and NaI), the sodium ion tends to be repelled from the surface, while the halide ions have either a weak (Cl^-) or strong (Br^- and I^-) preference for the surface.[54] The combined effect of the two ions is an integral net depletion of ions from the interfacial region.

4.2 ATR-FTIR and Raman Spectra of Acid Concentration Series

To understand the hydrogen-bonding environment of bulk water after the addition of small amounts of strong acids, a series of IR and Raman spectra were obtained for 0.015*x*, 0.050*x*, and 0.10*x* HCl, HBr, and HI aqueous solutions. The ATR-FTIR spectra of the acid series are shown in Figure 4.2, a-c. Spectral assignments were made after deconvoluting the spectra into component peaks as shown in Figure 4.3, a-j (calculated fits are shown in green). Isotropic Raman spectra (polarized parallel to the electric field vector of the incident vertically polarized laser beam) of the acid series are shown in Figure 4.4, a-c. The unpolarized, isotropic, and anisotropic (polarized perpendicular to the electric field vector of the incident vertically polarized laser beam) Raman spectra are also shown together in Figure 4.5, a-f. As in the IR spectra, spectral assignments were made after deconvolution of the spectra into component peaks as shown in Figure 4.6, a-j, with the calculated fits shown in green. The peaks in the water O-H stretching region

of the IR and Raman spectra are assigned to the modes with primarily symmetric stretch character at ~3250 cm^{-1} and the modes with antisymmetric stretch character at ~3400 cm^{-1} and ~3550 cm^{-1}, as previously described in Chapter 3.

Fitting of the ATR-FTIR and Raman spectra of the acids is complicated by the presence of the proton hydration complexes, H_3O^+ and $H_5O_2^+$.[43-45,48] These complexes have a broad absorption in the IR spectra and to a lesser extent in the Raman spectra and an additional peak had to be included when fitting the acid spectra. The peak positions, amplitudes, full width at half maximum (FWHM), and peak areas for the IR and Raman spectra are shown in Table 4.2.

Upon the addition of acid, the IR spectra (Figure 4.2) show a decrease in the 3250 and 3400 cm^{-1} peaks and a narrowing of the 3400 cm^{-1} peak. The IR spectra also reveal a substantial intensity enhancement in the region between ~1500 cm^{-1} and ~3100 cm^{-1} as acid is added. The Raman spectra (Figure 4.4) show a decrease in the 3250 cm^{-1} peak, which is accompanied by an increase and narrowing of the 3400 cm^{-1} peak. The broad band observed in the IR spectra from ~1500 and ~3100 cm^{-1} is also present in the Raman spectra, but to a lesser extent. These changes in the hydrogen-bonding region in the IR and Raman spectra are amplified when going from 0.015*x* to 0.10*x*, as well as when the size and polarizability of the anion is increased ($Cl^- < Br^- < I^-$).

The decrease in the 3250 cm^{-1} peak intensity is due to the disruption of the symmetric stretch character of the tetrahedral hydrogen-bonding network. The resulting increase in modes with anti-symmetric stretch character is observed in the increase of the 3400 cm^{-1} peak of the Raman spectra. This weakening of the hydrogen-bonding structure is caused by the solvation of the anions; as anions are added, the water molecules break

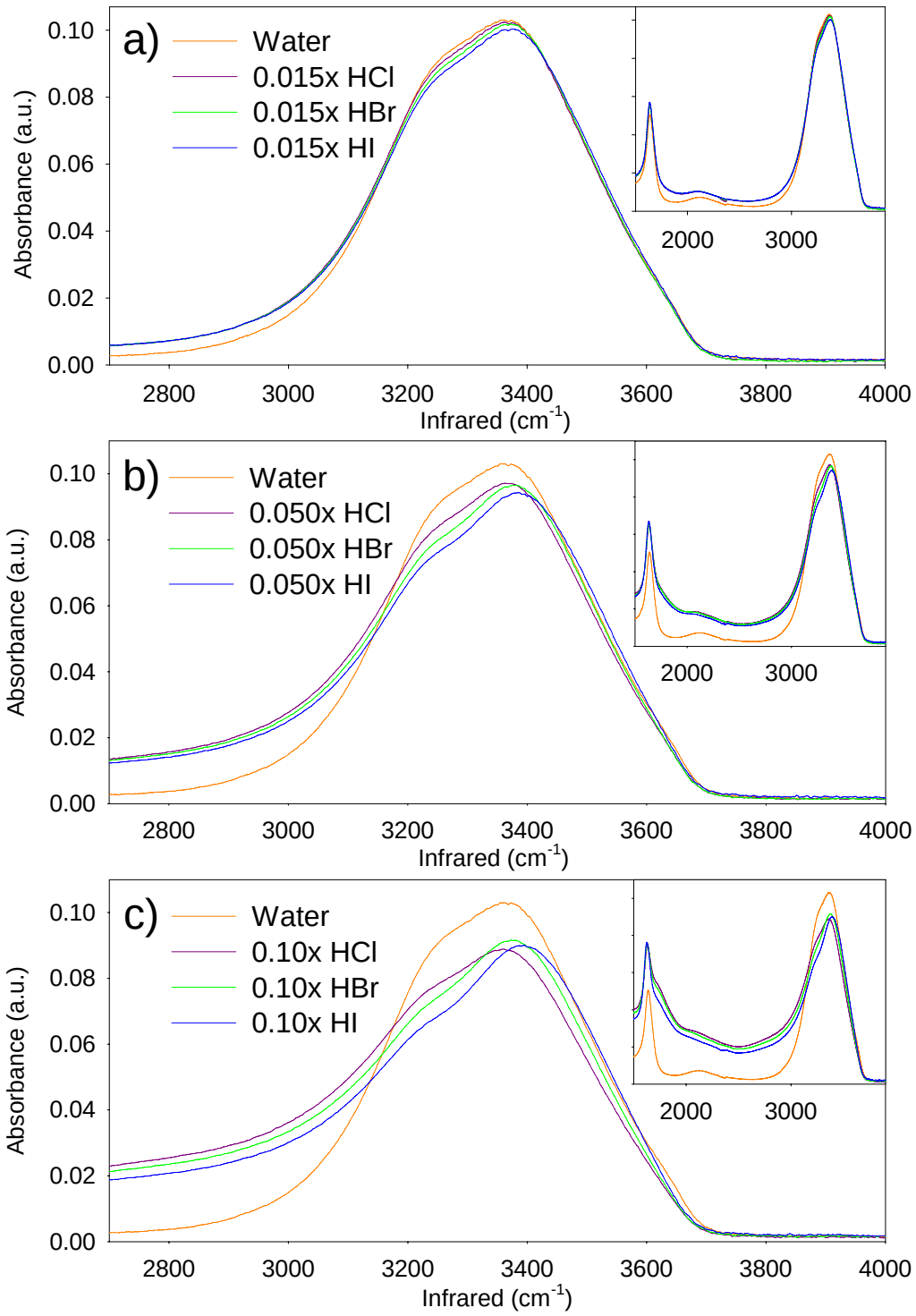

Figure 4.2: ATR-FTIR spectra of HCl, HBr, and HI aqueous solutions compared to that of neat water (a) 0.015*x* series, (b) 0.050*x* series, and (c) 0.10*x* series. Insets: ATR-FTIR spectra of the acid between 1500 cm^{-1} and 3900 cm^{-1}.

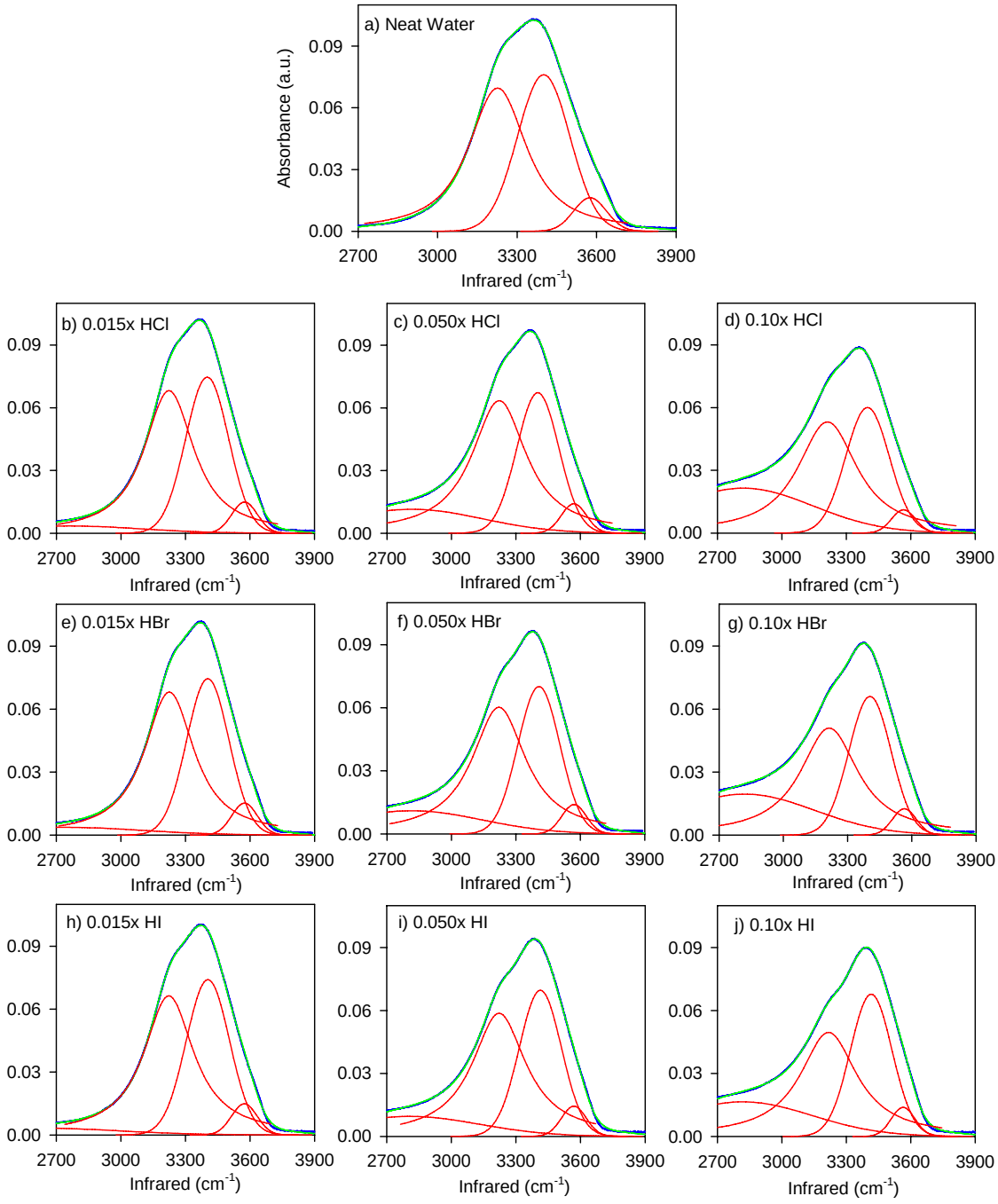

Figure 4.3: Spectral fits of ATR-FTIR spectra of the acid series (a) Neat Water, (b) 0.015*x* HCl, (c) 0.050*x* HCl, (d) 0.10*x* HCl, (e) 0.015*x* HBr, (f) 0.050*x* HBr, (g) 0.10*x* HBr, (h) 0.015*x* HI, (i) 0.050*x* HI, (j) 0.10*x* HI. Component peaks are shown in red and the calculated fits from the component peaks are shown in green.

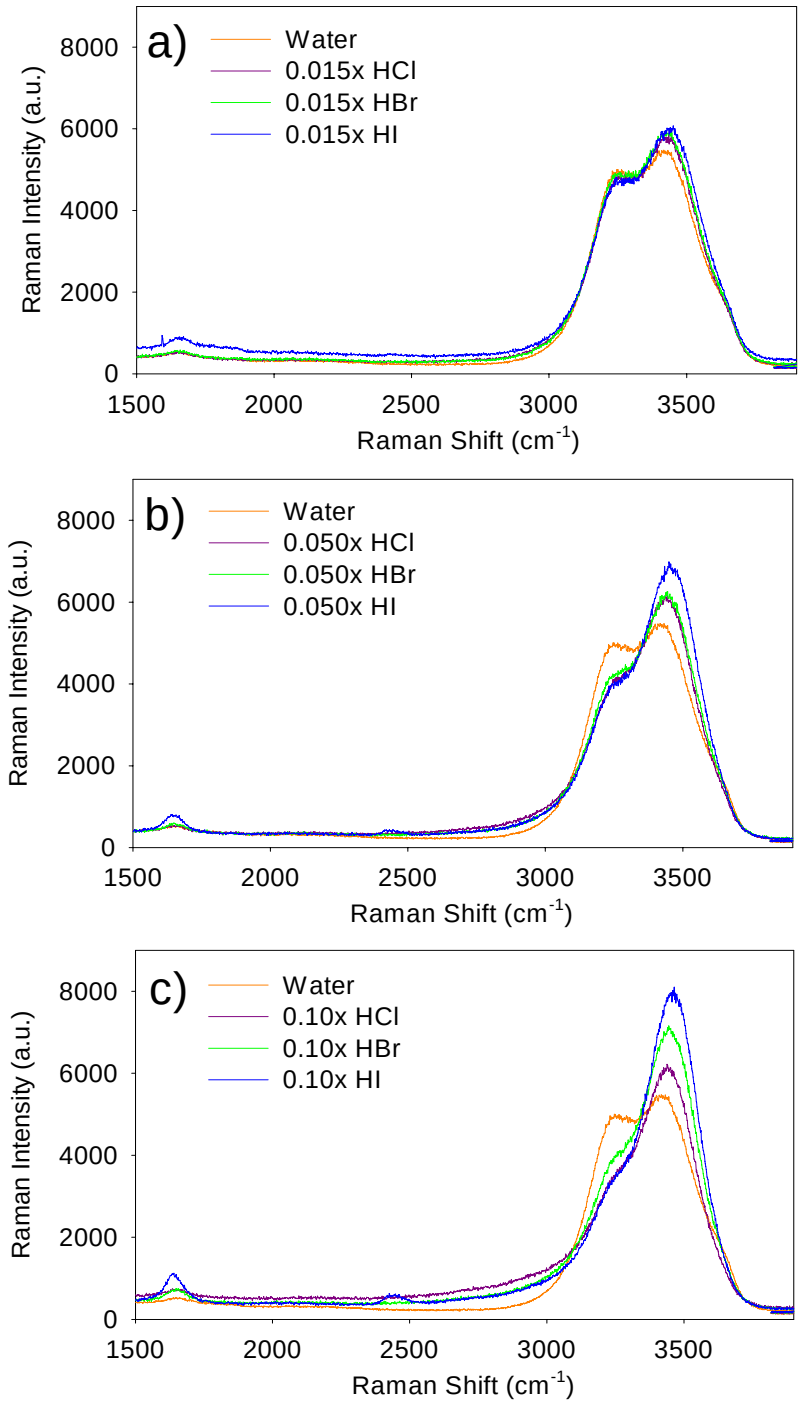

Figure 4.4: Isotropic Raman spectra of HCl, HBr, and HI aqueous solutions compared to that of neat water (a) 0.015*x* series, (b) 0.050*x* series, and (c) 0.10*x* series.

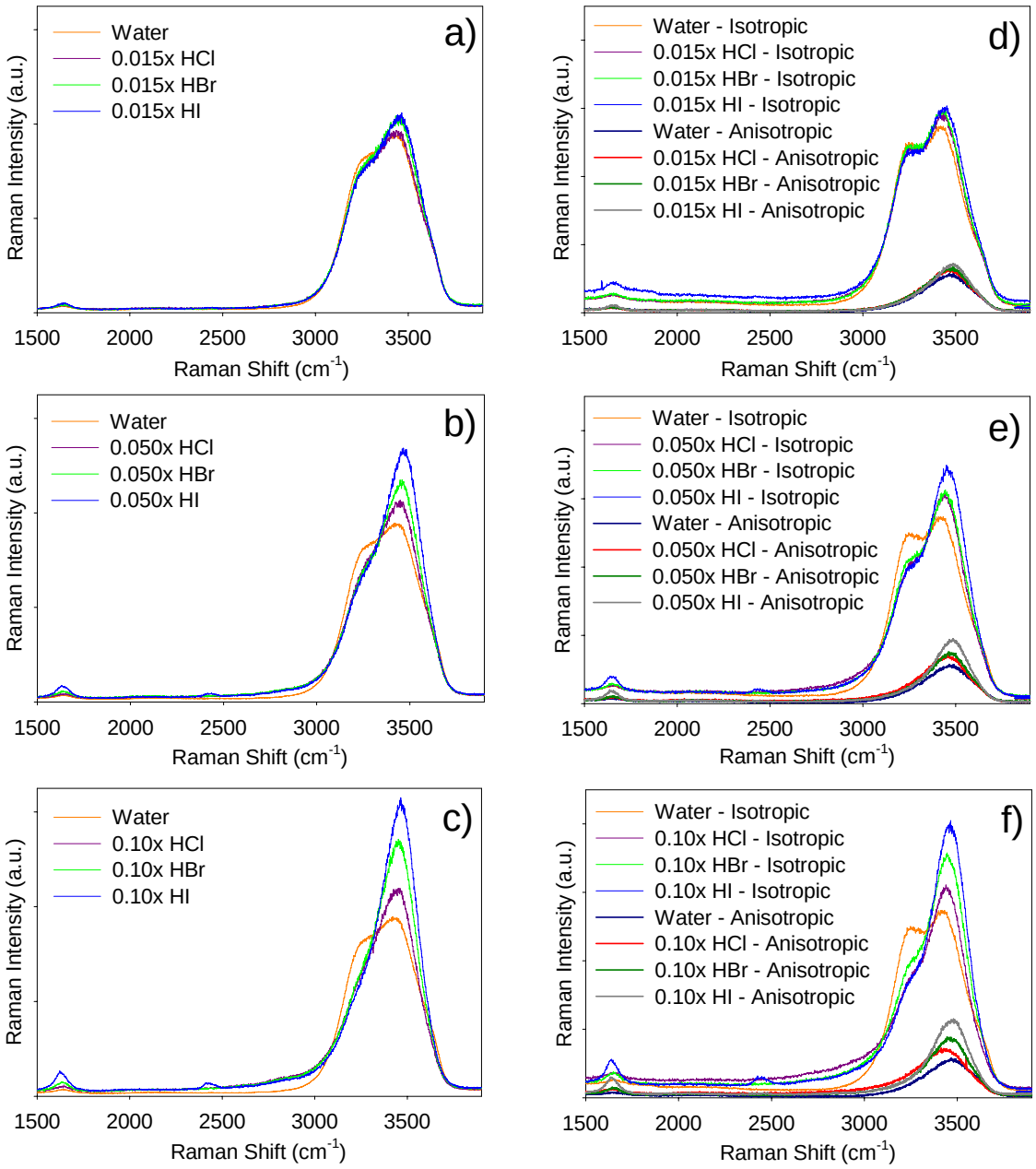

Figure 4.5: Unpolarized Raman spectra of HCl, HBr, and HI aqueous solutions compared to that of neat water (a) 0.015*x* series, (b) 0.050*x* series, and (c) 0.10*x* series. Spectra were acquired using the system with the SpectraPro monochromator. Polarized Raman spectra of HCl, HBr, and HI aqueous solutions compared to that of neat water (d) 0.015*x* series, (e) 0.050*x* series, and (f) 0.10*x* series. Spectra were acquired using the system with the Shamrock monochromator.

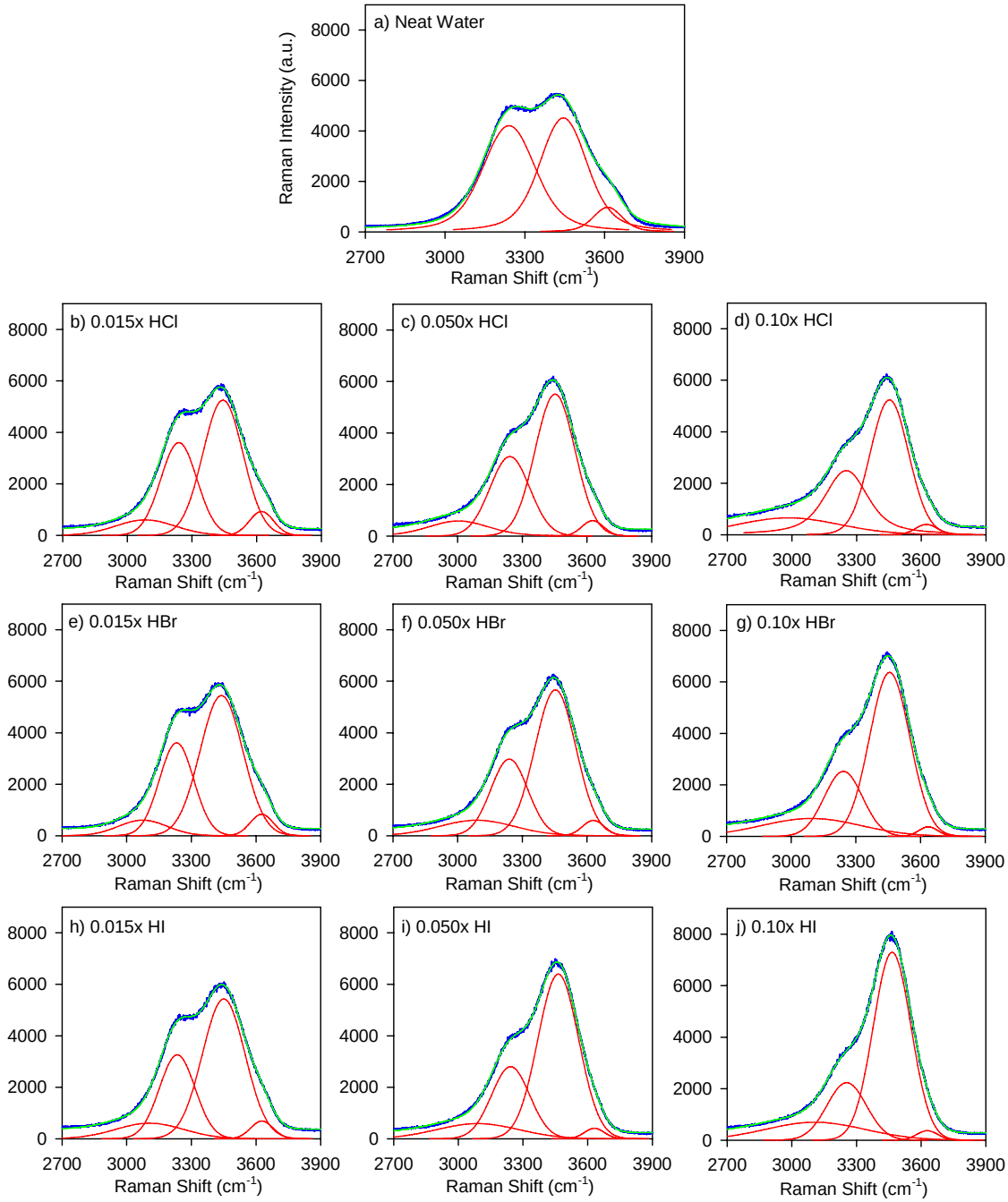

Figure 4.6: Spectral fits of isotropic Raman spectra of the HCl acid series (a) Neat Water, (b) 0.015*x* HCl, (c) 0.050*x* HCl, (d) 0.10*x* HCl, (e) 0.015*x* HBr, (f) 0.050*x* HBr, (g) 0.10*x* HBr, (h) 0.015*x* HI, (i) 0.050*x* HI, (j) 0.10*x* HI. Component peaks are shown in red and the calculated fits from the component peaks are shown in green.

	ATR-FTIR				Raman			
	Peak Position (cm^{-1})	Amplitude (A_v)	FWHM	Area	Peak Position (cm^{-1})	Amplitude (A_v)	FWHM	Area
Neat Water	3226.3	0.0923	259.1	27.35	3240.8	4478.8	231.6	1.22×10^6
	3400.5	0.0761	233.1	18.88	3445.1	4807.3	208.3	1.18×10^6
	3575.5	0.0163	145.6	2.52	3611.7	1037.0	127.3	1.55×10^5
0.015*x* HCl	2755.4	0.0035	791.2	2.92	3083.4	600.5	324.1	2.07×10^5
	3223.5	0.0958	277.4	29.16	3238.9	3603.4	197.8	7.59×10^5
	3401.2	0.0747	235.8	18.74	3443.6	5253.3	219.2	1.23×10^6
	3575.2	0.0149	140.2	2.22	3622.5	927.4	132.4	1.30×10^5
0.015*x* HBr	2733.6	0.0037	865.9	3.42	3074.8	605.1	265.8	1.71×10^5
	3225.0	0.0960	277.0	29.12	3231.6	3609.3	187.1	7.19×10^5
	3404.0	0.0745	232.3	18.43	3439.7	5448.1	233.5	1.35×10^6
	3574.5	0.0152	140.1	2.27	3626.5	837.2	125.8	1.12×10^5
0.015*x* HI	2609.7	0.0033	890.5	3.12	3106.3	605.3	370.0	2.38×10^5
	3223.2	0.1018	280.3	29.05	3234.6	3261.9	194.2	6.74×10^5
	3404.9	0.0741	237.1	18.70	3450.2	5431.9	233.0	1.35×10^6
	3574.0	0.0148	140.3	2.21	3627.4	691.7	122.2	8.99×10^5
0.050*x* HCl	2816.4	0.0114	770.1	9.38	3004.05	601.7	326.9	2.23×10^5
	3222.3	0.0955	305.9	30.27	3242.1	3086.8	216.9	7.13×10^5
	3402.4	0.0672	230.4	16.49	3451.9	5513.2	217.6	1.28×10^6
	3570.2	0.0141	137.7	2.07	3626.3	597.5	117.6	7.50×10^5

Continued

Table 4.2: Parameters for ATR-FTIR (Figures 3.11, a-j) and isotropic Raman (Figures 3.13, a-j) spectral fits of HCl, HBr, and HI concentration series.

Table 4.2 (continued)

	ATR-FTIR				Raman			
	Peak Position (cm^{-1})	Amplitude (A_v)	FWHM	Area	Peak Position (cm^{-1})	Amplitude (A_v)	FWHM	Area
0.050*x* HBr	2814.6	0.0110	774.0	9.09	3089.0	601.0	409.9	2.62×10^5
	3221.0	0.0952	302.9	28.58	3239.5	2975.7	201.5	6.38×10^5
	3407.3	0.0701	230.0	17.16	3453.6	5664.9	223.6	1.35×10^6
	3571.0	0.0140	134.7	2.00	3629.7	597.0	119.1	7.57×10^5
0.050*x* HI	2805.8	0.0095	768.9	7.78	3090.4	589.4	447.4	2.81×10^5
	3222.1	0.1032	302.5	27.90	3242.6	2800.3	208.2	6.21×10^5
	3413.8	0.0697	230.8	17.11	3463.9	6399.7	222.3	1.51×10^6
	3569.2	0.0144	135.8	2.08	3631.4	406.6	109.2	4.74×10^5
0.10*x* HCl	2820.6	0.0215	764.2	17.47	2938.6	658.3	560.6	4.02×10^5
	3212.6	0.0749	328.8	27.0	3251.9	2797.1	233.4	7.84×10^5
	3398.9	0.0601	240.2	15.36	3452.3	5259.1	210.0	1.19×10^6
	3566.5	0.0111	131.8	1.56	3624.0	400.4	119.3	5.01×10^5
0.10*x* HBr	2819.7	0.0195	767.0	15.93	3093.3	696.0	541.2	4.01×10^5
	3214.5	0.0755	325.0	25.77	3242.2	2525.2	208.4	5.60×10^5
	3404.9	0.0661	232.6	16.35	3456.9	6369.6	219.5	1.49×10^6
	3565.5	0.0125	131.1	1.75	3636.3	370.0	104.6	4.12×10^5
0.10*x* HI	2817.5	0.0165	761.5	13.36	3108.2	696.5	542.7	4.02×10^5
	3217.4	0.0781	319.8	24.82	3254.5	2235.7	214.9	5.11×10^5
	3416.0	0.0678	228.3	16.47	3465.4	7296.4	206.3	1.60×10^6
	3564.6	0.0139	130.5	1.92	3628.5	370.7	115.1	4.54×10^5

their tetrahedral hydrogen-bonding environment to separately solvate the anion, resulting in a more disordered hydrogen-bonded network as previously discussed in Chapter 3. As the acid concentration is increased, an ever-increasing fraction of the water molecules becomes associated with the hydration shells of the anions. The resulting effect is an increasing perturbation of the hydrogen-bonding network and thus an increase in the 3400 cm^{-1} peak.

The differences in the hydrogen-bonding region of the IR and Raman spectra can again be attributed to the different selection rules; for a mode to be IR active, the vibration must cause a change in dipole moment and for a mode to be Raman active, there must be a change in polarizability with the vibration. As acids with increasingly polarizable anions ($Cl^- < Br^- < I^-$) are added, the water molecules solvating these anions exhibit increased polarizability; thus, since Raman intensities arise from this condition, the effect is observed in the Raman spectra. Additionally, the amplitudes in the IR spectra are not the actual absorption cross sections, but the product of these with the coupling of the respective intramolecular motions to intermolecular excitation along the hydrogen bonds.[33] The polarity of the H_3O^+ and $H_5O_2^+$ ions also responsible for the strong proton continuum in the IR spectra, but weak Raman spectra.[47]

The broad band, between ~1500 cm^{-1} and ~3100 cm^{-1}, present in both the IR and Raman spectra arises from $H_5O_2^+$ groupings, as mentioned in Chapter 3. These hydrogen bonds are extremely polarizable and interact strongly with their environment. These strong interactions (i.e. induced dipole interactions with ions and with dipole fields of the solute and solvent molecules and with each other) distort the energy surfaces of the hydrogen-bonds in $H_5O_2^+$.[43,44,49-51] The distortion of the energy surfaces results in the

photons in the hydrogen bonds having a continuous energy level distribution and thus, a continuum in the IR and Raman spectra is observed,[43,44,51] as stated in Chapter 3.

In addition to the changes observed in the water O-H stretching region in the IR and Raman spectra, a peak at ~1730 cm^{-1} begins to emerge at low concentrations in the IR spectra (inset of Figure 4.2) and becomes increasingly visible with higher concentrations. This peak has been assigned to the ν_4 vibrational mode of H_3O^+.[45,58,81]

4.3 VSFG Spectra of Acid Concentration Series

To examine effect of acids on the air-water interface, SSP-polarized VSFG spectra were acquired of 0.015*x*, 0.050*x*, and 0.10*x* aqueous solutions of HCl and HBr. Figure 4.7 shows the effects of the two anions (Cl^- and Br^-) on the air-water interface and Figure 4.8 shows the trend as the acid concentration is increased. Spectral fits of the VSFG spectra after deconvolution into the component peaks with the calculated fits (green solid lines going through the majority of the data points) are shown in Figure 4.9, a-g. The corresponding fitting parameters including relative phases (+ versus -) of the amplitude terms are shown in Table 4.3.

Acquiring reproducible VSFG spectra of the aqueous acid solutions proved to be a difficult task. The trend in the HCl and HBr concentration series was able to be reproduced over a period of two years. Most recently the VSFG spectra of the HCl concentration series acquired in 2004 were reproduced in March 2005 and are shown in Figure 4.8b. However, reproducing the trend in the HI concentration series was more difficult and therefore the VSFG spectra of the HI concentrations are not presented here. The source of the irreproducibility in the VSFG spectra of aqueous acid solutions is

uncertain. Energy tests were performed to address this issue (Appendix A) and the source of the irreproducible acid VSFG spectra was not able to be determined from these tests. Consequently, further work needs to be done on these solutions.

As stated in Chapter 3, the peak assignments for the aqueous acid solutions are the same as that for neat water (Figure 3.2) except for the addition of a broad band centered at ~3100 cm^{-1} to account for the vibrational stretches of H_3O^+ and $H_5O_2^+$. The region between 2800 cm^{-1} and 3950 cm^{-1} of the VSFG spectra of aqueous solutions is comprised of the single proton donor – double proton acceptor (DAA) molecule stretch at ~3250 cm^{-1},[33-35] tetra-coordinated interfacial water molecule stretch at ~3400 cm^{-1},[33-35] the double proton donor – single proton acceptor (DDA) molecule stretch at ~3550 cm^{-1},[33-35] and the dangling O-H stretch at ~3700 cm^{-1}.[36-38]

The VSFG spectra of the acids reveal two distinct trends, one in the identity of the anion (as previously observed in Chapter 3) and one in concentration. Firstly, as the identity of the anion is changed from chloride to bromide, the VSFG spectra (Figure 4.7) reveal an enhancement in the 3250 cm^{-1} and 3400 cm^{-1} peak intensities. The increase in the 3400 cm^{-1} peak intensity (arising from tetra-coordinated water molecules) is attributed to water molecules solvating the anions at the surface and thus disrupting the hydrogen-bonding network, as previously described in the bulk solution studies and in the 1.2 M aqueous solutions (Chapter 3).

Changing the concentration of the acids results in a slightly more complicated scenario (Figure 4.8). The addition of 0.015*x* increases the intensity of the 3250 cm^{-1} peak and decreases the 3700 cm^{-1} (free O-H) peak. Increasing the concentration to 0.050*x* continues to increase the 3250 cm^{-1} peak and decrease the 3700 cm^{-1} peak. However,

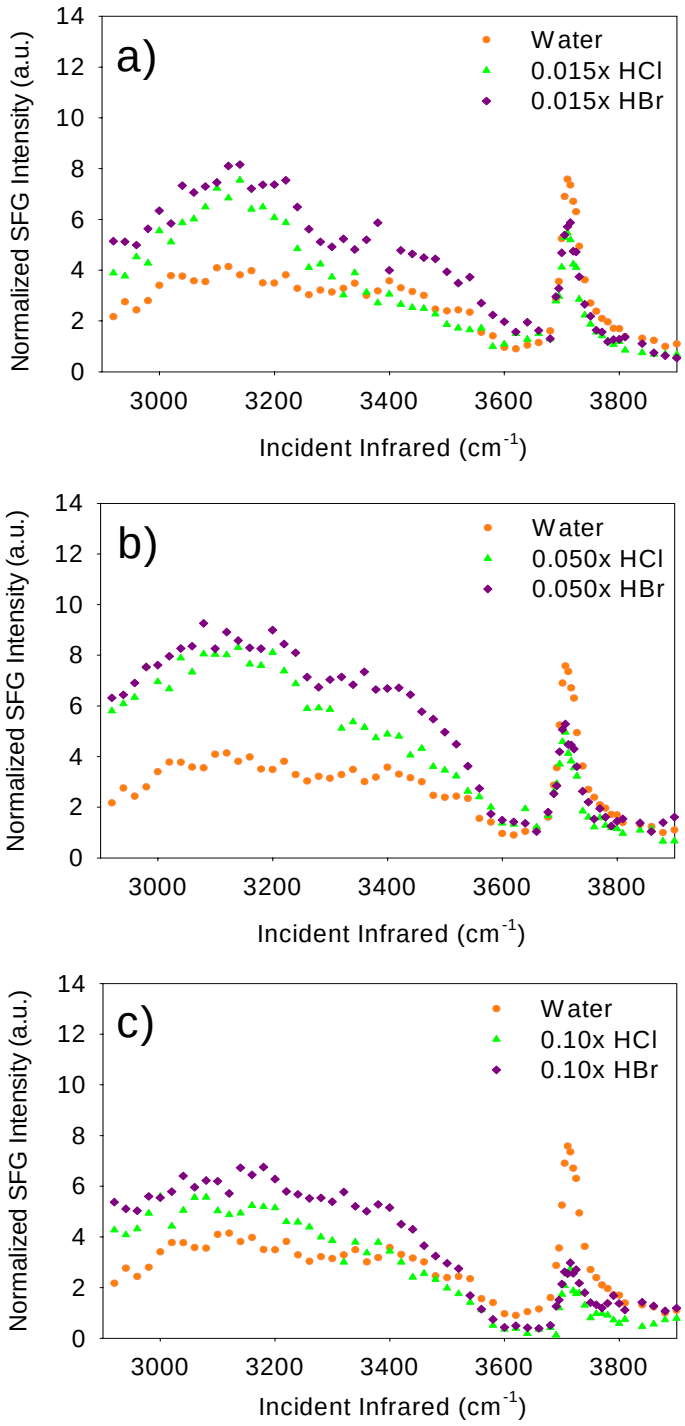

Figure 4.7: SSP-polarized VSFG spectra of acid solutions compared to that of neat water (a) 0.015*x*, (b) 0.050*x*, (c) 0.10*x*.

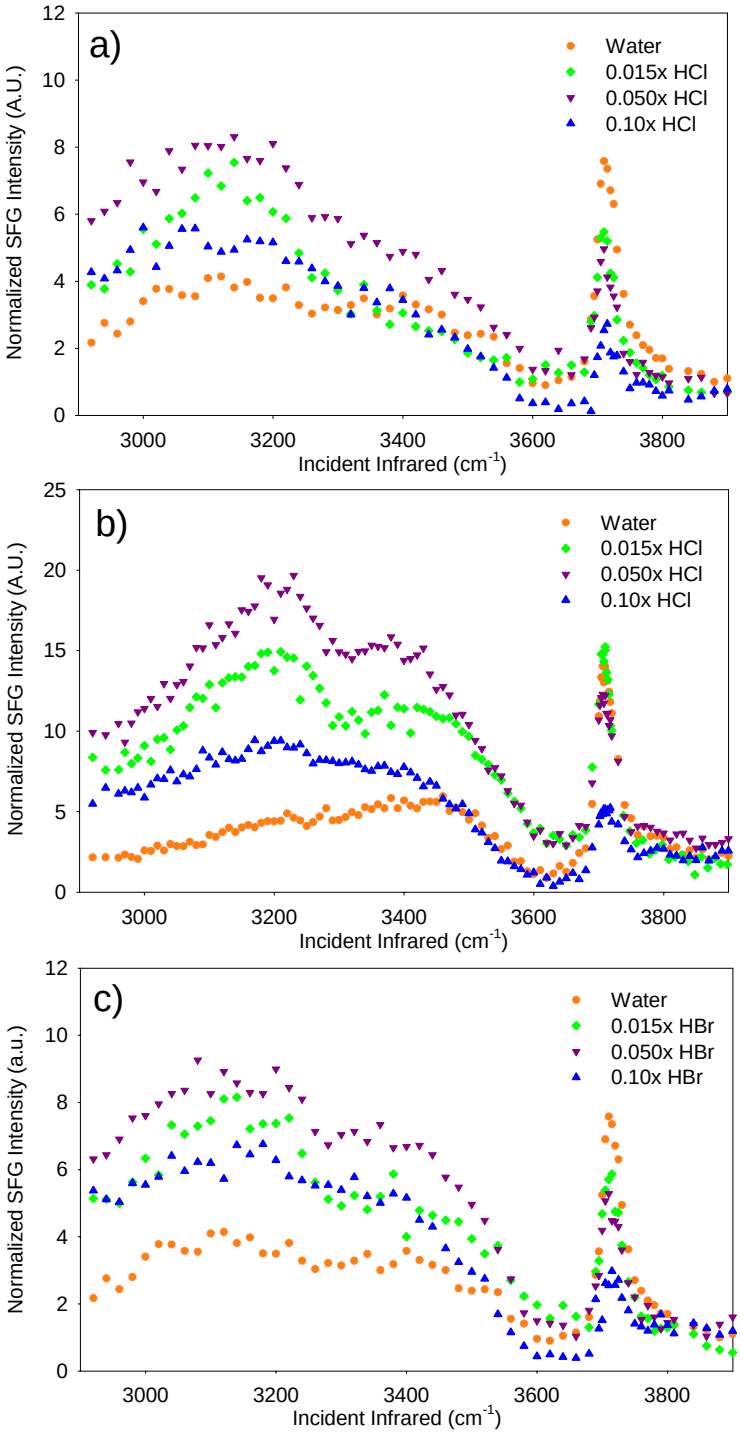

Figure 4.8: SSP-polarized VSFG spectra of acid solutions compared to that of neat water (a) HCl concentration series, (b) HCl concentration series reproduced March 2005, (c) HBr concentration series.

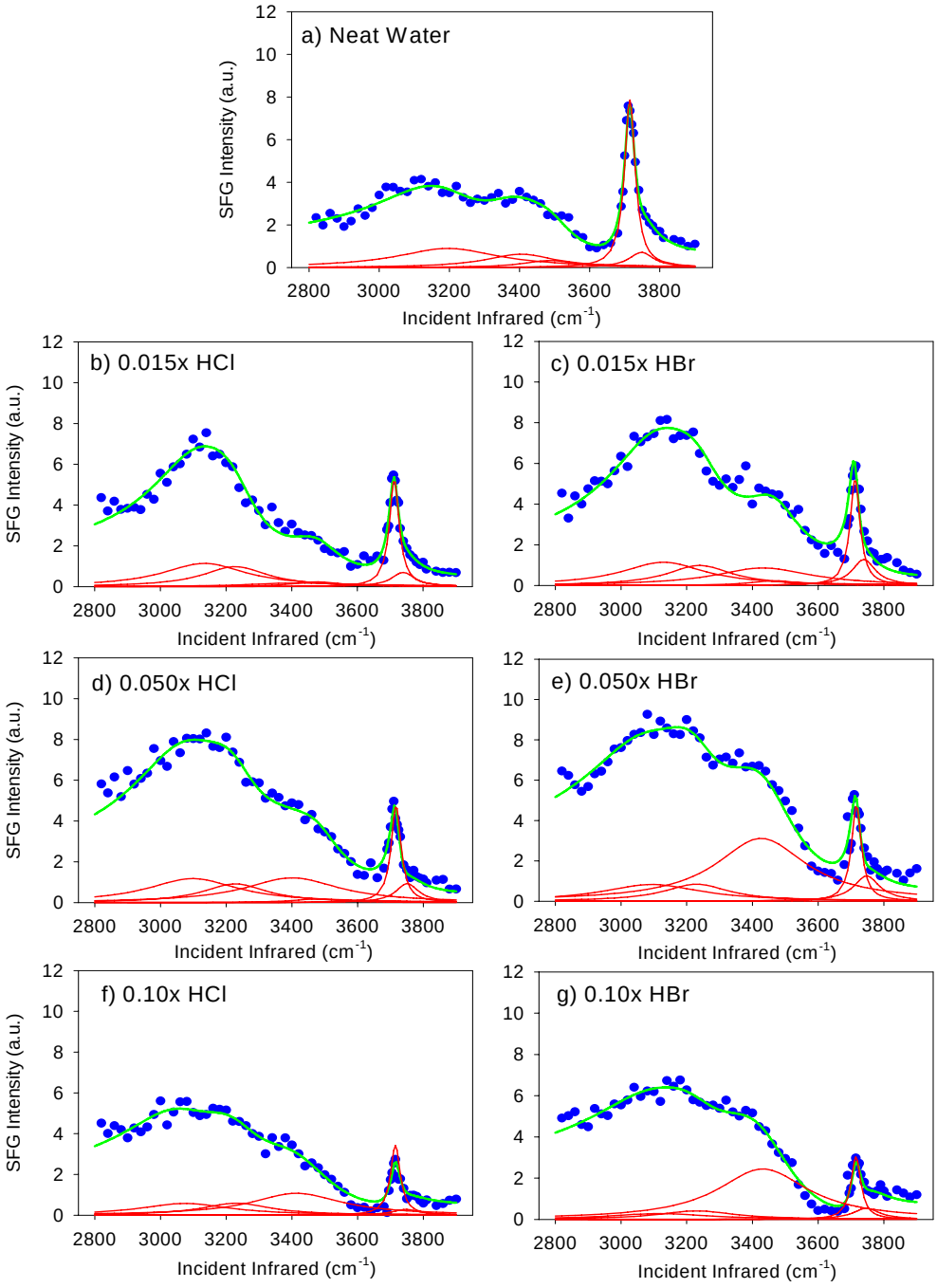

Figure 4.9: Spectral fits of SSP-polarized VSFG spectra of the HCl acid series (a) Neat Water, (b) 0.015*x* HCl, (c) 0.050*x* HCl, (d) 0.10*x* HCl, (e) 0.015*x* HBr, (f) 0.050*x* HBr, (g) 0.10*x* HBr. Component peaks are shown in red and the calculated fits from the component peaks are shown as green lines that go through most of the data points.

	Non-Resonant Term	Peak Position (cm^{-1})	Phase	Amplitude (A_v)	Γ_v	FWHM	Area
Neat Water	-0.88576 + 0.28837*i*	3196.2	+	167.0	176.3	352.6	391.8
		3403.2	+	95.1	120.2	240.4	203.5
		3487.1	+	51.3	89.2	178.4	82.7
		3714.5	-	51.3	18.3	36.6	439.3
		3747.5	-	36.0	42.6	85.2	86.1
0.015x HCl	-0.88576 + 0.28837*i*	3134.1	+	167.0	156.3	312.6	446.5
		3227.5	+	119.4	120.2	240.4	319.1
		3419.8	+	75.1	176.2	352.4	80.5
		3476.1	+	43.8	89.2	178.4	60.2
		3712.3	-	41.8	18.3	36.6	292.1
		3739.3	-	35.7	42.6	85.2	85.1
0.050x HCl	-0.88576 + 0.28837*i*	3098.2	+	182.4	167.8	335.6	480.5
		3227.5	+	115.4	120.2	240.4	298.0
		3400.8	+	194.2	176.2	352.4	538.7
		3476.1	+	37.8	89.2	178.4	44.8
		3716.9	-	39.8	18.3	36.6	264.4
		3751.0	-	41.2	42.6	85.2	112.5
0.10x HCl	-0.98772 + 0.25035*i*	3075.4	+	126.8	167.3	334.6	230.1
		3231.8	+	97.9	128.0	256.0	199.5
		3414.7	+	173.7	167.8	335.6	456.9
		3453.1	+	8.51	110.2	220.4	1.79
		3714.9	-	33.8	18.3	36.6	190.8
		3746.9	-	26.1	49.1	98.2	38.7

Continued

Table 4.3: Parameters for VSFG spectral fits of 0.015*x*, 0.050*x*, and 0.10*x* aqueous solutions of HCl and HBr.

Table 4.3 (continued)

	Non-Resonant Term	Peak Position (cm^{-1})	Phase	Amplitude (A_v)	Γ_v	FWHM	Area
0.015x HBr	-0.88576 + 0.28837*i*	3129.1	+	167.0	156.3	312.6	445.6
		3239.8	+	119.4	120.2	240.4	319.5
		3433.2	+	166.4	179.4	358.8	385.4
		3467.4	+	43.2	89.2	178.4	58.6
		3712.3	-	41.8	18.3	36.6	292.1
		3739.2	-	48.2	42.6	85.2	155.5
0.050x HBr	-1.1808 + 0.19207*i*	3094.7	+	166.3	182.8	365.6	357.5
		3230.3	+	110.4	120.2	240.4	272.9
		3426.6	+	295.2	167.2	334.4	1323.6
		3453.3	+	11.8	89.2	178.4	4.35
		3716.5	-	39.8	18.3	36.6	264.4
		3747.8	-	53.3	47.6	95.2	167.0
0.10x HBr	-1.2669 + 0.073293	3116.7	+	98.7	186.3	372.6	124.3
		3230.3	+	89.9	140.0	280.0	151.3
		3431.5	+	262.7	167.8	335.6	1043.3
		3453.1	+	8.51	110.2	220.4	1.79
		3714.9	-	31.8	18.3	36.6	168.9
		3746.9	-	36.1	49.1	98.2	74.1

when the concentration is increased to 0.10*x*, the peak intensity in the hydrogen-bonding region decreases to an intensity just below that of 0.015*x*, but is still increased relative to neat water. The 3700 cm^{-1} peak in 0.10*x* acid solutions continues to decrease.

As mentioned previously in Chapter 3, one source of the additional 3250 cm^{-1} peak intensity in the VSFG spectra of the acids is an increase in the interfacial depth. Recall that vibrational sum frequency generation intensity (SSP polarization) is enhanced when probing a deeper interfacial region. The presence of H_3O^+ (and $H_5O_2^+$) ions and the halide anions at the surface of aqueous solutions causes an increase in noncentrosymmetry and thus, an increase in interfacial depth.

The interfacial depth increase can be confirmed by plotting the additive peak areas (integrated from 2800 to 3600 cm^{-1} to include the distribution of the tails) of the 3100, 3250, 3400, and 3550 cm^{-1} component peaks (Figure 4.10). The VSFG additive intensity increases from that of neat water to that of HBr for each concentration. Since the VSFG intensity is related to the Raman and IR intensities (Equation 5), comparing the product of the Raman and IR intensities with the VSFG intensity can yield information about the air-aqueous interface. The increase for the VSFG intensity for the 0.015*x* and 0.050*x* aqueous acid solutions is considerably larger than that for the Raman x IR (Figure 4.10), indicating the number of water molecules existing in the interfacial region increases with 1) the addition of H_3O^+ and $H_5O_2^+$ and 2) the size and polarizability of the halide anion. Specifically, the interface becomes larger with the addition of the H_3O^+ (and $H_5O_2^+$) and bromide anions at these concentrations. This explanation is consistent with molecular dynamics simulations which also reveal an increase in the interfacial depth upon addition of hydrogen halides (HCl, HBr, and HI) to water[52] and the observed

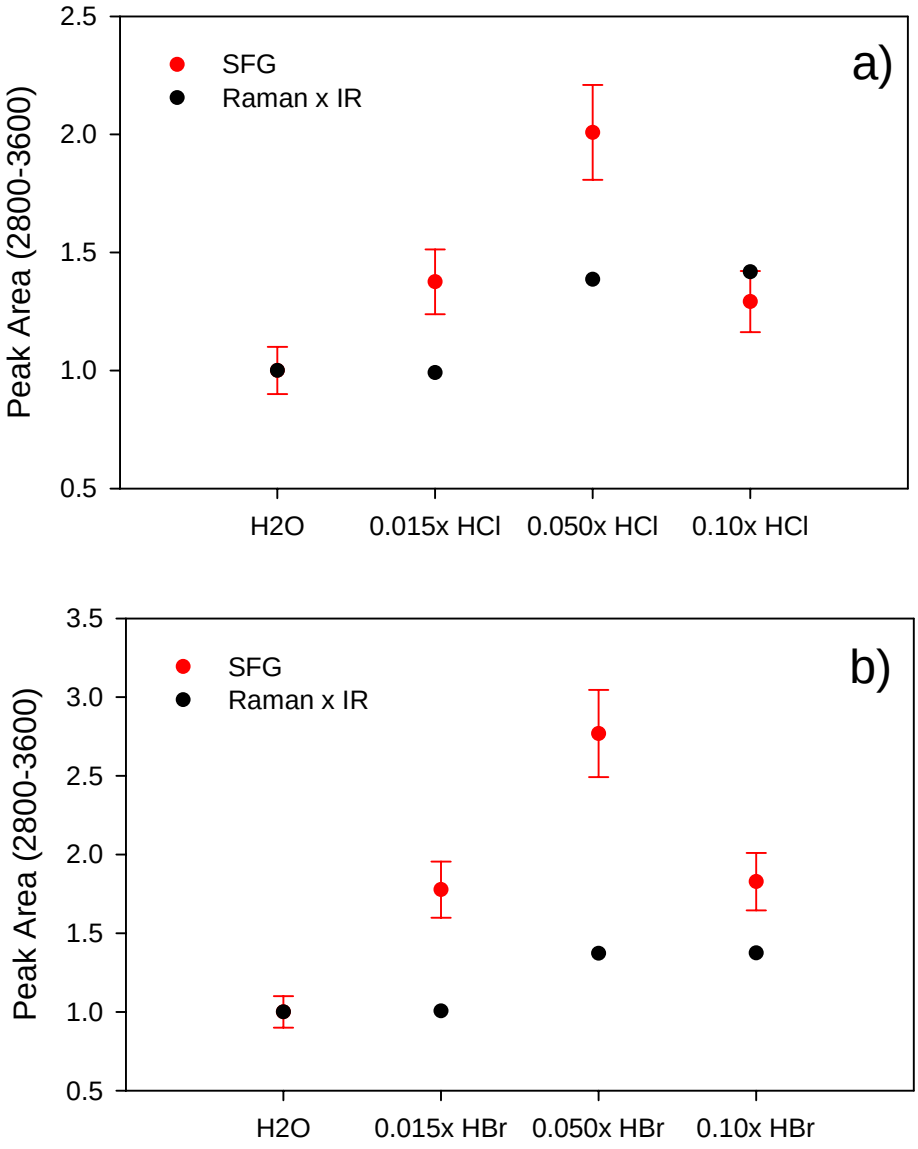

Figure 4.10: The areas of the 3100, 3250, 3400, and 3550 cm^{-1} (approximate, positions varied) peaks in the O-H stretch region for Raman x infrared (Raman area multiplied by ATR-FTIR area) and the SFG for the (a) HCl and (b) HBr acid concentrations. Areas were normalized to neat water. Error bars are estimated to be approximately 10%, based on experimental values.

increase in interfacial depth in sodium halide aqueous solutions both by experimental studies[29] and MD simulations.[53,54] However, at 0.10*x*, the interfacial depth does not continue to increase as expected. Instead, the depth decreases from that determined for the 0.050*x* solutions (but is still greater than that for neat water), indicating that the change in the depth of the interface is not linear with concentration.

Another explanation for the 3250 cm^{-1} peak intensity increase is due the vibrational modes of H_3O^+ and $H_5O_2^+$. Recent molecular dynamics simulations,[52,55] show that the hydronium ion has a weak affinity for the surface of aqueous acid solutions with a preferred orientation with the hydrogens pointing towards the aqueous phase and oxygen towards the vapor phase. Consequently, the O-H stretching frequencies of the hydronium ion are detected and contribute to the VSFG intensity. As the acid concentration is increased, more H_3O^+ (and $H_5O_2^+$) molecules are present in the interface and thus the intensity of the VSFG spectrum in the 3200 cm^{-1} region increases.

The VSFG spectra also reveal a decrease in the 3700 cm^{-1} peak intensity of the acid solutions (Figures 4.7 and 4.8), relative to neat water. Since this peak is attributed to the free O-H stretch at the air-aqueous interface, upon the addition of acids, the surface water structure undergoes a structural reorganization that reduces the number of O-H bonds projecting into the air. The identity of the anion does not affect the intensity of the free O-H peak. However, as the acid concentration is increased from 0.015*x* to 0.050*x* to 0.10*x*, the free O-H peak intensity continues to decrease. Currently, there is no clear physical understanding of the restructuring of the surface water molecules as mentioned previously in Chapter 3, but it is evident that the increasing presence of H_3O^+ (and

$H_5O_2^+$) ions in the interface plays a role. Recent molecular dynamics simulations[52] have predicted a decrease in the surface density (number per unit area) of free O-H bonds.

3.3 Conclusions

The air-liquid interface of aqueous hydrogen-halide (i.e. strong acid) solutions was investigated using vibrational sum frequency generation spectroscopy. The effect of these ions on the bulk water structure was also studied using ATR-FTIR and Raman spectroscopies. Within the bulk liquid environment for the aqueous hydrochloric, hydrobromic, and hydriodic acid solutions, the hydrogen-bonding network of water becomes increasingly disrupted by the solvation shell of the anion as the size, polarizability, and concentration of the anions is increased. Enhanced intensity was observed in the water O-H stretching modes at the air-liquid interface of 0.015*x* hydrochloric and hydrobromic acid solutions; the intensity was further enhanced as the acid concentration was increased to 0.050*x*. Whereas, at 0.10*x*, the intensity decreases relative to that for 0.050*x* but is still greater than that for neat water. Comparison of the bulk and interfacial spectra of the hydrochloric and hydrobromic acid solutions indicates the presence of H_3O^+ (and $H_5O_2^+$) and bromide ions at the air-liquid interface and an increase in interfacial depth relative to neat water. Increasing the acid concentration from 0.015*x* to 0.050*x* continues to increase the interfacial depth. However, at a concentration of 0.10*x*, the interfacial depth decreases from that for 0.050*x*, but the depth is still greater than that for the air-neat water interface, indicating the increase in interfacial depth is not linear with acid concentration.

CHAPTER 5

SUMMARY OF CONCLUSIONS

The air-liquid interface of aqueous hydrogen-halide (i.e. strong acid), sodium salt, and sodium base solutions was investigated using vibrational sum frequency generation spectroscopy. The effect of these ions on the bulk water structure was also studied using ATR-FTIR and Raman spectroscopies. Within the bulk liquid environment for the aqueous sodium chloride, sodium hydroxide, and hydrochloric, hydrobromic, and hydriodic acid solutions, the hydrogen-bonding network of water becomes increasingly perturbed by the solvation shell of the anion as the size, polarizability, and concentration is increased. For the aqueous solutions of NaCl and NaOH, the interfacial water structure was found to be similar to that for neat water. Whereas, enhanced intensity was observed in the water O-H stretching modes at the air-liquid interface of aqueous HCl, HBr, and HI solutions. Comparison of the bulk and interfacial spectra of the hydrochloric, hydrobromic, and hydriodic acids indicates the presence of H_3O^+ (and $H_5O_2^+$), bromide and iodide ions at the air-liquid interface and an increase in interfacial depth relative to neat water. Examining the effect of acid concentration on the interfacial depth reveals that the interfacial depth increases from 0.015*x* to 0.050*x*, but decreases from 0.050*x* to 0.10*x*, indicating the increase in interfacial depth is not linear with acid concentration.

The presences of H_3O^+ (and $H_5O_2^+$), bromide, and iodide ions at the air-liquid interface will have a significant effect on atmospheric aerosol chemistry. The existence of these ions at the aerosol surface will impact the physical characteristics of the aerosol surfaces (i.e. hydrophobicity, particle growth, morphology, and acidity) and thus influence the adsorption and absorption of gas phase molecules. Consequently, atmospheric heterogeneous reaction mechanisms will be altered.

REFERENCES

(1) Finlayson-Pitts, B. J. *Chemical Reviews* **2003**, *103*, 4801-4822.

(2) De Haan, D. O.; Brauers, T.; Oum, K.; Stutz, J.; Nordmeyer, T.; Finlayson-Pitts, B. J. *International Reviews in Physical Chemistry* **1999**, *18*, 343-385.

(3) Knipping, E. M.; Lakin, M. J.; Foster, K. L.; Jungwirth, P.; Tobias, D. J.; Gerber, R. B.; Dabdub, D.; Finlayson-Pitts, B. J. *Science* **2000**, *288*, 301-306.

(4) Keene, W. C.; Sander, R.; Pszenny, A. A. P.; Vogt, R.; Crutzen, P. J.; Galloway, J. N. *Journal of Aerosol Science* **1998**, *29*, 339-356.

(5) Beichert, P.; Finlayson-Pitts, B. J. *Journal of Physical Chemistry* **1996**, *100*, 15218-15228.

(6) De Haan, D. O.; Finlayson-Pitts, B. J. *Journal of Physical Chemistry A* **1997**, *101*, 9993-9999.

(7) Leu, M.-T.; Timonen, R. S.; Keyser, L. F. *Journal of Physical Chemistry A* **1997**, *101*, 278-282.

(8) Fenter, F. F.; Caloz, F.; Rossi, M. J. *Journal of Physical Chemistry* **1994**, *98*, 9801-9810.

(9) Carpenter, L. J. *Chemical Reviews* **2003**, *103*, 4953-4962.

(10) Vogt, R.; Sander, R.; Von Glasow, R.; Crutzen, P. J. *Journal of Atmospheric Chemistry* **1999**, *32*, 375-395.

(11) McFiggans, G.; Plane, J. M. C.; Allan, B. J.; Carpenter, L. J.; Coe, H.; O'Dowd, C. *Journal of Geophysical Research, [Atmospheres]* **2000**, *105*, 14371-14385.

(12) Finlayson-Pitts, B. J.; Pitts, J. N. J. *Chemistry of the Upper and Lower Atmosphere: Theory, Experiments, and Applications*. Academic Press: San Diego, 2000.

(13) Winterton, N. *Green Chemistry* **2000**, *2*, 173-225.

(14) Prenni, A. J.; Tolbert, M. A. *Accounts of Chemical Research* **2001**, *34*, 545-553.

(15) Farman, J. C.; Gardiner, B. G.; Shanklin, J. D. *Nature* **1985**, *315*, 207-210.

(16) Solomon, S.; Garcia, R. R.; Rowland, F. S.; Wuebbles, D. J. *Nature* **1986**, *321*, 755-758.

(17) Solomon, S. *Reviews of Geophysics* **1999**, *37*, 275-316.

(18) Lary, D. J.; Chipperfield, M. P.; Toumi, R.; Lenton, T. *Journal of Geophysical Research, [Atmospheres]* **1996**, *101*, 1489-1504.

(19) Barone, S. B.; Zondlo, M. A.; Tolbert, M. A. *Journal of Physical Chemistry A* **1999**, *103*, 9717-9730.

(20) Chu, L. T.; Chu, L. *Journal of Physical Chemistry B* **1997**, *101*, 6271-6275.

(21) Bloembergen, N.; Pershan, P. S. *Physical Reviews* **1962**, *128*, 606-621.

(22) Hirose, C.; Akamatsu, N.; Domen, K. *Applied Spectroscopy* **1992**, *46*, 1051-1072.

(23) Miranda, P. B.; Shen, Y. R. *Journal of Physical Chemistry B* **1999**, *103*, 3292-3307.

(24) Morita, A.; Hynes, J. T. *Chemical Physics* **2000**, *258*, 371-390.

(25) Shen, Y. R. *The Principles of Nonlinear Optics*. John Wiley & Sons: New York, 1984.

(26) Bain, C. D. *Journal of the Chemical Society, Faraday Transactions* **1995**, *91*, 1281-1296.

(27) Moad, A. J. S., Garth J. *Journal of Physical Chemistry B* **2004**, *108*, 3548-3562.

(28) Zhang, D.; Gutow, J.; Eisenthal, K. B. *Journal of Physical Chemistry* **1994**, *98*, 13729-13734.

(29) Liu, D.; Ma, G.; Levering, L. M.; Allen, H. C. *Journal of Physical Chemistry B* **2004**, *108*, 2252-2260.

(30) McCreery, R. L. *Raman Spectroscopy for Chemical Analysis*. John Wiley & Sons: New York, 2000.

(31) Hommel, E. L. PhD, The Ohio State University, 2003.

(32) Buch, V.; Devlin, J. P. *Journal of Chemical Physics* **1999**, *110*, 3437-3443.

(33) Andersson, P.; Steinbach, C.; Buck, U. *European Physical Journal D: Atomic, Molecular and Optical Physics* **2003**, *24*, 53-56.

(34) Steinbach, C.; Andersson, P.; Kazimirski, J. K.; Buck, U.; Buch, V.; Beu, T. A. *Journal of physical Chemistry A* **2004**, *108*, 6165-6174.

(35) Devlin, J. P.; Sadlej, J.; Buch, V. *Journal of Physical Chemistry A* **2001**, *105*, 974-983.

(36) Allen, H. C.; Raymond, E. A.; Richmond, G. L. *Journal of Physical Chemistry A* **2001**, *105*, 1649-1655.

(37) Du, Q.; Superfine, R.; Freysz, E.; Shen, Y. R. *Physical Review Letters* **1993**, *70*, 2313-2316.

(38) Schnitzer, C.; Baldelli, S.; Campbell, D. J.; Shultz, M. J. *Journal of Physical Chemistry A* **1999**, *103*, 6383-6386.

(39) Shultz, M. J.; Baldelli, S.; Schnitzer, C.; Simonelli, D. *Journal of Physical Chemistry B* **2002**, *106*, 5313-5324.

(40) Rowland, B.; Fisher, M.; Devlin, J. P. *Journal of Chemical Physics* **1991**, *95*, 2485-2487.

(41) Vaden, T. D.; Weinheimer, C. J.; Lisy, J. M. *Journal of Chemical Physics* **2004**, *121*, 3102-3107.

(42) Shultz, M. J., personal communication, **2005**.

(43) Zundel, G. Easily Polarizable Hydrogen Bonds-Their Interactions With the Environment-IR Continuum and Anomalous Large Proton Conductivity. In *The Hydrogen Bond, Recent developments in theory and experiments*; Schuster, P., Zundel, G., Sandorfy, C., Eds.; North-Holland Publishing Company: Amsterdam, 1976; Vol. 2; Chapter 15.

(44) Roberts, N. K.; Zundel, G. *Journal of Physical Chemistry* **1980**, *84*, 3655-3660.

(45) Kim, J.; Schmitt, U. W.; Gruetzmacher, J. A.; Voth, G. A.; Scherer, N. E. *Journal of Chemical Physics* **2002**, *116*, 737-746.

(46) Schioeberg, D.; Zundel, G. *Journal of the Chemical Society, Faraday Transactions 2: Molecular and Chemical Physics* **1973**, *69*, 771-781.

(47) Falk, M.; Giguere, P. A. *Canadian Journal of Chemistry* **1957**, *35*, 1195-1204.

(48) Asmis, K. R.; Pivonka, N. L.; Santambrogio, G.; Bruemmer, M.; Kaposta, C.; Neumark, D. M.; Woeste, L. *Science* **2003**, *299*, 1375-1377.

(49) McCoy, A. B.; Huang, X.; Carter, S.; Landeweer, M. Y.; Bowman, J. M. *Journal of Chemical Physics* **2005**, *122*, 061101-061101-061101-061104.

(50) Diken, E. G.; Headrick, J. M.; Roscioli, J. R.; Bopp, J. C.; Johnson, M. A.; McCoy, A. B. *Journal of Physical Chemistry* **2005**, *ASAP*.

(51) Janoschek, R.; Weidemann, E. G.; Pfeiffer, H.; Zundel, G. *Journal of the American Chemical Society* **1972**, *94*, 2387-2396.

(52) Mucha, M.; Frigato, T.; Levering, L. M.; Allen, H. C.; Tobias, D. J.; Dang, L. X.; Jungwirth, P. *Journal of Physical Chemistry B* **2005**.

(53) Jungwirth, P.; Tobias, D. J. *Journal of Physical Chemistry B* **2001**, *105*, 10468-10472.

(54) Jungwirth, P.; Tobias, D. J. *Journal of Physical Chemistry B* **2002**, *106*, 6361-6373.

(55) Petersen, M. K.; Iyengar, S. S.; Day, T. J. F.; Voth, G. A. *Journal of Physical Chemistry B* **2004**, *108*, 14804-14806.

(56) Yeh, L. I.; Okumura, M.; Myers, J. D.; Price, J. M.; Lee, Y. T. *Journal of Chemical Physics* **1989**, *91*, 7319-7330.

(57) Janoschek, R.; Hayd, A.; Weidemann, E. G.; Leuchs, M.; Zundel, G. *Journal of the Chemical Society, Faraday Transactions 2: Molecular and Chemical Physics* **1978**, *74*, 1238-1245.

(58) Graham, J. D.; Roberts, J. T. *Chemometrics and Intelligent Laboratory Systems* **1997**, *37*, 139-148.

(59) Buck, U.; Ettischer, I.; Melzer, M.; Buch, V.; Sadlej, J. *Physical Review Letters* **1998**, *80*, 2578-2581.

(60) Steinbach, C.; Andersson, P.; Melzer, M.; Kazimirski, J. K.; Buck, U.; Buch, V. *Physical Chemistry Chemical Physics* **2004**, *6*, 3320-3324.

(61) Kazimirski, J. K.; Buch, V. *Journal of Physical Chemistry A* **2003**, *107*, 9762-9775.

(62) *Water In Confining Geometries*; Buch, V.; Devlin, J. P., Eds.; Springer: Germany, 2003.

(63) Zwier, T. S. *Science* **2004**, *304*, 1119-1120.

(64) Wei, S.; Shi, Z.; Castleman, A. W., Jr. *Journal of Chemical Physics* **1991**, *94*, 3268-3270.

(65) Svanberg, M.; Pettersson, J. B. C. *Journal of Physical Chemistry A* **1998**, *102*, 1865-1872.

(66) Khan, A. *Chemical Physics Letters* **2000**, *319*, 440-450.

(67) Shin, J.-W.; Hammer, N. I.; Diken, E. G.; Johnson, M. A.; Walters, R. S.; Jaeger, T. D.; Duncan, M. A.; Christie, R. A.; Jordan, K. D. *Science* **2004**, *304*, 1137-1141.

(68) Miyazaki, M.; Fujii, A.; Ebata, T.; Mikami, N. *Science* **2004**, *304*, 1134-1137.

(69) Kassner, J. L., Jr.; Hagen, D. E. *Journal of Chemical Physics* **1976**, *64*, 1860-1861.

(70) Nagashima, U.; Shinohara, H.; Nishi, N.; Tanaka, H. *Journal of Chemical Physics* **1986**, *84*, 209-214.

(71) Scherer, J. R. The Vibrational Spectroscopy of Water. In *Advances in Infrared and Raman Spectroscopy*; Clark, R. J. H., Hester, R. E., Eds.; Heyden: Philadelphia, 1978; Vol. 5.

(72) Raymond, E. A.; Tarbuck, T. L.; Richmond, G. L. *Journal of Physical Chemistry B* **2002**, *106*, 2817-2820.

(73) Raymond, E. A.; Tarbuck, T. L.; Brown, M. G.; Richmond, G. L. *The Journal of Physical Chemistry B* **2003**, *107*, 546-556.

(74) Raymond, E. A.; Richmond, G. L. *Journal of Physical Chemistry B* **2004**, *108*, 5051-5059.

(75) Randles, J. E. B. *Phys. Chem. Liq.* **1977**, *7*, 107-179.

(76) Adam, N. K. *The Physics and Chemistry of Surfaces*. Oxford University Press: London, 1941.

(77) Onsager, L.; Samaras, N. N. T. *Journal of Chemical Physics* **1934**, *2*, 528-536.

(78) Dang, L. X.; Chang, T.-M. *Journal of Physical Chemistry B* **2002**, *106*, 235-238.

(79) Ghosal, S.; Shbeeb, A.; Hemminger, J. C. *Geophysical Research Letters* **2000**, *27*, 1879-1882.

(80) Petersen, P. B.; Johnson, J. C.; Knutsen, K. P.; Saykally, R. J. *Chemical Physics Letters* **2004**, *397*, 46-50.

(81) Ritzhaupt, G.; Devlin, J. P. *Journal of Physical Chemistry* **1991**, *95*, 90-95.

(82) Brown, M. G.; Raymond, E. A.; Allen, H. C.; Scatena, L. F.; Richmond, G. L. *Journal of Physical Chemistry A* **2000**, *104*, 10220-10226.

APPENDIX A

IR ENERGY TESTS

When acquiring vibrational sum frequency generation (VSFG) spectra, careful consideration must be given to the individual energies of the visible and infrared (IR) beams as well as the magnitude of one with respect to the other. The magnitude of these energies can have a drastic effect on the shape of the vibrational sum frequency spectrum of water.

Initial studies were performed on 0.015*x* and 0.050*x* solutions of HCl, HBr, and HI. On one day, the VSFG spectra of the 0.015*x* solutions were acquired (Figure A.1a) and on another day, the VSFG spectra of the 0.050*x* solutions were acquired (Figure A.1b); the only difference in the instrument settings from the two days was the position of the IR focusing lens (i.e. the tightness of the IR beam focus at the sample).

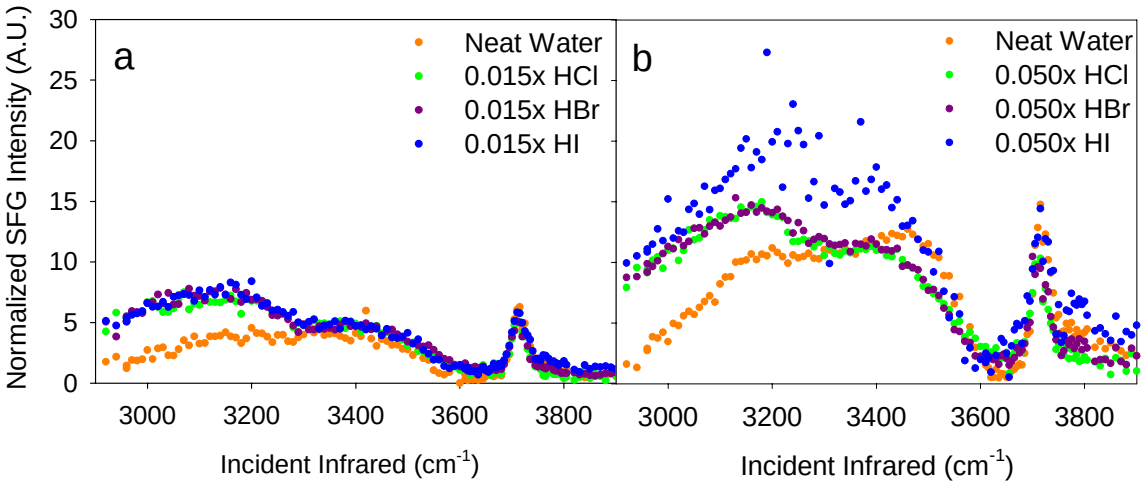

Figure A.1. (a) SSP-polarized VSFG spectra of 0.015*x* HCl, HBr, and HI. (b) SSP-polarized VSFG spectra of 0.050*x* HCl, HBr, and HI. The neat water VSFG spectrum is plotted in each figure for comparison. Visible energy: 0.35 mJ, IR energy: ~400 μJ.

As shown in Figure A.1, the shape and intensities of the spectra suggest a dependency on the focusing parameters of the IR beam. As shown in Figure A.2, with a tighter focus, the 3400 cm^{-1} peak in the hydrogen-bonding region of water has a peaked appearance, which is fully evident when the two water spectra are plotted on the same graph.

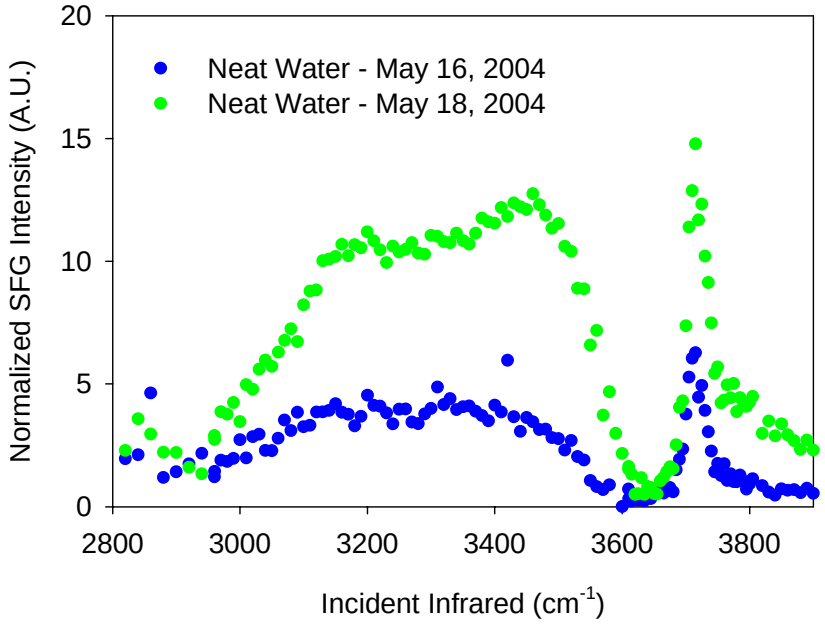

Figure A.2. SSP-polarized VSFG spectra of neat water acquired with different IR focusing parameters. Visible energy: 0.35 mJ, IR energy: ~400 μJ.

The source of the changing water shape is perhaps due to acquiring the VSFG spectra in a regime where the sum frequency response of the molecules in the interface is nonlinear with the incident infrared energy. Under optimal conditions, the intensity of the sum frequency signal, $I(\omega_{SFG})$, is directly proportional to the intensities of the incident infrared, $I(\omega_{IR})$, and visible beam, $I(\omega_{vis})$, [23,24,82] as shown by equation A1,

$$I(\omega_{SFG}) \propto \left|\chi^{(2)}\right|^2 I(\omega_{IR}) I(\omega_{vis}) \qquad \text{(A1)}$$

where $\omega_{SFG} = \omega_{IR} + \omega_{vis}$ and $\chi^{(2)}$ is the second-order susceptibility of the medium at the interface. When excess IR energy is pumped onto the sample surface, the ability of the molecules to absorb IR energy and undergo a vibrational transition seems to be altered and thus, the sum frequency response becomes nonlinear and an artificial structure in the

VSFG spectra results (i.e. the enhancement of the 3400 cm^{-1} peak in the VSFG water spectrum).

Two options to reduce the IR energy density are: 1) attenuate the IR beam with a window or polarizer and/or 2) loosen the focus of the IR beam. First, the focus of the IR beam was relaxed, generating the VSFG spectrum in Figure A.3; the shape of this water spectrum is more similar to VSFG water spectra in literature.[29,37-39] A comparison of the peak intensities provides a good indication the acquisition parameters have been improved. First of all, the 3400 cm^{-1} peak no longer has a peaked appearance. Previous research on the VSFG spectrum of water[29,37-39] reveal the 3250 cm^{-1} and 3400 cm^{-1} peaks should be approximately equal in intensity; relaxation of the IR focus generates a VSFG spectrum that has comparable 3250 cm^{-1} and 3400 cm^{-1} peak intensities. Secondly, the free O-H peak intensity at 3700 cm^{-1} is much more intense. Literature VSFG spectra of neat water[29,37-39] show that the free O-H peak intensity is on the order of two to four times the intensity of the 3250 cm^{-1} and 3400 cm^{-1} peaks. The previous neat water and acid VSFG spectra have roughly the same intensities for all three peaks (3250, 3400, and 3700 cm^{-1}); relaxation of the IR focus also improves this concern by increasing the ratio of the free O-H peak to the 3250 cm^{-1} and 3400 cm^{-1} peaks to nearly 4:1.

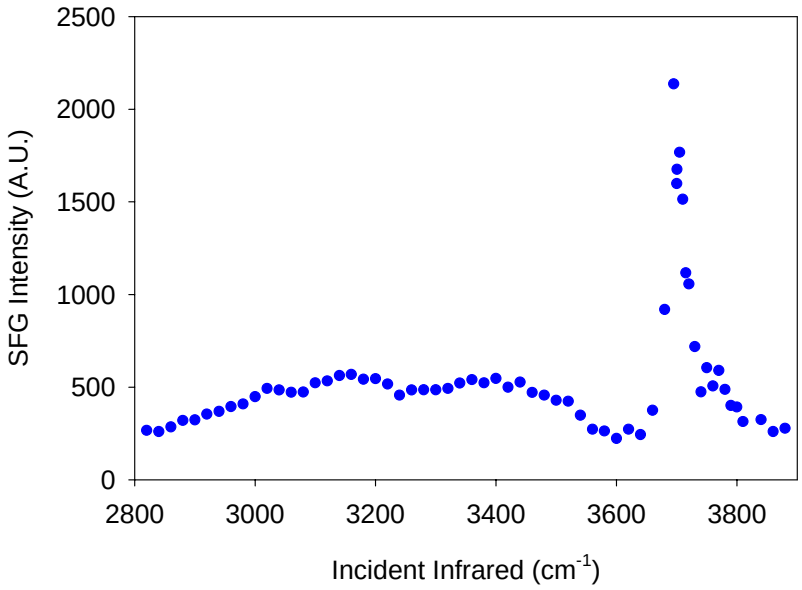

Figure A.3. SSP-polarized VSFG spectrum of neat water after relaxing the IR focus (IR energy density is decreased at the sample surface).

To double-check that the system was no longer in a nonlinear regime, an energy test was done using a zinc selenide (ZnSe) window. In the range between 0.6 and 16 μm, ZnSe transmits ~65% of the light passing through the window. Thus, if this window is placed in the path of the IR beam, the IR beam energy will be reduced by ~35% and thus the raw VSFG signal should be reduced by ~35% since the VSFG intensity is proportional to the intensity of the IR beam. Figure A.4 shows the comparison between the VSFG water spectrum and the VSFG water spectrum with the ZnSe window; after viewing the spectra, it is obvious that there is still an energy issue since the VSFG intensity between 3000 and 3600 cm^{-1} actually increases and the intensity of the 3700 cm^{-1} peak remains constant when the ZnSe window is in place.

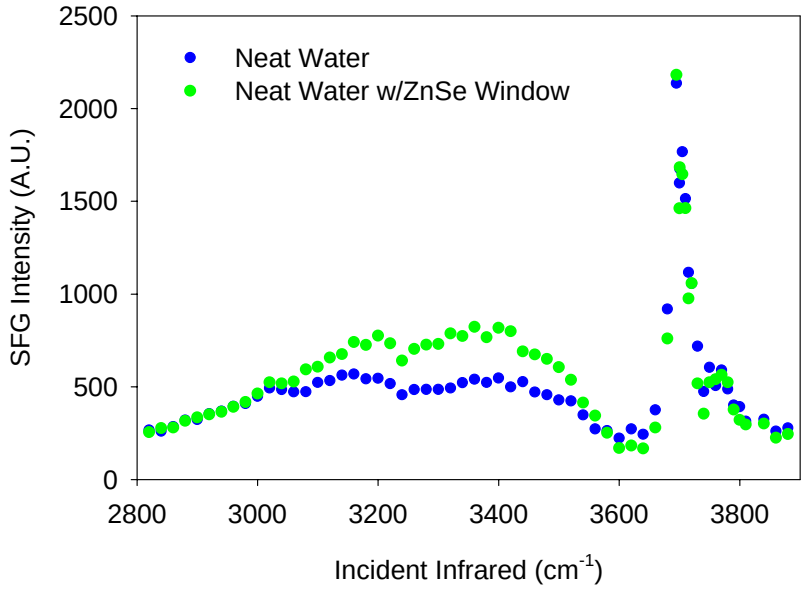

Figure A.4. Comparison of SSP-polarized VSFG spectra of neat water with and without a ZnSe window.

Further examination of the visible and IR energies was done to ensure that the expected trend of decreasing SFG signal with decreasing visible or IR energies was observed. First, the effect of decreasing the visible energy was studied; spectra were acquired at visible energies of 0.9 mJ and 0.45 mJ, keeping the IR energy constant at ~400 μJ. As shown in Figure A.5, when the visible energy is halved, the raw VSFG signal intensity is halved.

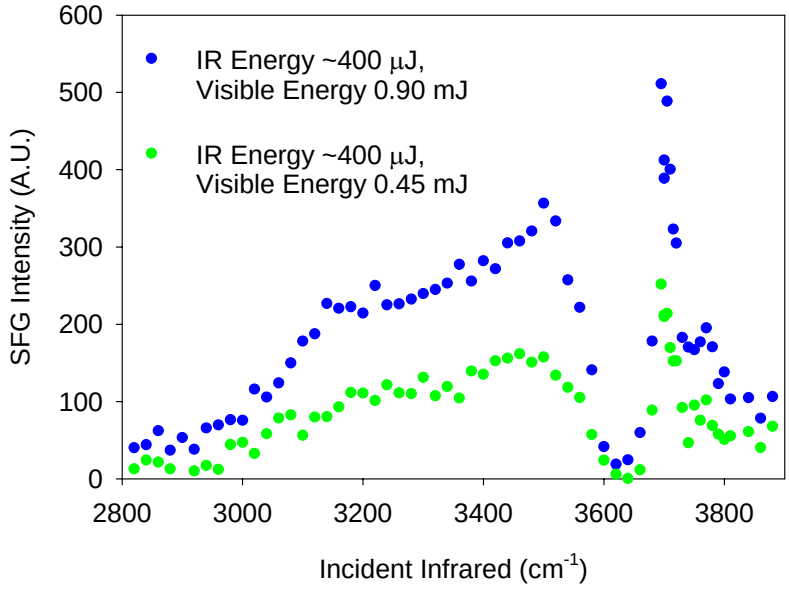

Figure A.5. SSP-polarized VSFG spectra of neat water with incident visible energies of 0.90 mJ and 0.45 mJ.

Next, the IR energy was changed from ~400 μJ to ~100 μJ while the visible energy was held constant at 0.9 mJ (Figure A.6); the raw VSFG signal intensity decreases by the same magnitude that the IR energy is decreased. Since the raw VSFG signal responds as predicted for a decrease in both the visible and IR energies, it seems that the problem with the nonlinearity of the sum frequency response has been fixed. However, normalization of the VSFG spectra by the IR energy profile should provide spectra that overlap exactly. The IR normalized VSFG spectra are shown in the inset of Figure A.6 and reveal the issue is not completely resolved since the spectra do not overlap.

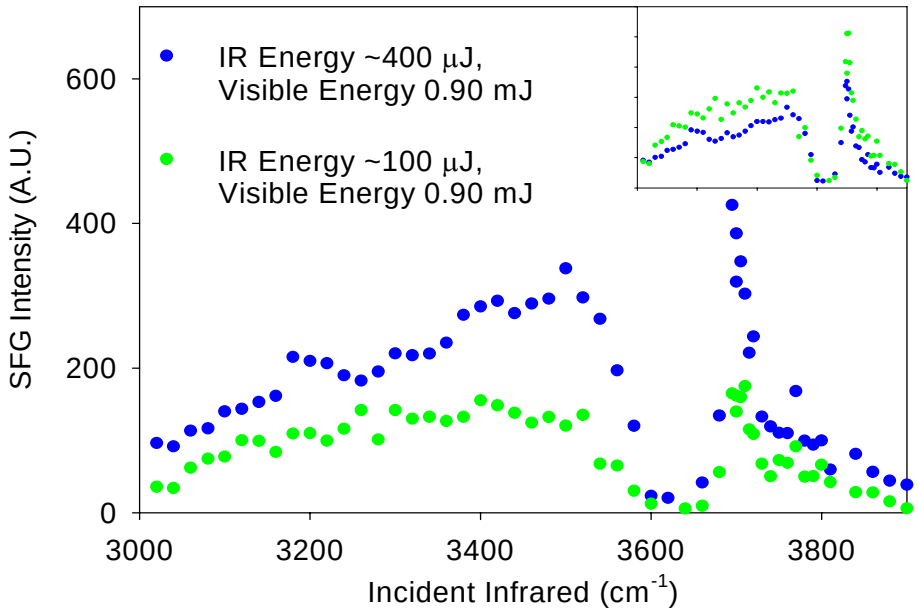

Figure A.6. SSP-polarized VSFG spectra of neat water with incident infrared energies of ~400 μJ and ~100 μJ. Inset: IR profile normalized SSP-polarized VSFG spectra of neat water using infrared energies of ~400 μJ and ~100 μJ.

In order to obtain overlapping normalized VSFG spectra, the IR beam was relaxed further. Figure A.7 shows the water spectra acquired at IR energies of ~450μJ and ~250 μJ and a visible energy of 0.9 mJ. As can been seen, when the IR energy is decreased, the raw VSFG signal also decreases. In addition, the IR normalized water spectra overlap at the two different IR energies (inset of Figure A.7), indicating that the issue with the nonlinear response of the sum frequency signal was resolved.

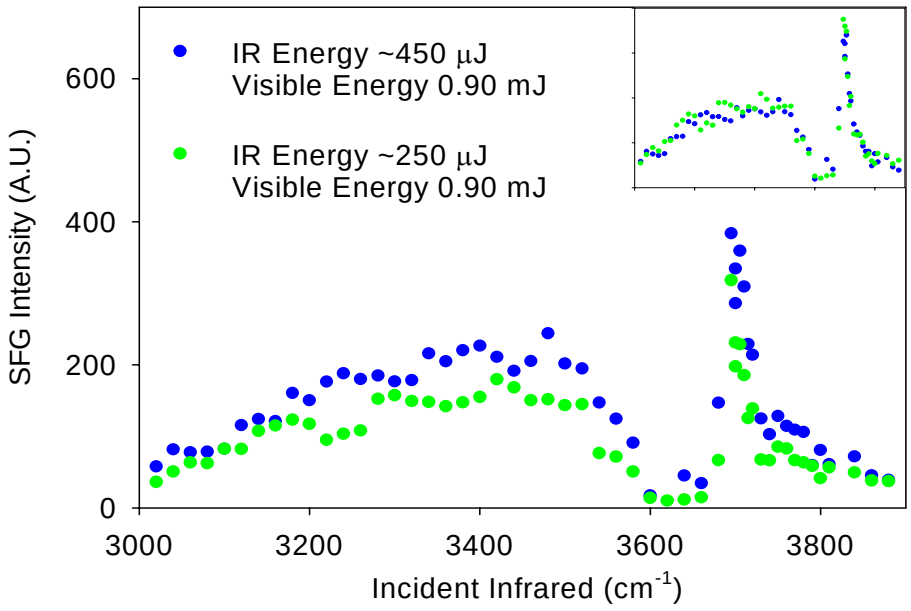

Figure A.7. SSP-polarized VSFG spectra of neat water with incident infrared energies of ~450 μJ and ~250 μJ. Inset: IR profile normalized SSP-polarized VSFG spectra of neat water using infrared energies of ~450 μJ and ~250 μJ.

As a final test on the sum frequency system, the energy test with the ZnSe window was redone in order to see if it could be used as a quick test to ensure the sum frequency system was not operating in the nonlinear regime. The expected decrease in the sum frequency signal of the spectrum with the ZnSe window still was not observed. Placing the ZnSe window in the IR beam path may alter the IR focusing parameters and thus, negating the energy reducing capabilities of the window.

In summary, it is crucial to conduct two tests prior to obtaining VSFG spectra. The first test is to half the visible energy while monitoring the IR energy; the raw spectral intensities over the whole spectral region should decrease to half than the original intensities. The second test is to half the IR energy; the resultant spectra must also

decrease to half its original value at all frequencies to be used (if viewing the raw VSFG data). The IR normalized VSFG spectra should overlap exactly at all frequencies for both tests.

APPENDIX B

CONFIRMATION OF IGOR FIT USING MATHCAD

The VSFG spectral fits obtained from the IGOR program were confirmed by using a Mathcad 2000 program written by Dr. Dingfang Liu of the Allen lab. The program utilizes equations B1 and B2 to calculate the component peaks and calculated fit from parameters obtained from IGOR.

$$\chi_v^{(2)} \propto \frac{A_v}{\omega_v - \omega_{IR} - i\Gamma_v} \tag{B1}$$

$$\chi^{(2)} = \chi_{NR}^{(2)} + \sum_v \chi_v^{(2)} \tag{B2}$$

The variables A_v, ω_v, and Γ_v in equation B1 correspond to the IGOR peak amplitude, position and width values, respectively. Plotting $\chi_v^{(2)}$ versus the infrared wavelength range for each vibration yields the component peaks. Summing the non-resonant terms from IGOR and each vibration's $\chi_v^{(2)}$ and squaring the value, as in equation B3, provides the calculated VSFG fit.

$$signal = \left| \chi_{NR}^{(2)} + \left(\sum_v \frac{A_v}{\omega_v - \omega_{IR} - i\Gamma_v} \right) \right|^2 \tag{B3}$$

The following is the Mathcad 2000 code for calculating the component peaks and the overall fit for the neat water VSFG spectrum. The variables are defined as follows:

a	IGOR peak amplitude
b	IGOR peak position
c	IGOR peak width
x	IR wavelength range
c(n)(x)	The $\chi_v^{(2)}$ value for the n^{th} vibration
f(x), g(x), h(x), i(x), j(x)	The component peak for the n^{th} vibration as a function of x
NR	IGOR non-resonant values (real and imaginary)
k(x)	The calculated VSFG fit

The component peaks and the calculated VSFG spectrum are plotted with the VSFG experimental data (red circles) for comparison in Figure B.1.

peak1

$a := 274.161$

$b := 3234.82$

$c := 140.939$

$x := 2800, 2805.. 3950$

$$c0(x) := \frac{a}{x - b - i \cdot c}$$

$$f(x) := \left(\left| \frac{a}{x - b - i \cdot c} \right| \right)^2$$

$f(x) =$

0.293
0.299
0.306
0.312
0.319
0.326
0.333
0.341
0.349
0.357
0.365
0.373
0.382
0.391
0.401
0.41

peak2

$a := 247.543$

$b := 3382.87$

$c := 97.5755$

$x := 2800, 2805.. 3950$

$$c1(x) := \frac{a}{x - b - i \cdot c}$$

$$g(x) := \left(\left| \frac{a}{x - b - i \cdot c} \right| \right)^2$$

$g(x) =$

0.175
0.178
0.181
0.185
0.188
0.191
0.194
0.198
0.201
0.205
0.209
0.213
0.217
0.221
0.225
0.229

peak3

$a := 72.1$

$b := 3568.8$

$c := 78.5$

$x := 2800, 2805.. 3950$

$$c2(x) := \frac{a}{x - b - i \cdot c}$$

$$h(x) := \left(\left| \frac{a}{x - b - i \cdot c} \right| \right)^2$$

$h(x) =$

$8.704 \cdot 10^{-3}$
$8.818 \cdot 10^{-3}$
$8.933 \cdot 10^{-3}$
$9.051 \cdot 10^{-3}$
$9.17 \cdot 10^{-3}$
$9.293 \cdot 10^{-3}$
$9.418 \cdot 10^{-3}$
$9.545 \cdot 10^{-3}$
$9.675 \cdot 10^{-3}$
$9.807 \cdot 10^{-3}$
$9.943 \cdot 10^{-3}$
0.01
0.01
0.01
0.011
0.011

peak4

$a := 86.6361$

$b := 3698.76$

$c := 20.039$

$x := 2800, 2805.. 3950$

$$c3(x) := \frac{a}{x - b - i \cdot c}$$

$$i(x) := \left(\left| \frac{a}{x - b - i \cdot c} \right| \right)^2$$

$i(x) =$

$9.287 \cdot 10^{-3}$
$9.392 \cdot 10^{-3}$
$9.497 \cdot 10^{-3}$
$9.605 \cdot 10^{-3}$
$9.715 \cdot 10^{-3}$
$9.826 \cdot 10^{-3}$
$9.94 \cdot 10^{-3}$
0.01
0.01
0.01
0.01
0.011
0.011
0.011
0.011
0.011

peak5

$a := 198.878$

$b := 3742.66$

$c := 86.9$

$x := 2800, 2805.. 3950$

$$c4(x) := \frac{a}{x - b - i \cdot c}$$

$$j(x) := \left(\left| \frac{a}{x - b - i \cdot c} \right| \right)^2$$

$j(x) =$

0.044
0.045
0.045
0.046
0.046
0.047
0.047
0.048
0.048
0.049
0.049
0.05
0.05
0.051
0.051
0.052

$NR := -1.2187 + 0.17749i$

$$k(x) := \left(\left| NR + c0(x) + c1(x) - c2(x) - c3(x) - c4(x) \right| \right)^2$$

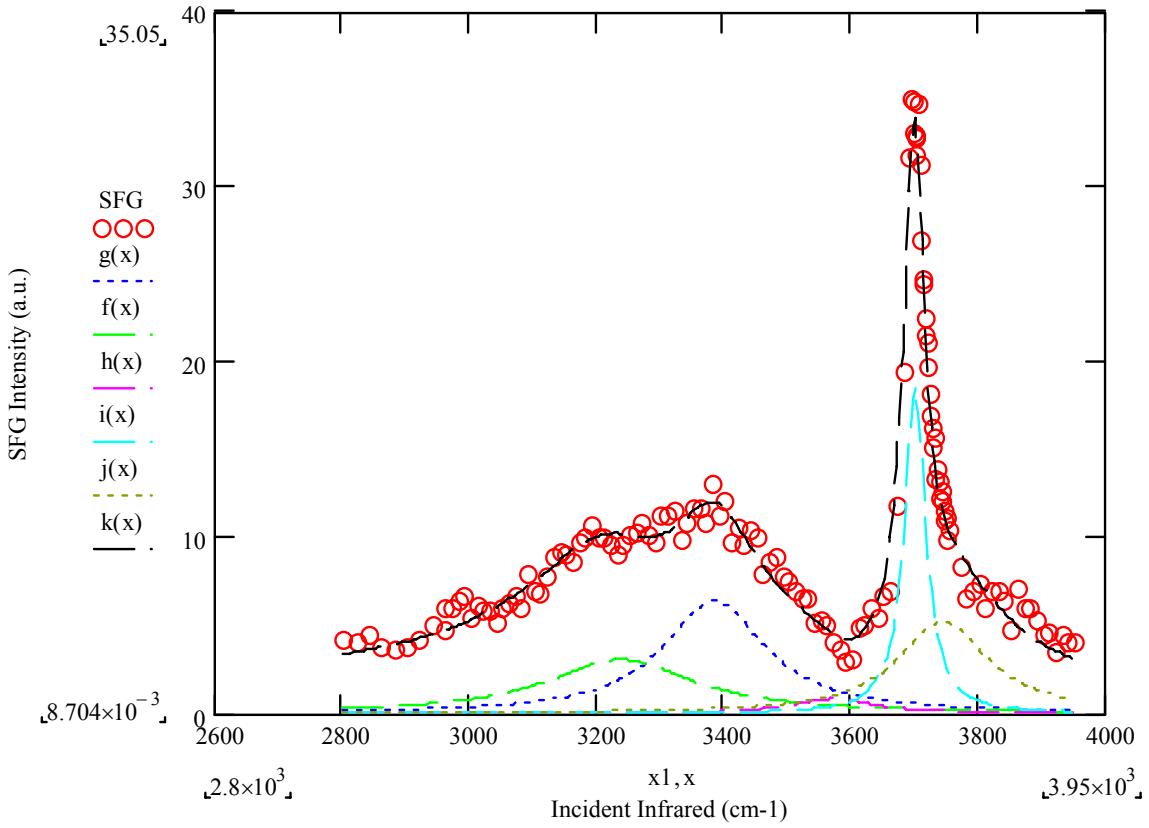

Figure B.1. The Mathcad calculated component peaks and VSFG spectrum for neat water. The experimental VSFG spectrum (red circles) is plotted for comparison.